

THE CATHOLIC UNIVERSITY OF AMERICA

Two-dimensional Continuous Wavelet Transform in Fringe Pattern Analysis

A DISSERTATION

Submitted to the Faculty of the
Department of Mechanical Engineering
School of Engineering
Of The Catholic University of America
In Partial Fulfillment of the Requirements
For the Degree
Doctor of Philosophy
©
Copyright
All Rights Reserved
By
Jun Ma

Washington, D.C.

2013

Two-dimensional Continuous Wavelet Transform in Fringe Pattern Analysis

Jun Ma, Ph.D.

Director: Zhaoyang Wang, Ph.D.

A vital task of fringe pattern analysis is to extract the phase distribution of interferograms in which certain physical quantities are concealed. Because of its robustness, the two-dimensional continuous wavelet transform (2D-CWT) technique has drawn a lot of attentions in recent years, and becomes one of the most important techniques in fringe pattern analysis. Hence, the dissertation investigates the theory of the 2D-CWT thoroughly, and elaborates the proposed algorithms based on the 2D-CWT technique to extract the phase distribution of interferograms efficiently and accurately. Both computer simulation and real experiments are conducted to verify the validity and effectiveness of the proposed algorithms as well.

First, when analyzes the interferogram whose phase distribution is non-monotonic by using the 2D-CWT technique, the phase ambiguity issue is inevitable. To cope with the phase ambiguity issue, in this dissertation, a phase determination rule is proposed according to the phase distribution continuity, and a frequency-guided scheme is employed to obtain the correct phase distribution following a conventional 2D-CWT analysis.

However, the processing of 2D-CWT is usually time-consuming. In order to speed up

the 2D-CWT analysis, the dissertation introduces a concept called the cover map. The cover map is constructed by discretizing the continuous dilation and rotation parameters. Then an algorithm is proposed based on the discretized parameters so as to substantially reduce the processing time without affecting the analysis accuracy.

In addition, the dissertation evaluates the performance of different kinds of mother wavelets for the 2D-CWT technique being used in optical fringe pattern analysis. Based upon the investigation, a 2D modulated Mexican hat wavelet is introduced to improve the performance of the 2D-CWT analysis.

Finally, in fringe pattern analysis, a technique is highly demanded to automatically analyze the interferograms that contain complex fringes and high-level noise as well as defects. In this dissertation, a hybrid technique is proposed to combine the concepts of the 2D-CWT technique and the phase-shifting technique. The novel technique takes the advantages of the two existing techniques, and has the ability to accurately and automatically analyze multiple phase-shifted complex interferograms involving noise and defects.

This dissertation by Jun Ma fulfills the dissertation requirement for the doctoral degree in Mechanical Engineering approved by Zhaoyang Wang, Ph.D., as Director, and by John A. Judge, Ph.D., and Jandro L. Abot, Ph.D. as Readers.

Zhaoyang Wang, Ph.D., Director

John A. Judge, Ph.D., Reader

Jandro L. Abot, Ph.D., Reader

to my dear wife Lei, and our lovely daughter Xinrong.

Table of Contents

List of Figures	vi
List of Tables	ix
Nomenclature	x
1 Introduction	1
1.1 Review	1
1.2 Objectives	5
1.3 Contributions	6
1.4 Organization	7
2 Optical Interference	9
2.1 Young's Double-slit Experiment	11
2.2 Interferometry	13
2.3 Moiré Technique	14
2.4 Simulation	17
2.4.1 Monotonic Fringe Patterns	18
2.4.2 Closed/Saddled Fringe Patterns	19
2.4.3 Peaks Fringe Patterns	20
2.4.4 Noise	22
3 Fringe Pattern Analysis	24
3.1 Phase Shifting Technique	25
3.2 Fourier Transform Technique	28
3.3 Time-frequency Analysis Technique	30
4 2D-CWT in Fringe Pattern Analysis	33
4.1 2D-CWT	34
4.1.1 Definition	34
4.1.2 2D Wavelet Ridge	36

4.2	Direct Ridge Detection Algorithm	37
4.2.1	Algorithm	37
4.2.2	Phase Ambiguity	40
4.3	Phase Determination Rule	44
4.3.1	Algorithm	44
4.3.2	Simulation	46
4.4	Cover Map	50
4.4.1	Heisenberg Uncertainty Principle	51
4.4.2	Wavelet modulated window	52
4.4.3	Cover Map	54
4.4.4	Simulation	59
4.5	Performance	64
4.5.1	Isotropic Wavelets	65
4.5.2	Directional Wavelets	68
4.5.3	Simulation	74
4.6	Hybrid Technique	76
4.6.1	Principle	78
4.6.2	Algorithm	80
4.6.3	Simulation	81
5	Experiments	86
5.1	Warpage Measurement	86
5.2	PBGA Measurement	89
5.3	Thermal Deformation Measurement	93
6	Conclusions and Future Work	96
6.1	Conclusions	96
6.2	Future Work	98
Bibliography		99

List of Figures

2.1	The Young's double-slit experiment.	11
2.2	Geometric diagram of the Young's double-slit experiment.	12
2.3	Schematic diagram of the Michelson interferometer.	14
2.4	The moiré patterns are observed through: (a) two sinusoidal gratings, and (b) two circular gratings.	15
2.5	Simulated fringe patterns with a linear chirp distribution.	19
2.6	Simulated Newton rings.	20
2.7	Simulated saddled fringe patterns.	20
2.8	Simulated peaks patterns.	21
2.9	Simulated five struts on a plate.	22
2.10	Simulated peaks fringe patterns with the additive white noise.	23
2.11	Simulated peaks fringe patterns: (a) the object image, and (b) with (a) and the additive white noise.	23
3.1	Schematic diagram of the Fourier transform method.	30
4.1	The DRD algorithm applied in fringe patterns with monotonic phase distribution: (a) Simulated fringe patterns, (b) extracted wrapped phase distribution, (c) unwrapped phase distribution with gray scale illustration, and (d) unwrapped phase distribution with 3D illustration.	41
4.2	Phase ambiguity in a simulated interferogram with non-monotonic phase distribution: (a) Simulated fringe patterns with four peaks, and (b) extracted phase distribution with $\theta \in [-\pi, \pi]$	42
4.3	Wavelet coefficients demonstration.	43
4.4	Phase ambiguity removed with $\theta \in [-\frac{\pi}{2}, \frac{\pi}{2}]$	43
4.5	phase distribution by using the DRD algorithm with $\theta \in [-\pi/2, \pi/2]$: (a) Simulated closed fringe patterns, and (b) phase ambiguity.	44
4.6	Explanation for the phase ambiguity of Fig. 4.5: (a) Wrong phase map, and (b) correct phase map.	45
4.7	Phase distribution and rotation angles in the analysis of Fig.4.5: (a) $\phi(\mathbf{x})$ and θ along a line, and (b) extracted phase distribution.	46

4.8	Phase distribution and rotation angles by applying the PDR: (a) $\phi(\mathbf{x})$ and θ along a line, and (b) correct phase distribution.	47
4.9	The 2D-CWT analysis of an interferogram with a complex phase distribution: (a) Original interferogram, (b) extracted phase distribution by using $\theta \in [0, \pi]$ in the DRD algorithm, (c) extracted phase with the PDR, and (d) unwrapped phase map.	48
4.10	Phase distribution extracted from an interferogram containing a crack: (a) Interferogram in a crack region, (b) detected incorrect phase distribution, (c) boundary mask, and (d) detected correct phase distribution.	49
4.11	Wavelet modulated window in the frequency domain.	54
4.12	Examples of cover maps: (a) $\sigma = 1.0$ and $q = 1.2536$, (b) $\sigma = 0.5$ and $q = 1.5809$, (c) $\sigma = 0.3376$ and $q = 2.0$, and (d) $\sigma = 0.5$ and $q = 2.0$	57
4.13	Schematic of the calculation of rotation angle.	58
4.14	Complete dyadic cover map for $\sigma = 0.3376$	59
4.15	Frequency response.	60
4.16	Frequency response for $\sigma = 0.5$: (a) $s = 3.2162$, (b) $s = 8.0380$, (c) $s = 20.0892$, and (d) $s = 125.4847$	61
4.17	Simulation results: (a) fringe pattern, (b) fringe pattern with noise, (c) extracted phase, (d) phase gradient, (e) phase gain, and (f) frequency gain.	63
4.18	Simulated interferogram: (a) without noise, and (b) with noise	67
4.19	Errors of phase extracted by using isotropic wavelets.	67
4.20	Isotropic wavelets with $H(\omega) = 1$ for $\omega_x \geq 0$ in the frequency domain: (a) grayscale illustration, and (b) schematic with the cutoff frequencies denoted as $(\omega_{c1}, \omega_{c2})$	69
4.21	The Morlet wavelet with different σ in the time domain.	70
4.22	Directional wavelets in the frequency domain: (a) grayscale illustration, and (b) schematic with the modulated frequency ω_0 and radius $\Delta\hat{\psi}$	71
4.23	Errors of phase extracted by using directional wavelets.	74
4.24	Simulated interferogram with large local fringe variations.	76
4.25	Phase-shifted interferograms generated from computer simulation: (a) $\delta = 0$, (b) $\delta = \frac{\pi}{2}$, (c) $\delta = \pi$, and (d) $\delta = \frac{3\pi}{2}$	82
4.26	Simulation results: (a) ideal wrapped phase map, (b) wrapped phase map with the phase-shifting technique, (c) wrapped phase map with the conventional 2D-CWT technique, and (d) wrapped phase map with the hybrid 2D-CWT techniques.	83
4.27	Unwrapped phase analysis: (a) unwrapped phase, (b) three-dimensional view of (a), (c) comparison with the ideal phase along $x = 128$ pixel, and (d) comparison with the ideal phase along $y = 128$ pixel	84

5.1	Warpage measurement of an electronic package: (a) Fringe pattern (288×288 pixels), (b) Wrapped phase distribution, (c) Refined wrapped phase distribution, and (d) 3D warpage.	87
5.2	Displacement measurement of a circular disc: (a) Fringe pattern (1024×1024 pixels), (b) wrapped phase distribution, (c) refined wrapped phase distribution, and (d) displacement map	88
5.3	Moiré fringe pattern of a PBGA package and the analysis results obtained by the conventional 2D-CWT scheme: (a) fringe pattern, (b) boundary mask, (c) spectrum, and (d) phase map.	90
5.4	Analysis results with different cover map parameters: (a) cover map for $\sigma = 1.0$, (b) phase map from $\sigma = 1.0$, (c) cover map for $\sigma = 0.5$, (d) phase map from $\sigma = 0.5$, (e) cover map for $\sigma = 0.3376$, and (f) phase map from $\sigma = 0.3376$	91
5.5	Comparison of analysis speed associated with different cover maps.	92
5.6	A real moiré interferogram.	93
5.7	Wrapped phase maps extracted by using the 2D-CWT technique with different wavelets: (a) 2D-AMHW, (b) 2D-PW, (c) 2D-MW, and (d) 2D-MMHW.	94

List of Tables

4.1	Mean relative errors of phase extracted by using directional wavelets with $ \omega_0 = 2\pi$ and various σ	75
4.2	Performance comparison.	85

Nomenclature

Notations

I	Intensity distribution of interferograms
L^p	Lebesgue spaces, p -norms function spaces
\mathcal{F}	Fourier transform operator
\mathcal{S}	Short-time (windowed) Fourier transform operator
\mathcal{W}	wavelet transform operator
\Im	imaginary part of complex number
\Re	real part of complex number
\mathbb{C}	complex numbers
\mathbb{N}	natural numbers
\mathbb{R}	real numbers
\mathbb{Z}	integer numbers
s	scale factor of the wavelet transform
θ	rotation angle of the two-dimensional continuous wavelet transform
ψ	mother wavelet
$\hat{\psi}$	Fourier transform of ψ
ψ^*	conjugate of ψ

μ	mean
σ	standard deviation
\langle , \rangle	inner product
$\ \cdot\ _p$	p -norm

Abbreviations

CWT	Continuous Wavelet Transform
DRD	Direct Ridge Detection
DWT	Discrete Wavelet Transform
FFT	Fast Fourier Transform
FT	Fourier Transform
PDR	Phase Determination Rule
PS	Phase Shifting
SNR	Signal-to-noise ratio
STFT	Short-time Fourier Transform
WFT	Windowed Fourier Transform
WT	Wavelet Transform
WVD	Wigner-Ville Distribution
1D	One-dimensional
2D	Two-dimensional
3D	Three-dimensional

Acknowledgments

I would like to express my sincere appreciation to my advisor Dr. Zhaoyang Wang for the opportunity he offered me to pursue a Ph.D. at The Catholic University of America, and for all the guidance and financial support over the last three years. Thank you to Dr. John Judge, Dr. Jandro L. Abot, Dr. Nader Namazi and Dr. Lu Sun for serving on my dissertation committee and all the valuable advices. In particular, I would like to thank the Chair, the faculty and staff of the department of mechanical engineering for the support during my Ph.D. study and research at CUA.

My deepest gratitude goes to my family. Without their understanding and unconditional support, I could not achieve any goal. Firstly, I am indebted to my wife Lei for her endless love and support, through the duration of my study and research. It is not easy at all for her to take care of our daughter alone. In some sense, it is much more difficult compared to my study and research. In addition, I owe an apology to my daughter Xinrong for my absence over the past years and missing her first three birthday parties. Finally, I would like to thank our beloved parents, sisters, and other relatives for the support and help to my wife during these years.

I had a really great time living in the Saint Joseph's Seminary. I would like to show my greatest gratitude to all the priests, deacons, seminaries, and residents in the Saint Joseph's Seminary. Their gracious company will be the memory that I will cherish for a lifetime.

Thank you to the rectors, especially Bishop John H. Ricard, S.S.J. and Father Brian Fox, S.S.J for their kindness and generosity to me. Especially, I want to thank Reverend Father John Filippelli, S.S.J. for all the interesting chats where I have learned a lot about the religion and culture of western countries. To Father Howard Johnson, I will never forget your kindness, consideration and help. And, thank you to Brother Louis Tomasso, S.S.J. and Brother David Andrews, C.S.C. for telling me all kinds of stories about the history, foods, and languages of the United States. I really appreciate Brother Thomas Vincent, S.S.J. for providing me everything to make a comfortable residence. I wish to express my sincere gratitude to the Franciscan Sisters of St. Joseph for the delicious foods and deserts they prepared for us. I will never forget the days with you, my dear friends, Fr. Etido Samuel Jerome, S.S.J., Fr. Leo Onyekachi Udeagu, S.S.J., Mr. David Begany, and Mr. Randy Grove.

Finally, I wish to give my heartfelt thanks to everyone who offered me invaluable help and assistance. This dissertation would not have been possible without the support of them.

Chapter 1

Introduction

1.1 Review

Many optics-based experimental techniques produce interferograms or fringe patterns, which represent certain physical quantities that can be extracted from the phase distributions of the interferograms. At present, the automatic analysis of interferograms by virtue of the digital image processing techniques has become mature and prevalent. The well known automatic interferogram analysis method is the phase shifting (PS) technique, which yields fast and accurate analysis results from a series of phase-shifted interferograms. The PS technique is widely used for extracting the full-field phase information from interferograms or fringe patterns in a variety of optical measurements [1, 2], such as the moiré technique [3, 4], speckle pattern interferometry [5, 6], three-dimensional profilometry [7–9], and so on. In many cases, e.g., dynamic measurements, however, only a single interferogram for each measurement can be acquired. To analyze such a single interferogram, a number of analysis methods have been developed, such as the Fourier transform (FT) technique [10], windowed Fourier transform (WFT) technique [11–15], wavelet transform (WT) technique [16–18], and so on.

For the interferograms with carrier fringes, the FT technique works well if the carrier frequency is known. In reality, however, the carrier frequency normally cannot be accurately obtained. Furthermore, because the FT is a global operation, the technique is not suitable for accurately detecting the local characteristics of signals. To overcome the limitations of the FT technique, time-frequency techniques have been developed in recent years [19], like the WFT and WT techniques. The difference between the WFT and the WT analyses lies on the selection of a transform window. As opposed to the WFT, the WT has variable window sizes which make the technique more flexible.

Wavelet theory plays an important role in time-frequency analysis, as does the Fourier analysis. Because it has flexible time-frequency analysis windows, or the so-called multi-scale zooming capability, continuous wavelet transform (CWT) is suitable for analyzing a signal that has rich frequency components, for example, an interferogram or fringe pattern [20]. With the concept of the wavelet ridge [21], the one-dimensional CWT (1D-CWT) technique was successfully introduced to analyze different interferograms or fringe patterns [16, 22–25]. To make the CWT technique more robust, the 2D-CWT technique has been further developed for the analysis of fringe patterns acquired by various measurement techniques [26], such as moiré interferometry [17], electronic speckle pattern interferometry [27], and digital holography [28].

For the analysis of a complex interferogram where the fringe orders do not change monotonically, phase ambiguity, i.e., computed phase can have two possible values, is observed in both WFT and WT analyses. A method is proposed [13, 29] combining windowed Fourier ridges (WFR) with regularized phase tracking [30–32] to deal with the high and low frequency parts respectively without introducing phase ambiguity. Based on WFR and phase unwrapping, a frequency-guided algorithm is proposed to demodulate closed fringe patterns

[33, 34]. Compared with these methods, the WT technique has inherent characteristics making it capable of dealing with noise and defects in interferograms [17, 23, 27, 35, 36].

Unlike the most widely used PS technique, the 2D-CWT technique is robust to noise and requires only a single image for fringe pattern analysis. In spite of these advantages, 2D-CWT analysis is generally time-consuming due to the convolution-involved process, which hampers the applications of the technique. To cope with this problem, the fast Fourier transform (FFT) algorithm has been adopted to implement the 2D-CWT technique for fringe pattern analysis[35]. However, the computation time of 2D-CWT analysis is still much longer than that of other popular techniques, such as the PS technique. To further increase the analysis speed, a feasible solution is to choose a small number of discrete parameters instead of continuous dilation and rotation parameters. Some discussions on the choice of the dilation parameters in the 1D-CWT have been presented [37], but a complete and rigorous explanation remains lacking, especially for the 2D-CWT case, where the rotation parameters should be taken into consideration.

In addition, the mother wavelet is an essential component in the wavelet transform, and many mother wavelets have been employed in the 2D-CWT fringe pattern analysis. A typical one is the well-known Gabor wavelet, which was initially used for processing the moiré interferogram [17] and later developed to analyze the speckle fringe pattern [27] as well as the digital hologram [28]. Another commonly used mother wavelet is the Morlet wavelet, and it has been successfully applied to practical optical measurements [35, 38–40]. Furthermore, a number of other notable wavelets, including the Fan wavelet [38], Paul wavelet [36], Mexican wavelet [41], Shannon wavelet [42], and Spline wavelet [42], have also been used in fringe pattern analysis.

As the 2D-CWT fringe pattern analysis technique becomes mature for scientific research

and engineering applications, a few discussions on the parameters of certain mother wavelets have been made to evaluate the performance of the 2D-CWT technique. For instance, a cost function was proposed to employ various scale factors and rotation angles in the 2D-CWT fringe pattern analysis, and a corresponding performance comparison with the 2D FT technique based on analyzing experimental fringe patterns was carried out [40]. In addition, the cover map was used to improve the efficiency of the 2D-CWT technique [43], and the meanings of the 2D-CWT parameters have been elaborated by virtue of this concept. Moreover, with respect to the local stationary length concept, an algorithm on the selection of the window size in the 2D-CWT technique was proposed and adapted for use by the 2D WFT analysis [42, 44]. A detailed comparison of the 2D-CWT and other time-frequency analysis techniques was also recently presented [45].

It is noteworthy, however, that the aforementioned discussions were usually made for certain mother wavelets and with respect to one or two aspects of the 2D-CWT technique. Moreover, the comparisons were conducted based on experimental results, and a fundamental theoretical analysis is lacking. Consequently, it remains unclear which kinds of wavelet(s) should be used in practice.

Finally, although it possesses a number of advantages such as automatic and fast analysis, the PS technique is sensitive to the noise and defects presented in the interferograms as mentioned before, which impairs the application of the technique when noise-free results are demanded. In order to reduce the noise level, a straightforward way is to apply a filtering process to the determined phase data, but this may smear the phase map. A more practical approach is filtering the initial interferograms in advance or filtering the numerator and denominator parts of the arctangent function of the phase calculation formula separately [46]. For interferograms with fringe discontinuities, other schemes, such as filtering

with a mask map and the phasor image processing [47], can be adopted. In recent years, a few new filtering techniques, including the ones use the quadrature filters [48] and the frequency transfer function [49], have also been developed to enhance the noise reduction in the phase-shifting analysis. Despite these advances, the combination of the classic PS technique and the filtering technique is insufficient to correctly obtain the full-field phase map from interferograms that contain defects and corrupted fringes. To cope with the noise and defects simultaneously, a robust adaptive filtering technique with the capability of detecting local fringe information is usually required.

1.2 Objectives

In fringe pattern analysis, compared with other existing techniques, the 2D-CWT technique is more robust to noise and defects, and requires only a single image to fulfill the analysis. This superiority of the 2D-CWT technique has drawn a lot of attentions in recent years. Hence, this dissertation will be mainly focus on the 2D-CWT technique used in fringe pattern analysis.

The purpose of the research is to study the fringe pattern analysis and the wavelet theory thoroughly, identify the issues and problems mentioned in previous section, and find out the solutions so as to improve the efficiency and performance of the 2D-CWT technique. More specifically, the objectives of this dissertation are on the following:

- Reveal the relation between the phase distribution of fringe patterns and the 2D-CWT.
- Develop novel algorithms to remove the phase ambiguity in the analysis by using the 2D-CWT technique.

- Give a complete and rigorous explanation to the parameters of the 2D-CWT and develop efficient algorithms to speed up the 2D-CWT analysis.
- Give a general rule to choose an appropriate mother wavelet in the 2D-CWT analysis by evaluating the commonly used mother wavelets in real applications.
- Develop a method to extract the full-field phase more effectively and accurately by combining the 2D-CWT technique and other popular techniques.

1.3 Contributions

After years of research, our contributions on this area are listed as follows.

1. By investigating the theory of the CWT thoroughly, the relation between the phase distribution of interferograms and the CWT is revealed. Based on this relation, a 2D ridge detection algorithm of the 2D-CWT technique in fringe pattern analysis is introduced. Then, a rigorous proof of the algorithm is given. This is the foundation why the 2D-CWT can be used in fringe pattern analysis.
2. For the analysis of an interferogram where the fringe orders do not change monotonically, an inevitable problem, so called the phase ambiguity (i.e. computed phase can have two possible values), is observed by using any kind of time-frequency analysis techniques, including the 2D-CWT technique. Through analyzing the simulation and real experiments, the reason causing the problem is identified and a rule for phase determination of the 2D-CWT technique is proposed to remove the phase ambiguity.
3. The 2D-CWT analysis is generally time-consuming due to the convolution involved process. Although the FFT algorithm has been employed to implement the 2D-CWT

technique, the computation time is still much longer than that of other popular techniques. By observing the essence of wavelet transform, a complete and rigorous explanation to discretize the dilation and rotation parameters in the 2D-CWT analysis is given. By proposed a concept called the cover map, a new algorithm is developed to further increase the analysis speed without loss the accuracy.

4. In the theory of WT, there is no general rule or theorem to determine which kind of mother wavelet is the best for a specific application. After investigating all kinds of mother wavelets commonly used in fringe pattern analysis, a general rule for the wavelet selection is given and the performance comparison is evaluated.
5. When the variation of the interferogram is large, the phase distribution in such low frequency area might not be determined correctly by using the 2D-CWT technique. Through combining other techniques with the 2D-CWT technique, like the PS technique, a hybrid 2D-CWT technique is developed to extract the full-field phase distributions. Compared with the conventional 2D-CWT technique, the proposed one is more effective and accurate.

1.4 Organization

This dissertation is divided into six chapters to elaborate the 2D-CWT technique in fringe pattern analysis. The first chapter gives a review of the popular techniques used to analyze the interferograms, especially the 2D-CWT technique, in Sec. 1.1. Then, the objectives and contributions of this research are summarized in Secs. 1.2 and 1.3, respectively.

In chapter 2, the optical phenomenon, so called the interference, is included in order to interpret the essence of fringe pattern analysis. After introducing the commonly used inter-

ferometers, the moiré technique is demonstrated as a typical contemporary optical metrology. Then, the mathematical models, which will be used throughout the dissertation, of the intensity and phase distribution of interferograms are generalized at the end of chapter 2. As a comparison, the existing techniques commonly used in fringe pattern analysis are explained in chapter 3, like the PS, FT, and WFT technique.

Chapter 4 elaborates the recent progress of the 2D-CWT technique has been made during this dissertation work. The first two sections interpret the theory of the 2D-CWT mathematically. Then, the basic algorithm of the 2D-CWT is demonstrated based upon the ridge of the 2D-CWT. To cope with the phase ambiguity, a determination rule is proposed in Sec. 4.3. By observing the essence of the WT, in Sec. 4.4, a concept called the cover map is introduced and an efficient algorithm based upon this concept is developed to speed up the 2D-CWT analysis through discretizing the dilation and rotation parameters of the 2D-CWT. Furthermore, the performance of a few commonly used mother wavelets is investigated and evaluated in Sec. 4.5, and it gives a general guidance on the selection of the mother wavelet in the 2D-CWT technique. At the end of chapter 4, a hybrid technique that takes the advantages of both the PS and 2D-CWT techniques is demonstrated to accurately extract the full-field phase distributions from analyzing multiple phase-shifted interferograms. The technique can analyze virtually any kinds of interferograms, including those with phase ambiguities, large fringe-frequency variations, noise, and defects. Computer simulations are carried out to verify the validity and feasibility of the proposed algorithms and concepts in each section.

Chapter 5 presents various real experiments to verify the validity and effectiveness of the algorithms explained in previous chapter. In Chapter 6, as a summary, Sec. 6.1 draws the conclusion of the dissertation. Then, Sec. 6.2 provides the future work in fringe pattern analysis by using the 2D-CWT.

Chapter 2

Optical Interference

In optical metrology, the light wave equation can be expressed in complex form as [50],

$$u(\mathbf{x}, t) = A(\mathbf{x}) \exp\{i[-2\pi\nu t + \phi(\mathbf{x})]\} \quad (2.1)$$

where $i = \sqrt{-1}$ is the imaginary unit, \mathbf{x} denotes the spatial coordinates, t is time, ν means the wave frequency; $A(\mathbf{x}), \phi(\mathbf{x})$ represent the amplitude and phase distribution of the light wave, respectively. Generally, for optic-based experiments, the quantity of interest is the intensity of the light wave. Hence, at a specific time, equation (2.1) can be simplified as

$$u(\mathbf{x}) = A(\mathbf{x}) \exp[i\phi(\mathbf{x})] \quad \text{or} \quad u = A \exp(i\phi) \quad (2.2)$$

In addition, the intensity is usually defined in terms of the irradiance. In optics, the concept of irradiance means the power of light wave irradiates a surface area and can be calculated by averaging the complex amplitude over a time period.

$$I = \langle u, u^* \rangle = \int_0^T uu^* dt \quad (2.3)$$

Then, at a specific time, the intensity is proportional to the complex amplitude as

$$I \propto |u|^2 = uu^* = A^2 \quad (2.4)$$

An interesting issue arises when two coherent light waves are encountered. It shows that the superposed intensity of the two light waves is not simply the addition of the amplitudes. Instead, alternatively dark and bright stripes will be observed. This phenomenon is called the interference and the stripes are called the *interferogram* or *fringe patterns*. And the fringe patterns are related to the phase difference of the two light waves. More specifically, suppose there are two waves defined as

$$u_1 = A_1 \exp(i\phi_1) \quad \text{and} \quad u_2 = A_2 \exp(i\phi_2) \quad (2.5)$$

Then based on the irradiance in Eqs. (2.3) and (2.4), the superposed intensity of the light waves can be obtained as

$$I = A_1^2 + A_2^2 + 2A_1A_2 \cos(\phi_1 - \phi_2) \quad (2.6)$$

Obviously, when the phase difference $\Delta\phi = \phi_1 - \phi_2$ keeps a constant at a specific time, the term $\cos(\Delta\phi)$, so called the interference term, will give the fringe patterns. And, it is the concept of coherent comes from.

The interferograms can be observed in optical experiments by using appropriate instruments which are known as the interferometers. As mentioned before, in order to generate the interferogram, the coherent light waves are needed. And a commonly used way to get the coherent light waves is to split the waves from one light source. Hence, the interferometer generally can be classified as two in terms of the splitting technique [1]. One is called wavefront-dividing interferometers, like the one used in the Young's interference experiment. Another is called amplitude-dividing interferometers, for example, the Michelson interferometer.

2.1 Young's Double-slit Experiment

In 1803, an experiment, which is well known as the Young's Double-slit experiment, was conducted by Thomas Young in order to study the wave-particle duality. In this experiment, two screens are used. One has two slits on it and is put in front of the light source so as to act as an obstacle. The other works as an observation screen and put behind the obstacle one. Based on the particle theory, the light wave should be blocked by the obstacle screen. But in reality, wider alternative dark and bright strips are observed on the observation screen. This phenomenon proves that the light wave has the wave-particle duality. The diagram of the Young's double-slit experiment is shown in Fig. 2.1.

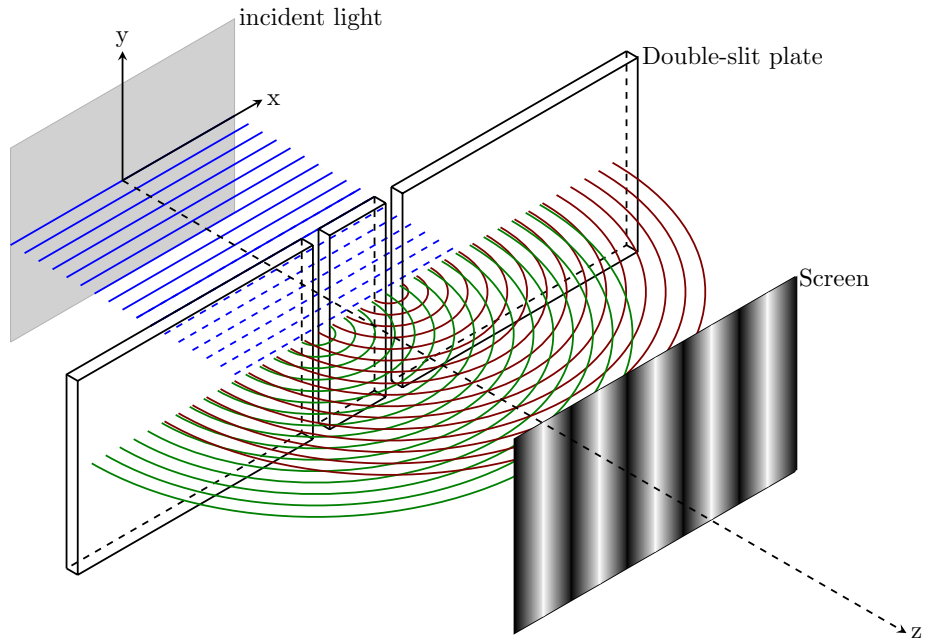


Figure 2.1: The Young's double-slit experiment.

More importantly, one or more physical quantities are related to the fringe patterns [1, 50]. For example, in the Young's double-slit experiment, the wave length λ can be calculated

in terms of the period p of the fringe patterns. For simplification and clarity, the relation is demonstrated in Fig. 2.2.

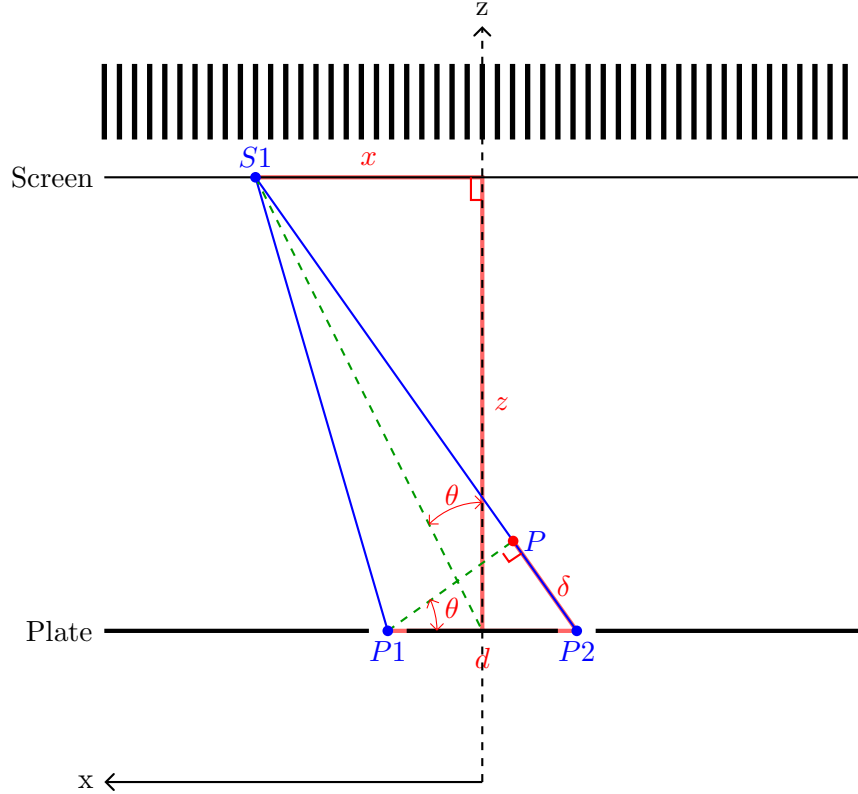


Figure 2.2: Geometric diagram of the Young's double-slit experiment.

When the distance z between the two screens is far enough, i.e. $z \gg d$, which means the far field case, the relation can be induced as

$$\frac{\delta}{d} \approx \frac{x}{z} \quad (2.7)$$

and the phase difference is given by

$$\Delta\phi = 2\pi \frac{\delta}{\lambda} = 2\pi \frac{xd/z}{\lambda} \quad (2.8)$$

Since the dark and bright strips occur when $x = p = \lambda z/d$, equation (2.7) gives a way to calculate the wave length by

$$\lambda = \frac{pd}{z} \quad (2.9)$$

In addition, the intensity of the fringe patterns can be obtained by substituting Eq. (2.8) into Eq. (2.6) as

$$I(x) = I_b + I_a \cos\left(\frac{2\pi d}{\lambda} \frac{x}{z}\right) \quad (2.10)$$

where $I_b = A_1^2 + A_2^2$ and $I_a = 2A_1A_2$.

2.2 Interferometry

Another kind of interferometers is named as amplitude-dividing interferometers, which are more commonly used in modern optical measurements, e.g., the Michelson interferometer. Compared with the wavefront-dividing method, only one light source is needed by amplitude-dividing interferometers to generate the interferogram. Through a beam splitter, the incident light wave is divided as two partial waves which are reflected by mirrors. Then, the interference occurs when the reflected partial waves encounter and different fringe patterns can be observed by adjusting the position of the mirror. The schematic diagram of the Michelson interferometer is shown in Fig. 2.3.

Suppose the displacement of the mirror is denoted as x , then the phase difference is given by

$$\Delta\phi = \frac{2\pi}{\lambda} 2x$$

Hence, according to Eq. (2.6)

$$I(x) = 2I_a \left(1 + \cos \frac{4\pi}{\lambda} x \right) \quad (2.11)$$

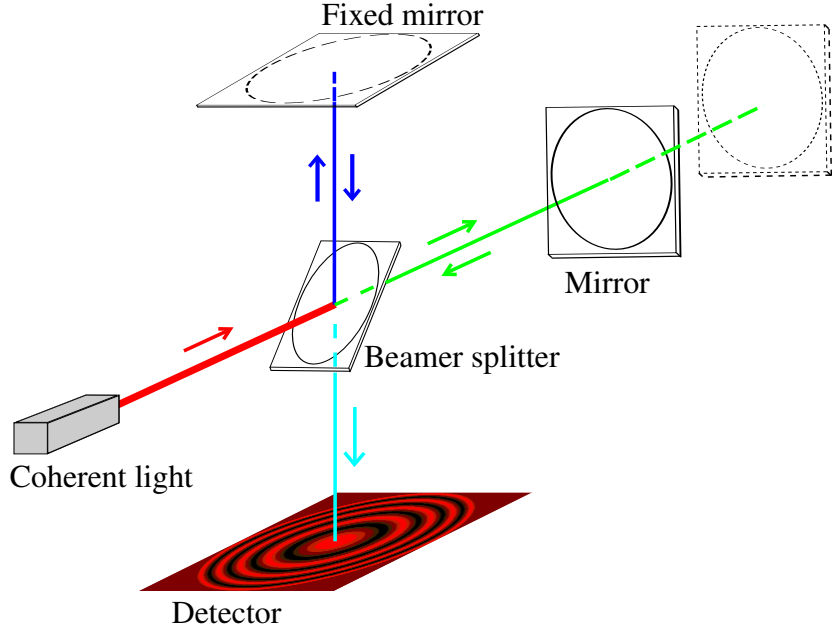


Figure 2.3: Schematic diagram of the Michelson interferometer.

In optics-based experiments, amplitude-dividing interferometers are more popular, such as the Twyman-Green interferometer, the Newton, Fizeau, Haidinger interferometers, and so on. Moreover, in modern optical measurements, there are three kinds of interferometry mainly used in real applications, including the holography, electronic speckle pattern interferometry, which is known as ESPI or TV-holography, and moiré technique [2, 50, 51].

For the sake of conciseness and clarity, only the moiré technique will be introduced in this dissertation as a typical contemporary optical metrology.

2.3 Moiré Technique

Not like the aforementioned interferogram which can merely observed through a particular setup, the moiré interferogram is a quite common optical phenomenon which can be seen

in daily life, for example when two gratings overlap, like through window nets, or fences around a house. And, it is the reason to name the phenomenon as the moiré fringes or moiré pattern. Here, instead of a person's name, moiré is a French word which originally means "an irregular wavy finish on a fabric" [52]. Nowadays, it is used to describe the interference phenomenon which can be observed when two gratings overlap. Two typical examples of the moiré patterns are given in Fig. 2.4.

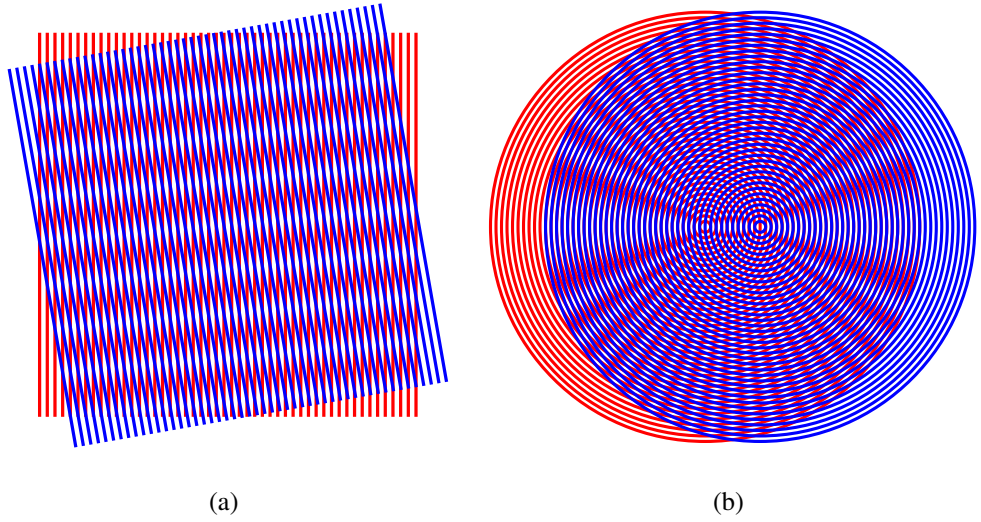


Figure 2.4: The moiré patterns are observed through: (a) two sinusoidal gratings, and (b) two circular gratings.

From Eq. (2.6), the two sinusoidal gratings can be expressed as

$$I_1(x) = A_{11} + A_{12} \cos[\phi_1(x)] \quad \text{and} \quad I_2(x) = A_{21} + A_{22} \cos[\phi_2(x)] \quad (2.12)$$

where $\phi_i(x)$ represent the phase.

When the gratings are superimposed, the multiplication of the equations gives

$$\begin{aligned} I_1(x) \cdot I_2(x) = & A_{11}A_{21} \\ & + A_{12}A_{21} \cos[\phi_1(x)] + A_{11}A_{22} \cos[\phi_2(x)] \\ & + A_{12}A_{22} \cos[\phi_1(x)] \cos[\phi_2(x)] \end{aligned} \quad (2.13)$$

By using the trigonometric transformation technique, the last term can be expressed as

$$\frac{1}{2}A_{12}A_{22} \cos[\phi_1(x) + \phi_2(x)] + \frac{1}{2}A_{12}A_{22} \cos[\phi_1(x) - \phi_2(x)] \quad (2.14)$$

The first term governs the high frequency components of the interferogram and the second term gives the equation of moiré pattern. Moreover, let $\phi(x) = \phi_1(x) - \phi_2(x)$, then the dark and bright stripes of the moiré pattern will appear when $\phi(x) = n\pi, n = 0, 1, 2, \dots$. Hence, the phase distribution of the superimposed gratings can be obtained by measuring the period of the moiré pattern [2].

Many applications are benefit from this conclusion [53–57], for example, the measurement of in-plane displacement due to the displacement

$$U(\mathbf{x}) = p\phi(\mathbf{x}) \quad (2.15)$$

where p is the grating period. Then, the strains can be calculated as [1, 50, 58]

$$\begin{aligned} \varepsilon_x &= p \frac{\partial \phi_x}{\partial x}, \\ \varepsilon_y &= p \frac{\partial \phi_y}{\partial y}, \\ \gamma_{xy} &= p \left(\frac{\partial \phi_x}{\partial y} + \frac{\partial \phi_y}{\partial x} \right) \end{aligned} \quad (2.16)$$

Based on the fundamental theory of moiré pattern, many new techniques have been developed, e.g., the projection fringes technique [8] and shadow moiré technique [59] which are used in vibration analysis, shape or deformation measurements, contouring objects, and other applications.

2.4 Simulation

From Eqs. (2.6), (2.10), (2.11) and (2.14), the general representation of the intensity distribution of interferogram can be modeled as

Definition 1. (*Intensity distribution of interferogram*). Suppose $\mathbf{x} \in \mathbb{R}^2$, the intensity of interferogram $I : R^2 \rightarrow R$ is defined as

$$I(\mathbf{x}) = I_b(\mathbf{x}) + I_a(\mathbf{x}) \cos[\phi(\mathbf{x})] + N(\mathbf{x}) \quad (2.17)$$

where I_b , I_a , and ϕ represent the background, amplitude, and phase distribution of fringe patterns, respectively; $N(\mathbf{x})$ denotes the additive noise.

It needs to be emphasized that due to the limitation of physical devices, e.g., the CCD camera, \mathbf{x} usually is a subset of \mathbb{R}^2 , e.g., $\mathbf{x} \in \mathbb{Z}^2$ instead of $\mathbf{x} \in \mathbb{R}^2$. However, for the purpose of analysis, the mathematical model defined by the above definition is more commonly used.

In reality, many simulated fringe patterns are conducted in order to study the theory and verify the algorithms based on the definition 1. Hence, the most commonly used simulations are introduced here and will be used thoroughly in the following sections. Because the object of fringe patterns analysis are mainly focus on the phase distribution $\phi(\mathbf{x})$, the variety of the simulations exists in the representation of $\phi(\mathbf{x})$.

Definition 2. (*Phase distribution of interferogram*). Suppose $\mathbf{x} \in \mathbb{R}^2$, the phase distribution of interferogram $\phi : R^2 \rightarrow R$ is defined as

$$\phi(\mathbf{x}) = 2\pi \cdot \mathbf{f}_c \cdot \mathbf{x} + \phi_0(\mathbf{x}) \quad (2.18)$$

where \mathbf{f}_c and ϕ_0 represent the normalized carried frequency, and initial phase of fringe patterns, respectively.

Based on Defs. 1 and 2, the simulation of fringe patterns can be generally classified as the monotonic, closed or saddled, and multi-components fringe patterns.

2.4.1 Monotonic Fringe Patterns

The typical monotonic distribution is known as the linear chirp patterns whose phase distribution is represented by using the linear chirp function. The general equation of a linear chirp function in terms of time is

$$f(t) = f_0 + kt \quad (2.19)$$

where f represents the instantaneous frequency, f_0 is the initial frequency, and k denotes the chirp rate. Then, the phase can be obtained from Eq. (2.19) as

$$\phi(t) = \int_0^t f(\tau)d\tau = \left(f_0 + \frac{k}{2}t \right) t \quad (2.20)$$

By adapted for the phase of interferogram in the spatial-time domain, e.g., for the simulation of a interferogram whose phase distribution along the horizontal axis, a simulation function based on Def. 2 can be expressed as

$$\phi(x) = \frac{2\pi}{N} \left[f_0 + \frac{f_1 - f_0}{2(N-1)}x \right] x + \phi_0 \quad (2.21)$$

where N, f_0, f_1, ϕ_0 represent the size, initial frequency, stop frequency, and initial phase, respectively. For example, figure. 2.5 represents a fringe pattern with the size of $N = 512$, the initial and stop frequency of $f_0 = 20$ Hz and $f_1 = 2$ Hz, and the initial phase of $\phi_0 = \pi$.

Similarly, the exponential and quadratic chirp fringe patterns can be simulated by using proper simulation functions.

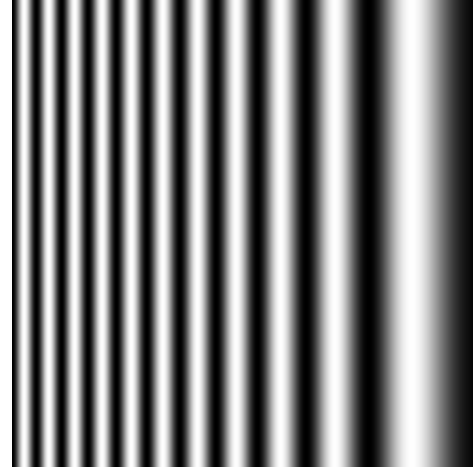


Figure 2.5: Simulated fringe patterns with a linear chirp distribution.

2.4.2 Closed/Saddled Fringe Patterns

Another kind of fringe patterns is more difficult to analysis than the monotonic patterns and is known as the closed fringe patterns. For example, a fringe pattern called the Newton rings can be simulated by using Eq. (2.22).

$$\phi(x, y) = \frac{2\pi}{N\lambda} [(x - x_0)^2 + (y - y_0)^2] + \phi_0 \quad (2.22)$$

where (x_0, y_0) is the center of newton rings, λ denotes the wavelength. For example, figure. 2.6 shows a fringe pattern with $N = 512$, $\lambda = 20$, $(x_0, y_0) = (256, 256)$, and $\phi_0 = \pi$.

Similarly to the Newton rings, if change the addition in Eq. (2.22) to subtraction in Eq. (2.23), then the fringe patterns will be changed to another well known one which is called the saddled fringe patterns here, and an example is shown in Fig. 2.7 with the same parameters used in Fig. 2.6.

$$\phi(x, y) = \frac{2\pi}{N\lambda} [(x - x_0)^2 - (y - y_0)^2] + \phi_0 \quad (2.23)$$

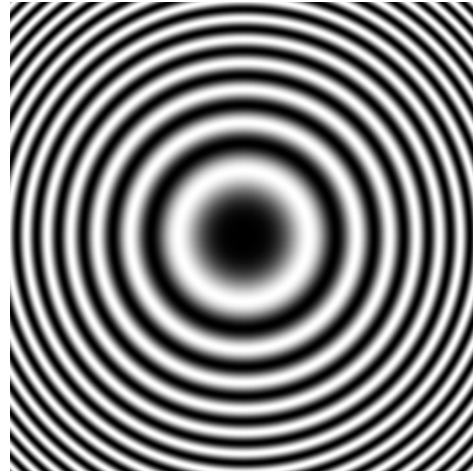


Figure 2.6: Simulated Newton rings.

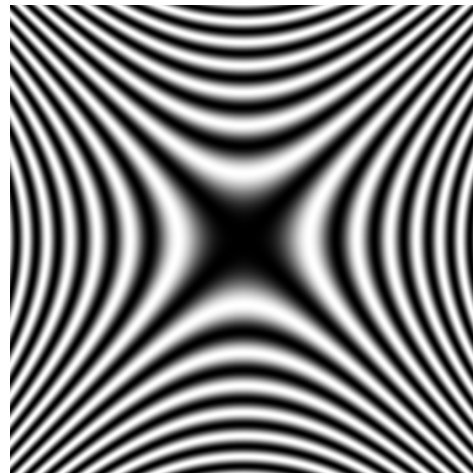


Figure 2.7: Simulated saddled fringe patterns.

2.4.3 Peaks Fringe Patterns

In order to simulate the case more closely to the real application, a complicated fringe pattern in which has a few peaks can be simulated and is so called peaks fringe patterns here. The phase distribution of the peaks fringe patterns is given by

$$\phi(x, y) = \frac{2\pi}{N} \cdot f_c \cdot x + C \cdot p(x, y) + \phi_0 \quad (2.24)$$

where $C \in \mathbb{R}$ is a constant and f_c is the carrier frequency along the x axis. It is worth noting that the fringe patterns with the carrier frequency along other directions can be simulated by adapting Eq. (2.24) accordingly.

For example, $p(x, y)$ can be the `Peaks` function in MATLAB as

$$\begin{aligned} p(x, y) = & 3 \cdot (1 - x)^2 \exp[-x^2 - (y + 1)^2] \\ & - 10 \cdot \left(\frac{x}{5} - x^3 - y^5\right) \exp(-x^2 - y^2) \\ & - \frac{1}{3} \cdot \exp[-(x + 1)^2 - y^2] \end{aligned} \quad (2.25)$$

Figure 2.8 gives an example of fringe patterns in which four peaks exist based on Eqs. (2.24) and (2.25) with $N = 512$, $\phi_0 = \pi$, $C = 3$ and $f_C = 30$ Hz.

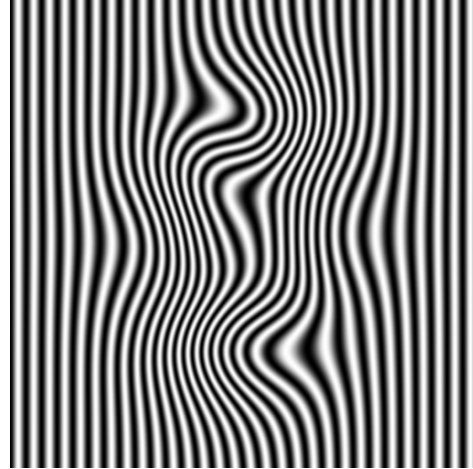


Figure 2.8: Simulated peaks patterns.

Based on Eq. (2.25) so as to vary $p(x, y)$ in Eq. (2.24), a more general equation for peaks fringe patterns can be expressed as

$$p(x, y) = \sum_{i=1}^n a_i \exp\left\{-\frac{5}{N}[(x - x_i)^2 - (y - y_i)^2]\right\} \quad (2.26)$$

where $i \in \mathbb{Z}$; a_i , n , (x_i, y_i) represent the amplitude, number, and the coordinates of peaks, respectively. This kind of fringe patterns can be used to simulate the interference occurs by

struts on a plate. For example, figure 2.9 simulates five struts on a plate and $p(x, y)$ is given by Eq. (2.26) with $n = 5$, $N = 512$, $\mathbf{a} = \{121.0, 85.0, 85.0, 85.0\}$, and the coordinates of peaks are $\{(256, 256), (118, 118), (394, 118), (394, 394), (118, 394)\}$.

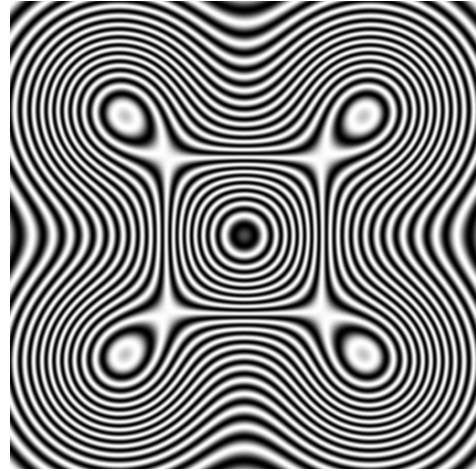


Figure 2.9: Simulated five struts on a plate.

2.4.4 Noise

In real applications, noise issue is always inevitable. From Def. 1 and Eq. (2.17), it can be seen that mainly two kinds of noise exist and affect the intensity of fringe patterns. One is the background noise $I_b(\mathbf{x})$, another is the additive noise $N(\mathbf{x})$. These noises are additive and can be simulated by superposing different images together. For example, by using the `rand` function in MATLAB, the additive white noise $N(\mathbf{x})$ can be simulated. Then, the noisy peaks fringe patterns can be obtained in Fig. 2.10.

Moreover, if takes the object image in Fig. 2.11 (a) as the background image or noise $I_b(\mathbf{x})$, a complicated peaks fringes patterns which is more closely to real application can be simulated as Fig. 2.11 (b) shows.

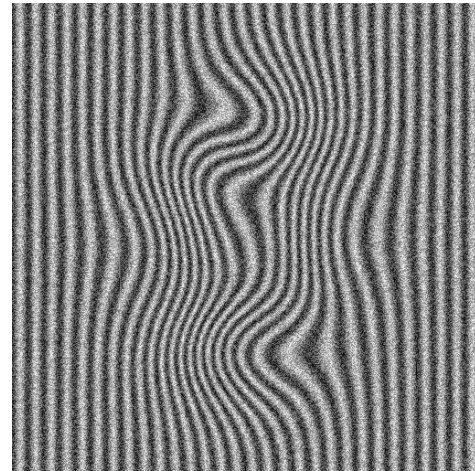


Figure 2.10: Simulated peaks fringe patterns with the additive white noise.

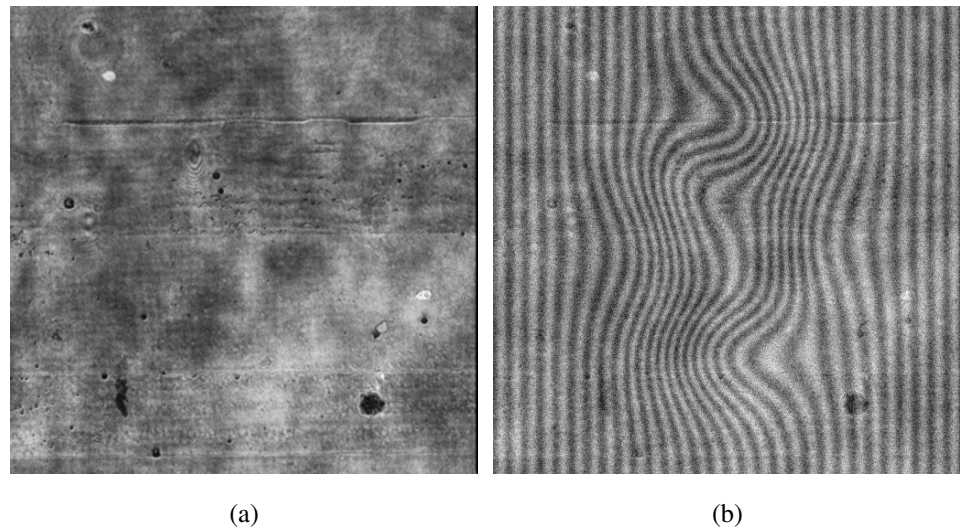


Figure 2.11: Simulated peaks fringe patterns: (a) the object image, and (b) with (a) and the additive white noise.

Chapter 3

Fringe Pattern Analysis

The main concern of fringe pattern analysis exists in the phase information of interferograms. In order to retrieve the phase distribution of interferograms, many techniques have been developed for fringe pattern analysis [1, 60–64]. Usually, the obtained phase distribution is either unwrapped or wrapped. For the wrapped one, unwrapping phase techniques are required [65–74]. Based upon the analysis domain, generally, the existing techniques of fringe pattern analysis can be classified as three categories: spatial-time domain, spatial-frequency domain, and time-frequency domain techniques.

The PS technique is the most widely used spatial-time domain technique for extracting the full-field phase information from interferograms or fringe patterns in a variety of optical measurement methodologies, such as the moiré technique [3, 4], speckle pattern interferometry [5, 6], three-dimensional profilometry [7–9], and so on.

The PS technique is very accurate and efficient but not suitable for the vibration analysis or real time measurements in which only one interferogram can be obtained instead of multiple interferograms. Hence, the spatial-frequency domain technique, which is known as the Fourier transform method (FTM), had been developed to extract the phase information from

a single interferogram.

However, both of the PS and FTM techniques are noise sensitive. In order to improve the result obtained from a single interferogram, the time-frequency domain techniques have been studied in fringe pattern analysis due to their antinoise capability, like the WFT, Wigner-Ville distribution (WVD), and WT techniques.

3.1 Phase Shifting Technique

The intensity of a phase-shifted interferogram or fringe pattern can be mathematically expressed as

$$I_k(\mathbf{x}) = I_b(\mathbf{x}) + I_a(\mathbf{x}) \cos[\phi(\mathbf{x}) + \delta_k] \quad (3.1)$$

where \mathbf{x} is the spatial coordinate, $\{k \in [1, N] \mid k, N \in \mathbb{N}\}$, $N \geq 3$ is the total number of phase-shifting steps, I_k is the intensity of the k th of the N interferograms, I_b is the background intensity, I_a is the modulation amplitude, ϕ is the angular phase, and $\delta_k = \frac{k-1}{N}2\pi$ is the phase-shifting amount.

For the N interferograms, a general algorithm can be found by using the least-squares algorithm [2, 50]. If Eq. (3.1) is expanded with the trigonometric identities and rewritten as

$$I_k(\mathbf{x}) = c_0 + c_1 \cos(\delta_k) + c_2 \sin(\delta_k) \quad (3.2)$$

where

$$c_0 = I_b(\mathbf{x}) \quad (3.3)$$

$$c_1 = I_a(\mathbf{x}) \cos[\phi(\mathbf{x})] \quad (3.4)$$

$$c_2 = -I_a(\mathbf{x}) \sin[\phi(\mathbf{x})] \quad (3.5)$$

Obviously, the phase distribution of the phase-shifted interferograms can be calculated as

$$\phi(\mathbf{x}) = \tan^{-1} \left(-\frac{c_2}{c_1} \right) \quad (3.6)$$

If write $\{I_k\}$ in matrix form and take advantages of the least-squares method, the coefficients of Eq. (3.2) can be solved through

$$\begin{pmatrix} c_0 \\ c_1 \\ c_2 \end{pmatrix} = A^{-1}B \quad (3.7)$$

where

$$A = \begin{pmatrix} N & \sum \cos(\delta_k) & \sum \sin(\delta_k) \\ \sum \cos(\delta_k) & \sum \cos^2(\delta_k) & \sum \cos(\delta_k) \sin(\delta_k) \\ \sum \sin(\delta_k) & \sum \cos(\delta_k) \sin(\delta_k) & \sum \sin^2(\delta_k) \end{pmatrix} \quad (3.8)$$

and

$$B = \begin{pmatrix} \sum I_k \\ \sum I_k \cos(\delta_k) \\ \sum I_k \sin(\delta_k) \end{pmatrix} \quad (3.9)$$

Based upon this least-squares algorithm and from Eq. (3.9), a complex signal can be constructed by using the N interferograms as

$$I(\mathbf{x}) = \sum_{k=1}^N I_k(\mathbf{x}) \cos(\delta_k) - i \sum_{k=1}^N I_k(\mathbf{x}) \sin(\delta_k) \quad (3.10)$$

where i is the imaginary unit. Substituting Eq. (3.1) into Eq. (3.10), and considering that the background intensity I_b will not change among the phase-shifted interferograms, and $\sum_{k=1}^N \sin(\delta_k) = 0$, $\sum_{k=1}^N \cos(\delta_k) = 0$, $\sum_{k=1}^N \sin(\phi + 2\delta_k) = 0$ and $\sum_{k=1}^N \cos(\phi + 2\delta_k) = 0$ for any ϕ , equation (3.10) can be simplified as

$$I(\mathbf{x}) = \frac{N}{2} I_a(\mathbf{x}) \exp[i\phi(\mathbf{x})] \quad (3.11)$$

It is noted that from Eqs. (3.10) and (3.11), the phase ϕ can be calculated as

$$\phi(\mathbf{x}) = \tan^{-1} \left[-\frac{\sum_{k=1}^N I_k(\mathbf{x}) \sin(\delta_k)}{\sum_{k=1}^N I_k(\mathbf{x}) \cos(\delta_k)} \right] \quad (3.12)$$

Equation (3.12) is the general governing equation of the conventional N -frame phase-shifting algorithm from the least-squares analysis. Although the equation is very simple, it can be seen that the noise and errors in I_k will be easily passed to the calculated phase ϕ . For this reason, the phase-shifting algorithm is vulnerable to the noise and defects presented in the interferograms.

Specifically, the most commonly used PS technique is the four-frame technique [1, 50]. According to Eq. (3.1), the intensity of the interferogram for each frame can be expressed as

$$I_k(\mathbf{x}) = I_b(\mathbf{x}) + I_a(\mathbf{x}) \cos[\phi(\mathbf{x}) + \delta_k] \quad (3.13)$$

where $k = \{1, 2, 3, 4\}$ and $\delta_k = \{0, \pi/2, \pi, 3\pi/2\}$. And based upon the fact that the background and signal intensity will not change during the phase shifting process, a complex signal can be constructed by eliminating the background as,

$$I(\mathbf{x}) = (I_4 - I_2) + i(I_3 - I_2) = 2I_a(\mathbf{x}) \exp \{i \cos[\phi(\mathbf{x})]\} \quad (3.14)$$

Hence, the phase distribution can be determined by

$$\phi(\mathbf{x}) = \tan^{-1} \left(\frac{I_4 - I_2}{I_3 - I_2} \right) \quad (3.15)$$

However, the PS technique is sensitive to the noise and defects presented in the interferograms, which impairs the application of the technique when noise-free results are demanded. In order to reduce the noise level, a straightforward way is to apply a filtering process to the determined phase data, but this may smear the phase map. A more practical approach is filtering the initial interferograms in advance or filtering the numerator and denominator parts

of the arctangent function of the phase calculation formula separately [46]. For interferograms with fringe discontinuities, other schemes, such as filtering with a mask map and the phasor image processing [47], can be adopted. In recent years, a few new filtering techniques, including the ones use the quadrature filters [48] and the frequency transfer function [49], have also been developed to enhance the noise reduction in the phase-shifting analysis. Despite these advances, the combination of the classic phase-shifting technique and the filtering technique is insufficient to correctly obtain the full-field phase map from interferograms that contain defects and corrupted fringes. To cope with the noise and defects simultaneously, a robust adaptive filtering technique with the capability of detecting local fringe information is usually required.

3.2 Fourier Transform Technique

The PS technique is very accurate and efficient but needs multiple interferograms to estimate the phase information. In some cases, only one interferogram can be obtained instead of multiple interferograms, for example, in the vibration analysis or real time measurements. As mentioned before, the PS technique cannot be used in such case. Hence, the FTM was developed by Takeda et al in 1982 [10] to extract the phase information from a single interferogram.

The basic theory of the FTM can be described as follows [1]. Suppose the intensity of fringe patterns with a carrier frequency is expressed as

$$I(\mathbf{x}) = I_b(\mathbf{x}) + I_a(\mathbf{x}) \cos[\omega_c \cdot \mathbf{x} + \phi(\mathbf{x})] \quad (3.16)$$

where ω_c is the carrier frequency in radians. According to the Euler's formula, equation

(3.16) can be written as

$$I(\mathbf{x}) = I_b(\mathbf{x}) + I_A(\mathbf{x}) \exp(i\omega_c \cdot \mathbf{x}) + I_A^*(\mathbf{x}) \exp(-i\omega_c \cdot \mathbf{x}) \quad (3.17)$$

where

$$I_A(\mathbf{x}) = \frac{1}{2} I_a(\mathbf{x}) \exp[i\phi(\mathbf{x})] \quad (3.18)$$

Then the Fourier transform of $I(\mathbf{x})$ is given by

$$\mathcal{F}[I(\mathbf{x})] = \hat{I}(\boldsymbol{\omega}) = \hat{I}_b(\boldsymbol{\omega}) + \hat{I}_A(\boldsymbol{\omega} - \boldsymbol{\omega}_c) + \hat{I}_A^*(\boldsymbol{\omega} + \boldsymbol{\omega}_c) \quad (3.19)$$

Obviously, three parts of information exist in the spectra. The first term gives the DC (direct current) component of the intensity. The low frequency and high frequency component are given by the second and third term, respectively.

As Fig. 3.1 shows, if the carrier frequency ω_c is high enough so as to separate the \hat{I}_A from \hat{I}_b , then a filter $H(\boldsymbol{\omega} - \boldsymbol{\omega}_c)$ can be employed to extract $\hat{I}_A(\boldsymbol{\omega} - \boldsymbol{\omega}_c)$. Through a demodulation and taking the inverse Fourier transform of \hat{I}_A , the phase distribution of fringe patterns $\phi(\mathbf{x})$ can be obtained by using Eq. (3.20) based upon Eq. (3.18).

$$\phi(\mathbf{x}) = \tan^{-1} \left\{ \frac{\Im[I_A(\mathbf{x})]}{\Re[I_A(\mathbf{x})]} \right\} \quad (3.20)$$

where \Im and \Re denote the imaginary and real part of complex number, respectively.

The FTM gives a great idea to extract the phase information from a single interferogram. But the problem is that the useful frequency component \hat{I}_A might not be isolated from \hat{I}_b in reality. For example, if the carrier frequency is not high enough, then \hat{I}_A and \hat{I}_b will be entangled together. In addition, if there is another kind of noise existing, e.g., the additive white noise, \hat{I}_A obviously cannot be obtained directly. In another word, the FTM is noise sensitive. Hence, many efforts are taken to solve this issue and a lot of new techniques have been developed to improve the results, for example, time-frequency analysis techniques.

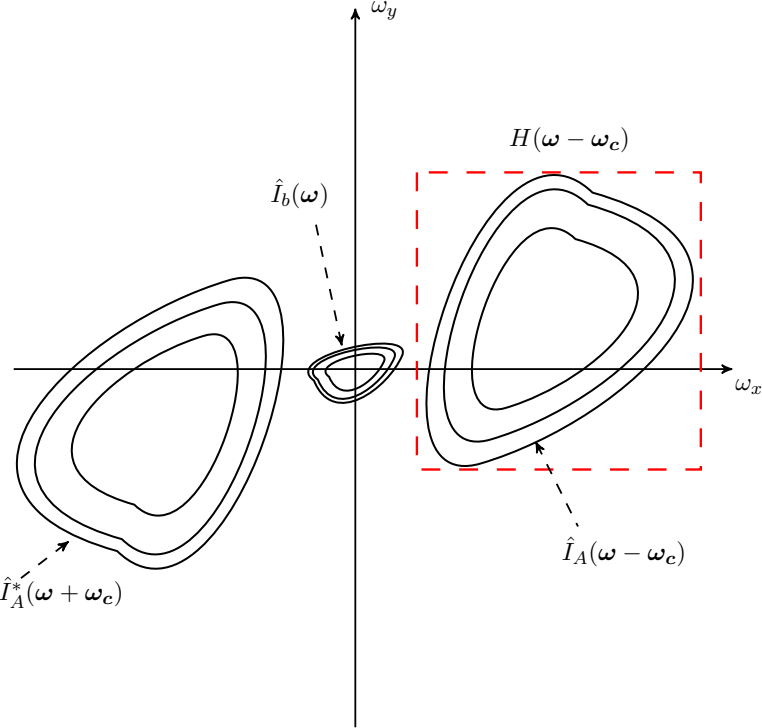


Figure 3.1: Schematic diagram of the Fourier transform method.

3.3 Time-frequency Analysis Technique

For interferograms with carrier fringes, the FTM works well if the carrier frequency ω_c is known. In reality, however, ω_c normally cannot be accurately obtained. Furthermore, because the FT is a global operation, the FTM is not suitable for accurately detecting the local characteristics of signals. To overcome the limitations of the FT technique, time-frequency analysis techniques have been developed in recent years. In fringe pattern analysis, the dominated techniques in the time-frequency domain are the WFT and CWT technique. The basic theory of the WFT technique used to extract the phase distribution of fringe patterns is introduced briefly in this section. In Chapter 4, the CWT technique will be elaborated thoroughly. Due to the immaturity, the WVD technique will not be discussed but the technical details

can be found at [58, 75, 76].

As mentioned in Eq. (3.18), suppose the intensity of phase shifting interferograms can be expressed as

$$I(\mathbf{x}) = I_a(\mathbf{x}) \exp[i\phi(\mathbf{x})] \quad (3.21)$$

And the Short-time fourier transform (STFT) is to analyze $I(\mathbf{x})$ locally by using a window function, and it is also called the WFT. For instance, the STFT of $I(\mathbf{x})$ is given by

$$\mathcal{S}(\mathbf{u}, \boldsymbol{\sigma}, \boldsymbol{\omega}) = \int_{\mathbb{R}^2} I(\mathbf{x}) w_{\mathbf{u}, \boldsymbol{\sigma}}(\mathbf{x}) \exp(-i\boldsymbol{\omega} \cdot \mathbf{x}) d^2\mathbf{x} \quad (3.22)$$

where $\boldsymbol{\omega}$ denotes the frequency coordinates, and $w_{\mathbf{u}, \boldsymbol{\sigma}}$ is window functions, e.g., the Gaussian functions which are defined as

$$w_{\mathbf{u}, \boldsymbol{\sigma}}(\mathbf{x}) = g_{\mathbf{u}, \boldsymbol{\sigma}}(\mathbf{x}) = \exp\left(-\frac{|\mathbf{x} - \mathbf{u}|^2}{2\boldsymbol{\sigma}^2}\right) \quad (3.23)$$

In a local region, i.e. around a point \mathbf{u} , the amplitude of $I(\mathbf{x})$ can be treated as a constant and the phase of $I(\mathbf{x})$ is linear so that

$$\begin{cases} I_a(\mathbf{x}) = I_a(\mathbf{u}) \\ \phi(\mathbf{x}) = \phi(\mathbf{u}) + (\mathbf{x} - \mathbf{u}) \nabla \phi(\mathbf{u}) \end{cases} \quad (3.24)$$

By substituting Eq. (3.24) into Eq. (3.22), it gives

$$\begin{aligned} \mathcal{S}'(\mathbf{u}, \boldsymbol{\sigma}, \boldsymbol{\omega}) &= \exp(i\boldsymbol{\omega} \cdot \mathbf{u}) \mathcal{S}(\mathbf{u}, \boldsymbol{\sigma}, \boldsymbol{\omega}) \\ &= \boldsymbol{\sigma} I_a(\mathbf{u}) \exp[i\phi(\mathbf{u})] \hat{g}\{\boldsymbol{\sigma}[\boldsymbol{\omega} - \nabla \phi(\mathbf{u})]\} \end{aligned} \quad (3.25)$$

By observing Eq. (3.25), it shows that the angle of \mathcal{S}' is relate to the phase ϕ if \hat{g} has a unique maximum at some point. Hence, the phase of $I(\mathbf{x})$ can be estimated from \mathcal{S}' as

$$\phi(\mathbf{x}) = \tan^{-1}[\mathcal{S}'(\mathbf{u}, \boldsymbol{\sigma}, \boldsymbol{\omega}_r)] + \boldsymbol{\omega}_r \cdot \mathbf{u} \quad (3.26)$$

where

$$\omega_r = \arg \max_{\omega \in \mathbb{R}^2} \{|\mathcal{S}'(\mathbf{u}, \sigma, \omega)|\} \quad (3.27)$$

Hence, ω_r is so called the ridges and this method is named as the windowed Fourier Ridges (WFR) [11, 13]. Compared to the FTM, the WFR is more robust and has a better anti-noise performance which WT techniques also have. The difference between the WFT and the WT analyses lies on the selection of a transform window [77]. As opposed to the WFT, the WT has variable window sizes which make the technique more flexible.

Chapter 4

2D-CWT in Fringe Pattern Analysis

In time-frequency analysis, in terms of the representation, it can be roughly classified as two categories: linear analysis, like the Fourier-type and wavelet-type; quadratic analysis, like the Cohen's class and affine class [78]. Specifically, the most well known transforms in the time-frequency analysis are the STFT, WT and WVD [78–80]. The STFT, also known as the WFT, is one of the most successful time-frequency analysis techniques in signal processing. Compared to the STFT, the WT had drawn a lot of attentions afterward due to the more flexible time-frequency window size, especially in the last two decades of the twentieth century.

Although the study of the WT in the sense of mathematics had appeared back to the early twentieth century, the time when the WT became a hot topic was in the 1980s due to the research in physics and engineering [81, 82]. Then, many mathematicians, scientists, and engineers took a lot of efforts in the research of the theory of WT [83–86] and numerous applications of the WT emerged [87–91], like signal and image processing[86], geophysics[92], medicine and biology[93], physics[94], etc..

The more mature studies of the WT is in the discrete WT (DWT), and many efforts

were taken into the construction of orthogonal wavelet bases and perfect reconstruction [84]. Based upon the theory and fast implementation algorithm of DWT, the WT techniques had been successfully used in numerous areas, such as denoising, compression, edge detection, linear and nonlinear approximations, and so on [86]. For the CWT, it is usually used in analysis and theoretical studies. However, after years of study by a lot of researchers, the CWT had been proved as a powerful tool in theory and real applications, like object detection and recognition, image retrieval and denoising, fractals and texture analysis, etc. [95].

As an excellent analysis technique, in recent years, CWT undoubtedly has drawn broad interests on fringe pattern analysis since it is robust and particularly helpful for detecting the characteristics of local fringes. With the concept of the wavelet ridge [21, 96], the 1D-CWT technique was successfully introduced to analyze different interferograms or fringe patterns [16, 22, 23, 97]. Compared with the 1D-CWT technique, the 2D-CWT one is more suitable for interferogram analysis due to antinoise capability [98, 99]. Then, in order to make the CWT technique more robust, the 2D-CWT technique has been further developed for the analysis of fringe patterns acquired by various measurement techniques [26], such as moiré interferometry [17, 35, 100], projection fringe pattern [38, 45], laser interferogram [39, 101], electronic speckle pattern interferometry [27, 102], and digital holography [28].

4.1 2D-CWT

4.1.1 Definition

The 2D-CWT is defined in the spatial domain or spatial-time domain as [95]

$$\mathcal{W}(\mathbf{u}, s, \theta) \equiv \langle f, \psi_{\mathbf{u}, s, \theta} \rangle = \int_{\mathbb{R}^2} f(\mathbf{x}) \psi_{\mathbf{u}, s, \theta}^*(\mathbf{x}) d^2\mathbf{x} \quad (4.1)$$

where $\mathbf{x} \in \mathbb{R}^2$ is the spatial coordinates, $f \in L^2(\mathbb{R}^2)$ represents a 2D finite energy signal, r_θ is the conventional 2×2 rotation matrix with respect to θ in Eq. (4.2),

$$r_\theta \equiv \begin{pmatrix} \cos \theta & -\sin \theta \\ \sin \theta & \cos \theta \end{pmatrix} \quad (4.2)$$

and the symbol $*$ denotes the complex conjugate operator. Generally, $\psi(\mathbf{x}) \in L^1(\mathbb{R}^2) \cap L^2(\mathbb{R}^2)$ is called the mother wavelet, and $\psi_{\mathbf{u},s,\theta}$ represents the family of wavelets, or called the daughter wavelets which is defined in Eq. (4.3)

$$\psi_{\mathbf{u},s,\theta}(\mathbf{x}) = \psi [s^{-1}r_{-\theta}(\mathbf{x} - \mathbf{u})] \quad (4.3)$$

where $\mathbf{u} \in \mathbb{R}^2$ is a translation parameter, $s \in \mathbb{R}_+$ is a scale factor, $\theta \in [0, 2\pi)$ or $[-\pi, \pi)$ is a rotation angle.

Based on the theory of wavelet analysis and the Eq. (4.1), any $f \in L^2(\mathbb{R}^2)$ can be reconstructed from the wavelet coefficients as

$$f(\mathbf{x}) = \frac{1}{c_\psi} \int_{\mathbb{R}^2 \times \mathbb{R}_+ \times [0,2\pi)} \mathcal{W}(\mathbf{u}, s, \theta) \psi_{\mathbf{u},s,\theta}(\mathbf{x}) d\mathbf{u} \frac{ds}{s} d\theta \quad (4.4)$$

if and only if the constant c_ψ satisfies

$$c_\psi \equiv \int_{\mathbb{R}^2} |\hat{\psi}(\boldsymbol{\omega})|^2 \frac{d^2\boldsymbol{\omega}}{|\boldsymbol{\omega}|^2} < \infty \quad (4.5)$$

where $\hat{\cdot}$ denotes the Fourier transform and $\boldsymbol{\omega}$ represents spatial-frequency coordinates in radians. Then, equation (4.5) is called the admissibility condition which implies the mother wavelet have the feature as $\hat{\psi}(\mathbf{0}) = 0$ or $\int_{\mathbb{R}^2} \psi(\mathbf{x}) d\mathbf{x} = 0$.

In real applications, the 2D-CWT is usually normalized in terms of amplitude or energy for analysis purpose, and this normalization is called L^1 -normalization or L^2 -normalization in mathematics, respectively. For example, under L^1 -normalization, equation (4.1) will be

$$\mathcal{W}(\mathbf{u}, s, \theta) = s^{-2} \int_{\mathbb{R}^2} f(\mathbf{x}) \psi^*[s^{-1}r_{-\theta}(\mathbf{x} - \mathbf{u})] d^2\mathbf{x} \quad (4.6)$$

Moreover, if the Fourier transform of f exists which means $f \in L^1(\mathbb{R}^2) \cap L^2(\mathbb{R}^2)$, then according to the Plancherel theorem in Eq. (4.7),

$$\langle f, g \rangle = \langle \hat{f}, \hat{g} \rangle \quad (4.7)$$

the definition of the 2D-CWT in the spatial-frequency domain under L^1 -normalization can be obtained in Eq. (4.8)

$$\mathcal{W}(\mathbf{u}, s, \theta) \equiv \langle \hat{f}, \hat{\psi}_{\mathbf{u}, s, \theta} \rangle = s^2 \int_{\mathbb{R}^2} \hat{f}(\boldsymbol{\omega}) \hat{\psi}^*[sr_{-\theta}(\boldsymbol{\omega})] e^{i\cdot\boldsymbol{\omega}\cdot\mathbf{u}} d^2\boldsymbol{\omega} \quad (4.8)$$

4.1.2 2D Wavelet Ridge

Suppose the signal $f(\mathbf{x})$, e.g. the wave equation, has such form,

$$f(\mathbf{x}) = A(\mathbf{x}) \exp[i\phi(\mathbf{x})] \quad (4.9)$$

by using the Taylor series expansion for $f(\mathbf{x})$ around $\mathbf{x} = \mathbf{u}$, which gives

$$f(\mathbf{x} + \mathbf{u}) = [A(\mathbf{u}) + \mathbf{x}\nabla A(\mathbf{x}) + \dots] \exp[i(\phi(\mathbf{u}) + \mathbf{x}\nabla\phi(\mathbf{u}) + \dots)] \quad (4.10)$$

then substitute Eq. (4.10) into Eq. (4.1) and an approximation of its 2D-CWT can be derived as [86, 95, 96, 99]

$$\mathcal{W}(\mathbf{u}, s, \theta) = A(\mathbf{u}) \exp[i\phi(\mathbf{u})] \hat{\psi}^*\{sr_{-\theta}[\nabla\phi(\mathbf{u})]\} + R(\mathbf{u}, s, \theta) \quad (4.11)$$

where ∇ represents the gradient operator, R is a higher order remainder that can be estimated by using Eq. (4.12),

$$|R(\mathbf{u}, s, \theta)| \leq s^2 \sup_{s^{-1}\mathbf{x} \in \Omega_\psi} |\nabla A(\mathbf{x})| \quad (4.12)$$

where Ω_ψ means the compact supported domain of the wavelets ψ .

Suppose $\hat{\psi}^*$ has a unique maximum at a certain position denoted as $\boldsymbol{\omega}_0$, by observing Eq. (4.11), an important fact is revealed that the energy of the 2D-CWT will reach the

maximum when $\hat{\psi}^*$ reaches the maximum, i.e. $\hat{\phi}^*(\omega_0)$. When this case occurs, it means that $sr_{-\theta}[\nabla\phi(\mathbf{u})] = \omega_0$ and gives the parameters (s_0, θ_0) of \mathcal{W} at the point \mathbf{u}_0 as

$$s_0 = \frac{|\omega_0|}{|\nabla\phi(\mathbf{u})|}, \quad \theta_0 = \frac{\langle \omega_0, \nabla\phi(\mathbf{u}) \rangle}{|\omega_0||\nabla\phi(\mathbf{u})|} \quad (4.13)$$

This fact shows that the phase information of $f(\mathbf{x})$ in Eq. (4.9) can be obtained from its wavelet coefficients \mathcal{W} . Obviously, it requires the wavelet function $\hat{\psi}^*$ is compact support and has a unique maximum at certain point, and this condition is not difficult to be satisfied, for example, the Gaussian function. Then, such points, $(\mathbf{u}_0, s_0, \theta_0)$, are called the wavelet ridges. Furthermore, the phase information of the interferogram is contained in the wavelet coefficients and can be extracted directly at wavelet ridges.

4.2 Direct Ridge Detection Algorithm

Based on the concept of wavelet ridge introduced above, an algorithm called the direct ridge detection (DRD) algorithm can be conducted to find the ridges among the wavelet coefficients. Then, the phase $\phi(\mathbf{x})$ of signals can be estimated by using the ridges. Equation (4.11) is a generic rule for any kind of mother wavelet. It was firstly used in signal processing to analyze instantaneous frequency of 1D signals [96] and 2D cases [99]. In 2004, the 1D-DRD algorithm was introduced in the moiré interferogram [23]. Then, the 2D case in speckle fringe patterns was proposed in 2009 [27].

4.2.1 Algorithm

Generally, according to Eq. (2.17) in Sec. 2.4, the intensity of an interferogram can be simplified as

$$I(\mathbf{x}) = I_b(\mathbf{x}) + I_a(\mathbf{x}) \cos[\phi(\mathbf{x})] \quad (4.14)$$

Moreover, when performing the wavelet analysis of fringe patterns, I_b and I_a can usually be treated as constants in a local region. Based on this assumption, I_b will contribute nothing to the wavelet coefficients because of the admissibility condition which means

$$\int I_b(\mathbf{x})\psi(\mathbf{x})d\mathbf{x} = 0 \quad (4.15)$$

And Eq. (4.11) is still available for the second term in Eq. (4.14) [86, 99]. It is worth noting that the reminder term in Eq. (4.11) will be different and more precise approximations of wavelet coefficients can be derived by using the stationary phase method [99, 103, 104].

Hence, the DRD algorithm can be described as follows [39]. Suppose the value of wavelet ridges are denoted as

$$\mathcal{W}(\mathbf{u})_{\text{ridge}} = \mathcal{W}(\mathbf{u}, s_{\text{ridge}}, \theta_{\text{ridge}}) \quad (4.16)$$

where

$$(s_{\text{ridge}}, \theta_{\text{ridge}}) = \arg \max_{\substack{s \in \mathbb{R}^+ \\ \theta \in [0, 2\pi)}} \{|\mathcal{W}(\mathbf{u}, s, \theta)|\} \quad (4.17)$$

Then, the phase at \mathbf{u} can be calculated from

$$\phi(\mathbf{u}) = \tan^{-1} \left\{ \frac{\Im[\mathcal{W}(\mathbf{u})_{\text{ridge}}]}{\Re[\mathcal{W}(\mathbf{u})_{\text{ridge}}]} \right\} \quad (4.18)$$

where \Im and \Re denote imaginary and real parts of a complex value, respectively.

The DRD algorithm is very useful in fringe patterns analysis due to it builds up the relation between the phase distribution of fringe patterns and the wavelet transform. That means the phase information can be estimated from the wavelet coefficients by using Eq. (4.18) when the 2D-CWT is applied to an interferogram.

The intensity of an interferogram, which is defined in Eq. (2.17) or the simplified version in Eq. (4.14), obviously is a 2D finite energy signal. Then the DRD algorithm is applicable

in fringe pattern analysis. More specifically, if the intensify $I(\mathbf{x})$ is rewritten as

$$I(\mathbf{x}) = I_b + I_a \cos [2\pi S^{-1} \mathbf{n} \cdot (\mathbf{x} - \mathbf{u}) + \phi(\mathbf{u})] \quad (4.19)$$

where I_b and I_a are treated as constants in the local region as mentioned before; $\mathbf{n} = (\cos \Theta, \sin \Theta)$ as the normal vector. When employs a typical 2D Morlet wavelet (actually the truncated Morlet wavelet and the details will be discussed in Sec. 4.5) which is defined as,

$$\psi_M(\mathbf{x}) = \exp(i\omega_0 \cdot \mathbf{x}) \exp\left(-\frac{1}{2}|\mathbf{x}|^2\right) \quad (4.20)$$

Then the analytical solution of the WT of $I(\mathbf{x})$ can be found as

$$\begin{aligned} \mathcal{W}(\mathbf{u}, s, \theta) &= 2\pi I_b \exp(-2\pi^2) \\ &+ \pi I_a \exp\left(-2\pi^2 \left\{ \left(\frac{s}{S} - 1\right)^2 + 2\frac{s}{S} [1 - \cos(\Theta - \theta)] \right\}\right) \exp[i\phi(\mathbf{u})] \\ &+ \pi I_a \exp\left(-2\pi^2 \left\{ \left(\frac{s}{S} + 1\right)^2 - 2\frac{s}{S} [1 - \cos(\Theta - \theta)] \right\}\right) \exp[-i\phi(\mathbf{u})] \end{aligned} \quad (4.21)$$

Equation (4.21) shows that the energy of the 2D-CWT, or the coefficient modulus, reaches maximum at the ridges which are $(\mathbf{u}, s = S, \theta = \Theta)$, and the corresponding wavelet coefficient is

$$\mathcal{W}(\mathbf{u}, s, \theta)_{\text{ridge}} = 2\pi I_b \exp(-2\pi^2) + \pi I_a \exp[i\phi(\mathbf{u})] + \pi I_a \exp(-8\pi^2) \exp[-i\phi(\mathbf{u})] \quad (4.22)$$

Obviously, the second term of Eq. (4.22) will dominate the value at the ridges. Hence,

$$\mathcal{W}(\mathbf{u}, s, \theta)_{\text{ridge}} \approx \pi I_a \exp[i\phi(\mathbf{u})] \quad (4.23)$$

It verifies the validity of Eq. (4.11) and a fact can be seen that the phase information of the interferogram is contained in the wavelet coefficient in a simple form, and thus can be extracted directly.

In order to show the feasibility, a simulated fringe patterns is shown in Fig. 4.1 (a) and the phase distribution extracted by using the DRD algorithm is shown in Fig. 4.1 (b).

4.2.2 Phase Ambiguity

When dealing with an interferogram in which the fringe orders change monotonically, this issue does not bring problems to phase determination with the DRD algorithm as mentioned in previous section. However, when the algorithm is applied to analyze non-monotonic interferogram, like the peaks fringe patterns described in Sec. 2.4.3, although the ridges can be correctly determined as Fig. 4.2 (a) shows, the phase determination can be ambiguous in Fig. 4.2 (b).

The fundamental reason of the phase ambiguity is that a single interferogram does not contain the sign information of phase gradients, so any algorithm using solely a single interferogram cannot distinguish between positive and negative gradients. Mathematically, the phase ambiguity of 2D-CWT can also be described as owing to the following property of the rotation matrix:

$$r_\theta(\mathbf{x}) = -r_{\pi+\theta}(\mathbf{x}) \quad (4.24)$$

This leads to

$$|\mathcal{W}(\mathbf{u}, s, \theta)| = |\mathcal{W}(\mathbf{u}, s, \pi + \theta)| \quad (4.25)$$

Eq. (4.25) indicates that the magnitude of the 2D-CWT wavelet coefficient is presented as a periodical signal of period π with respect to the rotation angle. This is demonstrated by a representative plot in Fig. 4.3.

Additionally, a careful observation on Eq. (4.21) reveals that at point $(\mathbf{u}, s = S, \theta = \pi + \Theta)$, the wavelet coefficient can be simplified as

$$\mathcal{W}(\mathbf{u}, s, \theta) = 2\pi I_b \exp(-2\pi^2) + \pi I_a \exp(-8\pi^2) \exp[i\phi(\mathbf{u})] + \pi I_a \exp[-i\phi(\mathbf{u})] \quad (4.26)$$

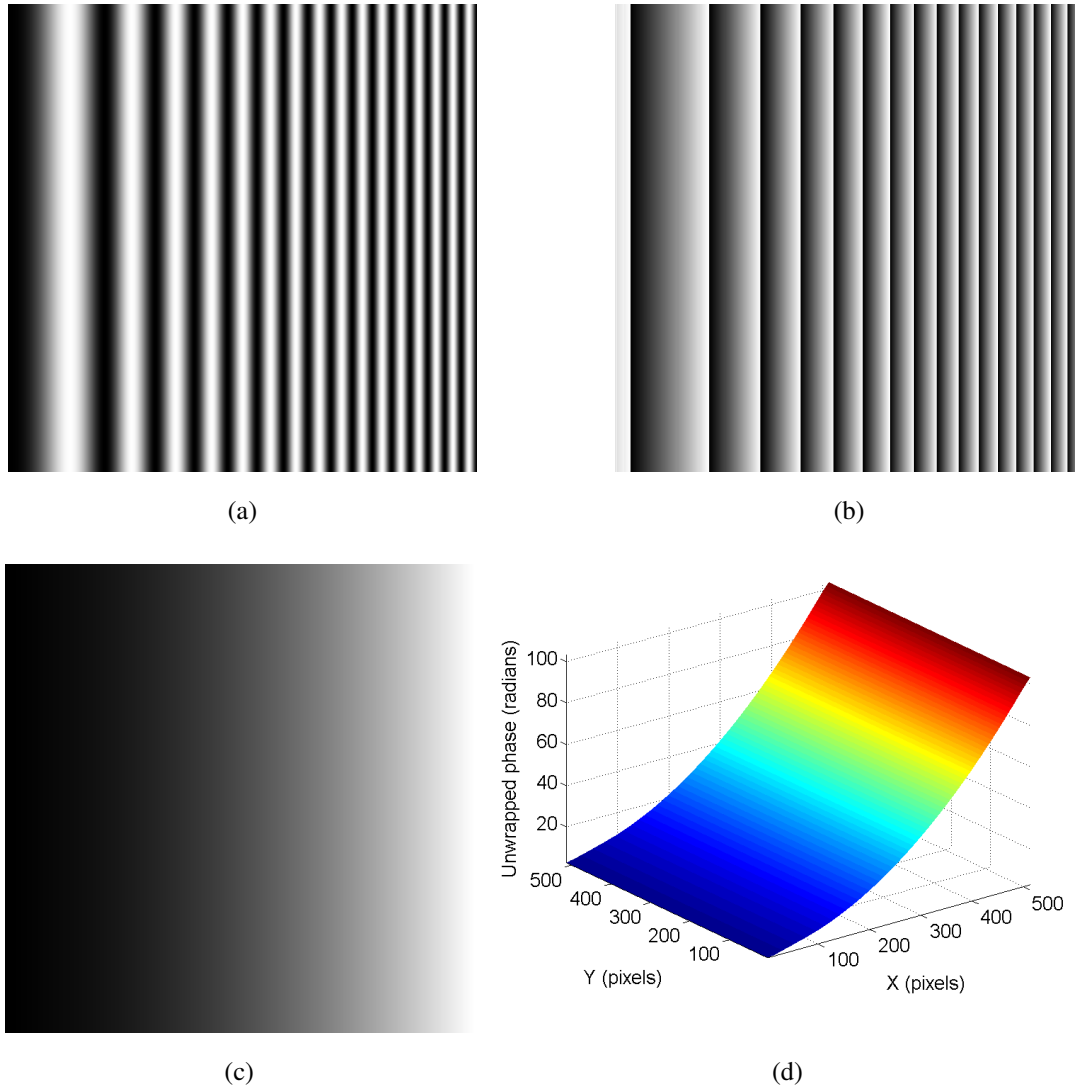


Figure 4.1: The DRD algorithm applied in fringe patterns with monotonic phase distribution: (a) Simulated fringe patterns, (b) extracted wrapped phase distribution, (c) unwrapped phase distribution with gray scale illustration, and (d) unwrapped phase distribution with 3D illustration.

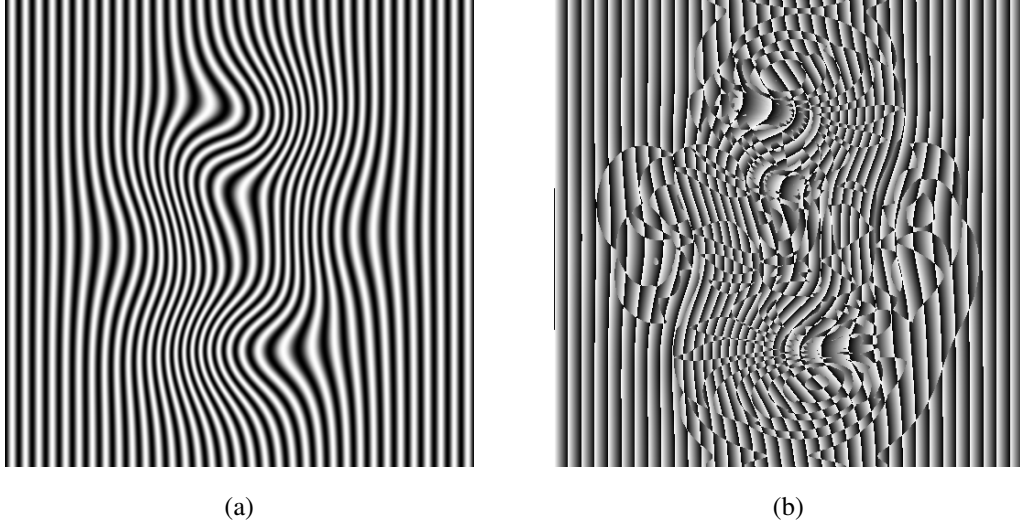


Figure 4.2: Phase ambiguity in a simulated interferogram with non-monotonic phase distribution: (a) Simulated fringe patterns with four peaks, and (b) extracted phase distribution with $\theta \in [-\pi, \pi]$.

It can be seen from Eqs. (4.22) and (4.26) that points (\mathbf{u}, S, Θ) and $(\mathbf{u}, S, \pi + \Theta)$ yield identical coefficient modulus, and the phase values extracted by using the arctangent function in Eq. (4.18) are opposite in the two cases. Considering that phase values are usually chosen to be positive, either $\phi(\mathbf{u})$ or $2\pi - \phi(\mathbf{u})$ will be obtained with the DRD scheme.

When dealing with an interferogram in which the fringe orders change monotonically along certain directions, such as interferograms with spatial carriers like Fig. 4.2 (a), the possible rotation angle θ can be bounded to a range of π to ensure a correct analysis. Then, the correct phase distribution can be obtained and shown in Fig. 4.4.

When rotation angle $\theta \in [-\frac{\pi}{2}, \frac{\pi}{2}]$ instead of $\theta \in [-\pi, \pi]$ is employed to analyze a closed interferogram such as the one shown in Fig. 4.5 (a), the phase ambiguity can be removed in many locations, as shown in Fig. 4.5 (b). However, because the interferogram

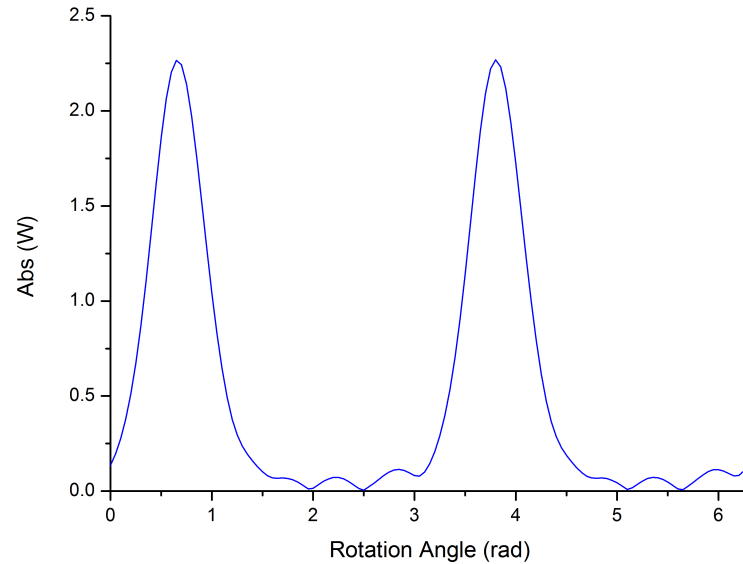


Figure 4.3: Wavelet coefficients demonstration.

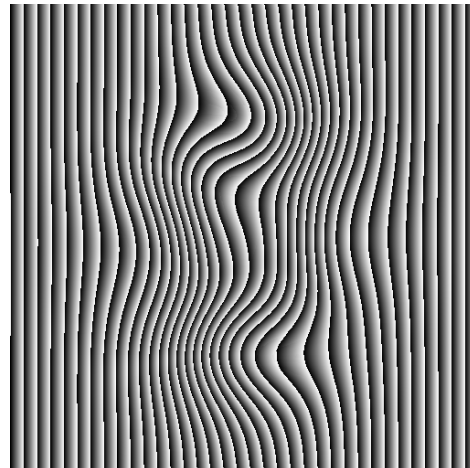


Figure 4.4: Phase ambiguity removed with $\theta \in [-\frac{\pi}{2}, \frac{\pi}{2}]$.

naturally requires a rotation angle $\theta \in [0, 2\pi)$ or $[-\pi, \pi]$, the phase ambiguity issue cannot be completely solved.

Because $|\mathcal{W}(\mathbf{u})|$ is periodical, the phase ambiguity issue can be further explained in

Fig. 4.6. If $-\frac{1}{4}\pi$ or $\frac{7}{4}\pi$ is the theoretical argument of maximum for ridges, $\frac{3}{4}\pi$ might be determined as the correct angle under the determination by using the DRD algorithm.

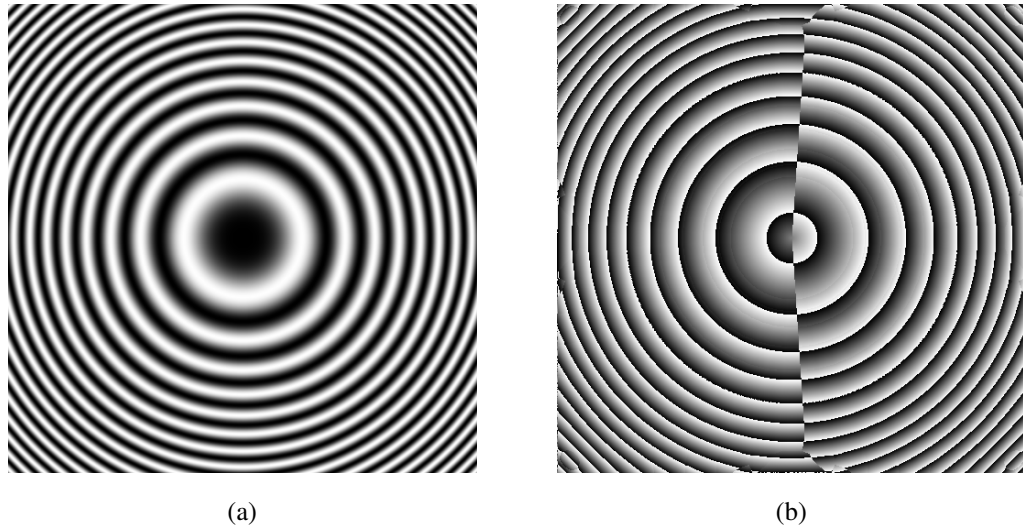


Figure 4.5: phase distribution by using the DRD algorithm with $\theta \in [-\pi/2, \pi/2]$: (a) Simulated closed fringe patterns, and (b) phase ambiguity.

4.3 Phase Determination Rule

4.3.1 Algorithm

To cope with the phase ambiguity issue introduced in the previous section, a phase determination rule is demanded for 2D-CWT to extract phase information from non-monotonic interferograms. The rule is established on the continuity of fringes, which requires the difference of rotation angles between two adjacent pixels to be small. This can be expressed as [39]

$$|\theta_{\text{ridge}}(\mathbf{u}_k) - \theta_{\text{ridge}}(\mathbf{u}_{k-1})| \leq \Delta\theta_{th} \quad (4.27)$$

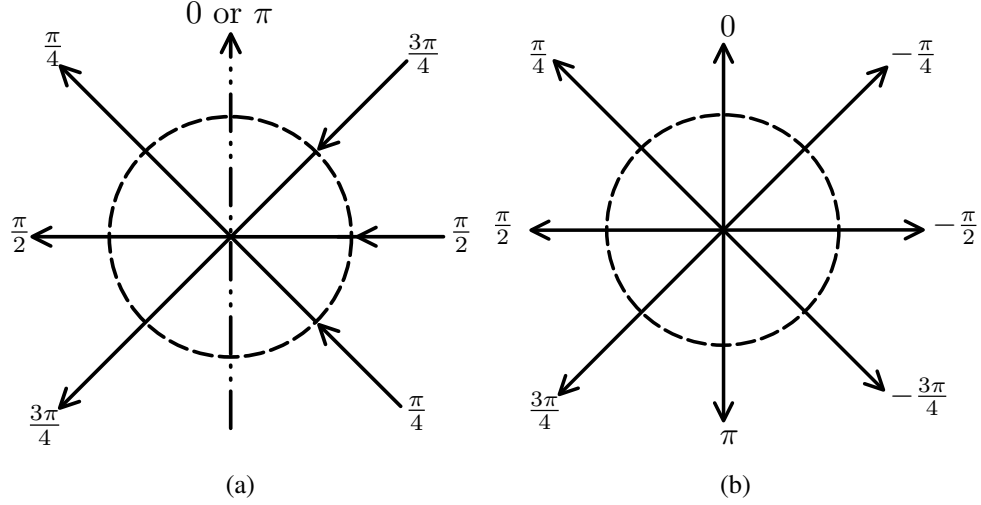


Figure 4.6: Explanation for the phase ambiguity of Fig. 4.5: (a) Wrong phase map, and (b) correct phase map.

where \mathbf{u}_k and \mathbf{u}_{k-1} represent two adjacent pixels, and $\Delta\theta_{th}$ is a threshold value.

Phase determination rule (PDR) Suppose $\theta_{dt} \in [0, \pi)$ is the rotation angle argument of the detected maximum ridge at a pixel, and $\phi_{dt} \in [0, 2\pi)$ is the corresponding phase. If θ_{dt} is continuous between this pixel and its adjacent pixel that has been well analyzed, then θ_{dt} and ϕ_{dt} are adopted as the rotation angle and phase respectively for this pixel. Otherwise, $(\theta_{dt} + \pi)$ and $(2\pi - \phi_{dt})$ should be adopted.

In practice, the PDR is achieved by the following algorithm,

$$[\theta_{\text{ridge}}(\mathbf{u}_k), \phi_{\text{ridge}}(\mathbf{u}_k)] = \begin{cases} [\theta_{dt}(\mathbf{u}_k), \phi_{dt}(\mathbf{u}_k)], & \text{if } |\theta_{\text{diff}}(\mathbf{u}_k) - \pi| > \theta_{\text{diff}}(\mathbf{u}_k) \\ [\theta_{dt}(\mathbf{u}_k), \phi_{dt}(\mathbf{u}_k)], & \text{if } |\theta_{\text{diff}}(\mathbf{u}_k) - \pi| > |\theta_{\text{diff}}(\mathbf{u}_k) - 2\pi| \\ [\theta_{dt}(\mathbf{u}_k) + \pi, 2\pi - \phi_{dt}(\mathbf{u}_k)], & \text{else} \end{cases} \quad (4.28)$$

where

$$\theta_{\text{diff}}(\mathbf{u}_k) = |\theta_{dt}(\mathbf{u}_k) - \theta_{\text{ridge}}(\mathbf{u}_{k-1})| \quad (4.29)$$

In order to interpret the PDR algorithm, figures 4.7 and 4.8 illustrate an example obtained by the 2D-CWT technique with the DRD and PDR, respectively.

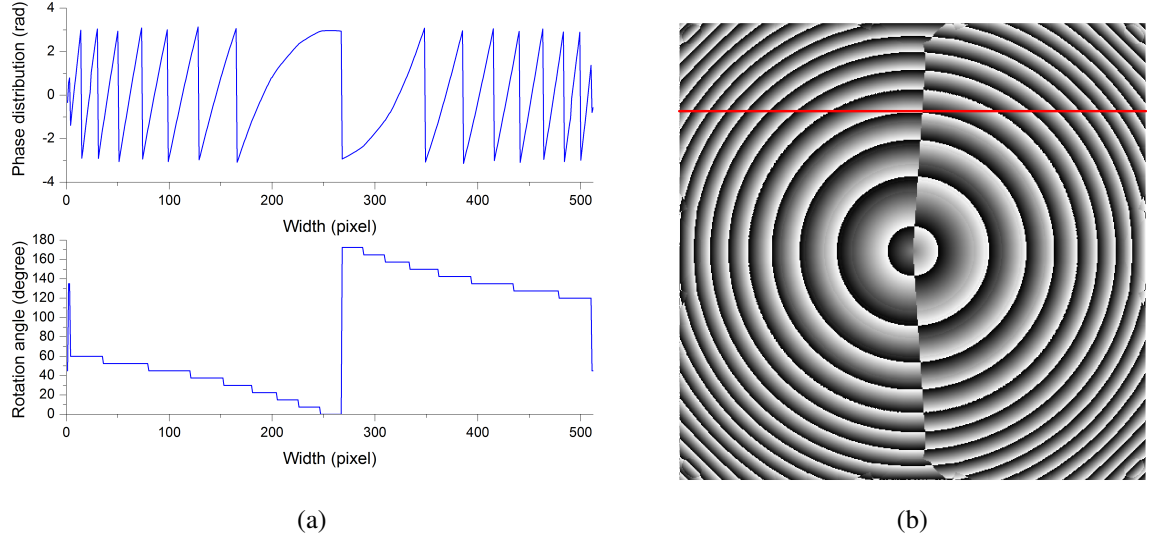


Figure 4.7: Phase distribution and rotation angles in the analysis of Fig.4.5: (a) $\phi(x)$ and θ along a line, and (b) extracted phase distribution.

4.3.2 Simulation

The algorithm of the PDR can be further explained as follows. Firstly, a conventional 2D-CWT processing with rotation angle $\theta \in [0, \pi]$ is carried out first. Then, an arbitrary starting pixel, where the fringe density is relatively high (i.e. the scale factor s is relatively small) compared with most of the fringes in the interferogram, is manually selected and marked as analyzed. After that, the pixel to be analyzed with the PDR is the one which has an adjacent neighboring pixel that has been analyzed and has the minimum scale factor s . The analysis uses 4-adjacency connectivity; if there is more than one pixel for the next candidate, all of them will be analyzed in no particular order. With this approach, the application of the PDR

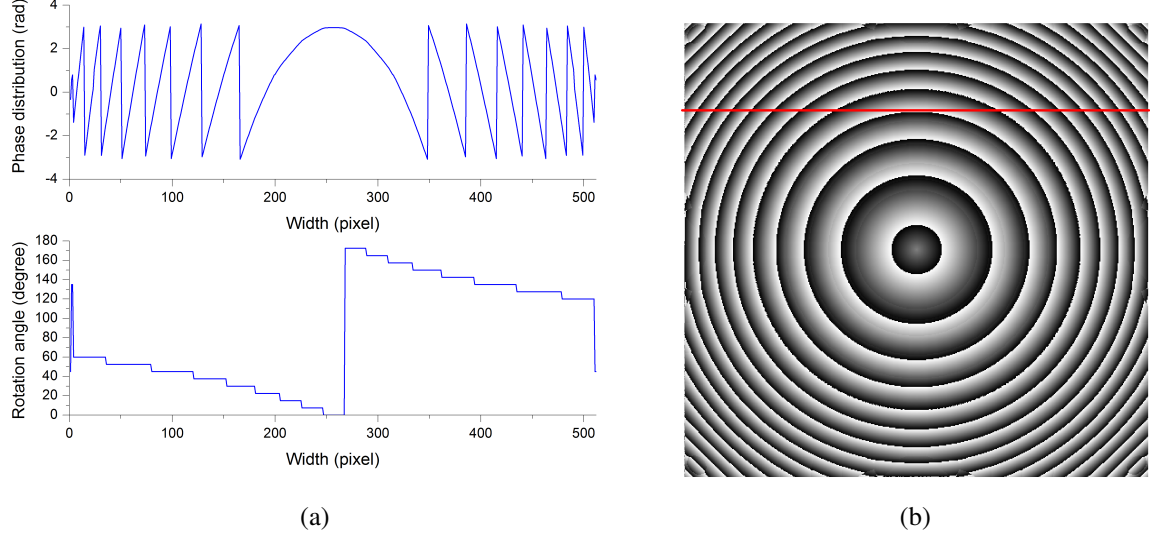


Figure 4.8: Phase distribution and rotation angles by applying the PDR: (a) $\phi(x)$ and θ along a line, and (b) correct phase distribution.

to the conventional 2D-CWT analysis results follows a path with the minimum scale factors. This procedure is similar to the reliability-guided phase unwrapping method and frequency-guided WFR method [34], and it can ensure a correct whole-field phase determination.

To demonstrate the validity of the PDR, a more complex interferogram is simulated and analyzed by using the DRD algorithm and the PDR. Figure 4.9 (b) shows the extracted phase distribution from Fig. 4.9 (a) with the phase ambiguity, and Fig. 4.9 (c) is the correct phase distribution by using the PDR. Then the unwrapped phase map can be obtained in Fig. 4.9 (d). It is noteworthy that although the frequency-guided searching approach can be directly used to obtain unwrapped phase, it is better to obtain wrapped phase first to ensure a correct analysis, as can be seen in the experiments presented below.

According to the PDR, automatic interferogram analysis should be limited to each continuous region. Consequently, for interferograms involving edge or boundary issues, a spe-

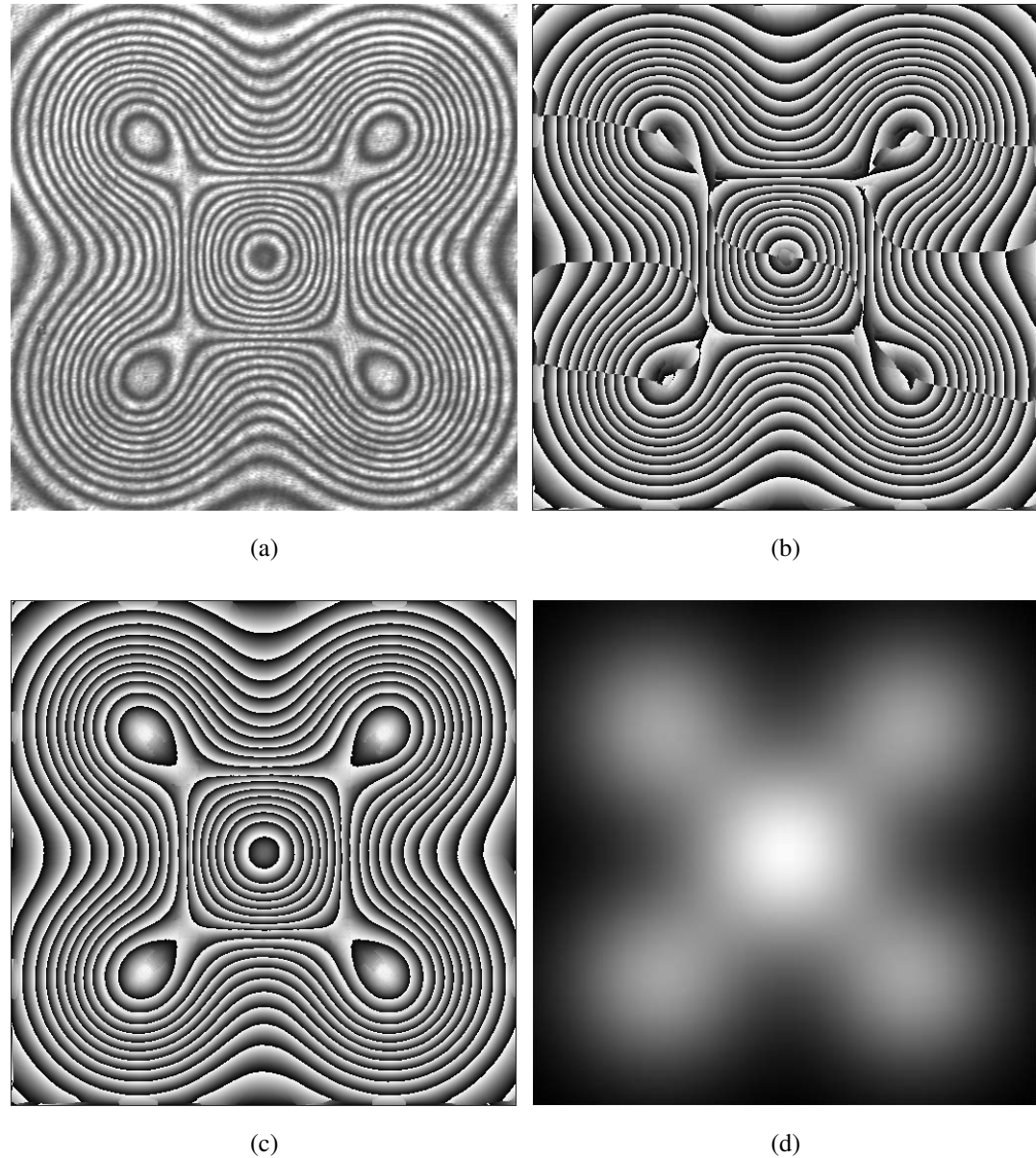


Figure 4.9: The 2D-CWT analysis of an interferogram with a complex phase distribution:
(a) Original interferogram, (b) extracted phase distribution by using $\theta \in [0, \pi)$ in the DRD
algorithm, (c) extracted phase with the PDR, and (d) unwrapped phase map.

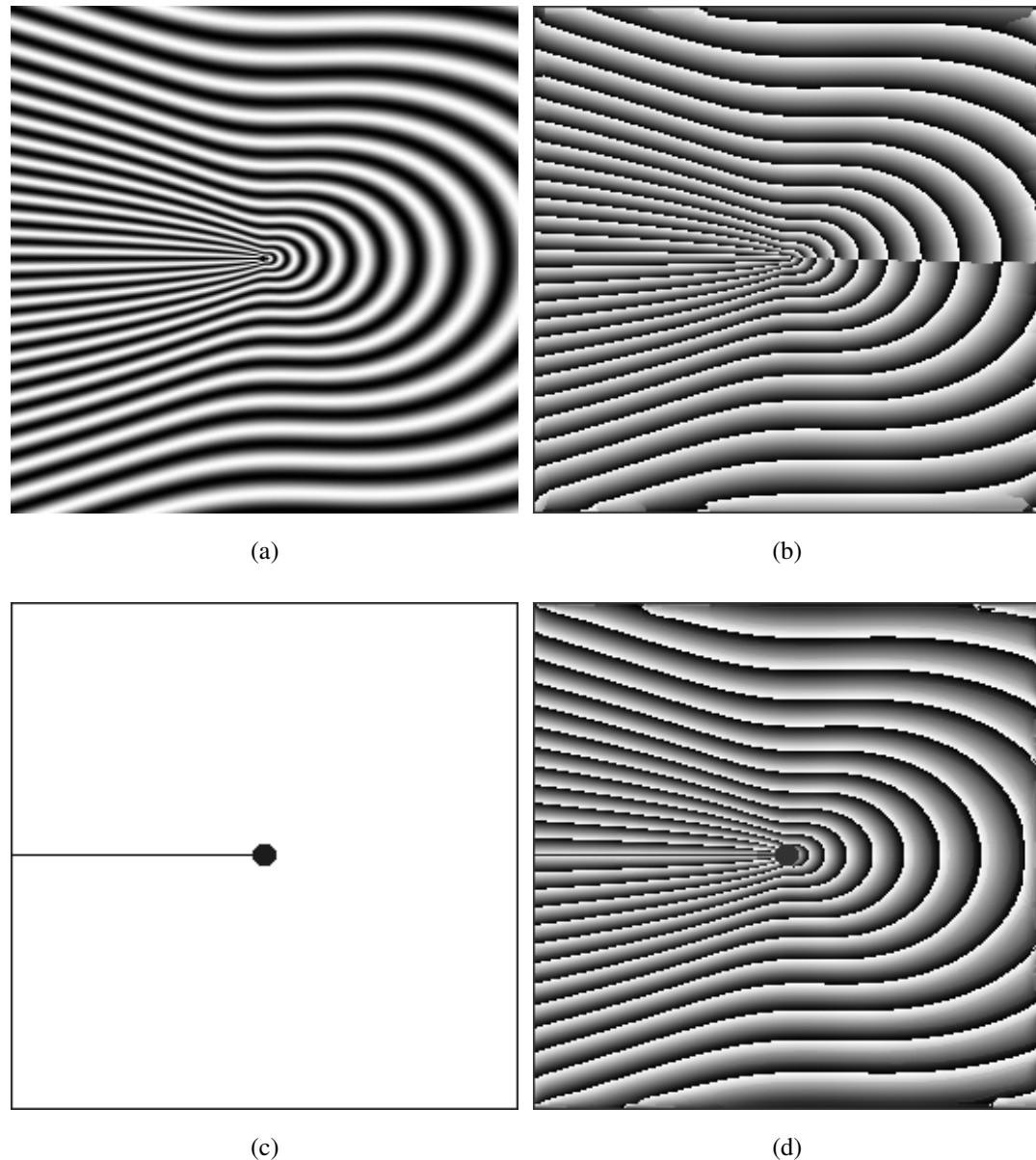


Figure 4.10: Phase distribution extracted from an interferogram containing a crack: (a) Interferogram in a crack region, (b) detected incorrect phase distribution, (c) boundary mask, and (d) detected correct phase distribution.

cial handling of applying a boundary mask is normally required to assure a correct phase determination. For instance, figure 4.10 (a) shows a simulation interferogram representing the deformation field around a crack. The proposed technique fails to yield a correct phase map without using a boundary mask, as shown in Fig. 4.10 (b). After specifying a boundary mask (Fig. 4.10 (c)) to make the frequency-guided searching occur within the valid region and prevent the analysis from crossing the discontinuity boundaries, a correct phase map (Fig. 4.10 (d)) is obtained. It may be worth mentioning that, in our perspective, the rule that automated interferogram analysis should not cross discontinuity (material discontinuity and geometric discontinuity) boundaries is valid for most interferogram analysis techniques we know, including phase shifting, Fourier transform, wavelet transform, and fringe skeletonizing techniques. Before analyzing the interferograms, such as the one shown in Fig. 4.10 (a), the discontinuity boundaries need to be known in advance.

4.4 Cover Map

Unlike the spatial-time domain techniques, e.g., the PS technique, the 2D-CWT technique is robust to noise and requires only a single image for fringe pattern analysis. However, 2D-CWT analysis is generally time consuming due to the convolution involved process, which hampers the applications of the technique. To cope with this problem, the FFT has been adopted to implement the 2D-CWT technique for fringe pattern analysis [35]. But the computation time of 2D-CWT analysis is still much longer than that of other popular techniques, such as the PS technique.

To further increase the analysis speed, a feasible solution is to choose a small number of discrete parameters instead of continuous dilation and rotation parameters. Some discussions on the choice of the dilation parameters in the 1D-CWT have been presented [37], but a

complete and rigorous explanation remains lacking, especially for the 2D-CWT case, where the rotation parameters should be taken into consideration. By observing the essence of wavelet transform, a concept called the cover map is introduced in this section to discretize the dilation and rotation parameters in the 2D-CWT analysis [43].

4.4.1 Heisenberg Uncertainty Principle

In time-frequency analysis, the Heisenberg uncertainty principle gives the relation between the temporal resolution and frequency resolution. The principle states that the time-frequency analysis window cannot be arbitrary small and the minimal temporal and frequency resolution cannot be achieved at the same time [83, 105], which can be expressed in radians or in hertz as

$$\Delta_f \Delta_{\hat{f}} \geq \frac{1}{2} \quad \text{or} \quad \Delta_f \Delta_{\hat{f}} \geq \frac{1}{4\pi} \quad (4.30)$$

where Δ_f is the half-duration of signal $f(t)$ in the time domain and $\Delta_{\hat{f}}$ is the frequency half-bandwidth of $f(t)$, whose Fourier transform is $\hat{f}(\omega)$. $2\Delta_f \times 2\Delta_{\hat{f}}$ or $4\Delta_f \Delta_{\hat{f}}$ is known as the “Heisenberg box” or “time-frequency analysis window” in the time-frequency plane.

In engineering, the measure of the duration of a signal is often determined by using the root mean square (RMS) duration or full width at half-time (FWHT) in terms of the energy and magnitude, respectively. Specifically, the half-RMS duration or radius of a signal is defined as

$$\Delta_f := \frac{1}{\|f\|_2} \left(\int_{-\infty}^{\infty} (t - t_0)^2 |f(t)|^2 dt \right)^{1/2} \quad (4.31)$$

where t_0 is the center or mean time of the signal and is written as

$$t_0 := \frac{1}{\|f\|_2^2} \int_{-\infty}^{\infty} t |f(t)|^2 dt \quad (4.32)$$

The equality of Eq. (4.30), that is,

$$\Delta_f \Delta_{\hat{f}} = \frac{1}{2} \quad \text{or} \quad \Delta_f \Delta_{\hat{f}} = \frac{1}{4\pi} \quad (4.33)$$

holds if and only if the signal has the following form:

$$f(t) = c \exp(ikt) \exp\left[-\frac{(x - \mu)^2}{2\sigma^2}\right] \quad (4.34)$$

where c is a nonzero constant; $k, \mu, \sigma \in \mathbb{R}$; and $\sigma \neq 0$. The equality indicates that the smallest Heisenberg box or minimal time-frequency resolution can be achieved by using a Gaussian function, such as the normal distribution,

$$g(t) = \frac{1}{\sqrt{2\pi}\sigma} \exp\left[-\frac{(t - \mu)^2}{2\sigma^2}\right] \quad (4.35)$$

where μ is the mean (or the center of the distribution) and σ is the standard deviation. By using Eq. (4.32), the center of the Gaussian signal in the time domain can be obtained as

$$t_0 = \frac{1}{\|g\|_2^2} \int_{-\infty}^{\infty} t |g(t)|^2 dt = \mu \quad (4.36)$$

and the radius through Eq. (4.31) can be obtained as

$$\Delta_g = \frac{1}{\|g\|_2} \left(\int_{-\infty}^{\infty} (t - t_0)^2 |g(t)|^2 dt \right)^{1/2} = \frac{\sqrt{2}}{2} \sigma \quad (4.37)$$

The radius of the bandwidth in the frequency domain can be calculated by using Eq. (4.33) as

$$\Delta_{\hat{g}} = \frac{\sqrt{2}}{2\sigma} \quad (4.38)$$

4.4.2 Wavelet modulated window

In the 2D case, the wavelet function $\psi(x)$, also known as “mother wavelet” or “wavelet kernel”. In the 2D-CWT fringe pattern analysis, the most widely used 2D wavelet function,

named the 2D Morlet wavelet, is given by

$$\psi_M(\mathbf{x}) = \exp(i\omega_0 \cdot \mathbf{x}) \exp\left(-\frac{1}{2\sigma^2}|\mathbf{x}|^2\right) \quad (4.39)$$

It is a general form compared with Eq. (4.20) and the Fourier transform of the 2D Morlet wavelet is

$$\hat{\psi}_M(\omega) = \exp\left(-\frac{\sigma^2}{2}|\omega - \omega_0|^2\right) \quad (4.40)$$

Without loss of generality, in this section, the 2D Morlet wavelet is used as the mother wavelet. It should be pointed out that the following concepts can be easily modified and applied to other wavelets as well.

Generally, $\hat{\psi}_M(\omega)$ is known as the wavelet modulated window in the frequency domain. It can be seen from Eq. (4.40) that the Morlet wavelet is actually a kind of bandpass filter, and the center frequency is modulated to ω_0 . According to Eq. (4.31), by means of the RMS width, which is defined in the time domain as $2\Delta_\psi$ and in the frequency domain as $2\Delta_{\hat{\psi}}$, the time-frequency analysis window can be written as

$$[|\mathbf{u}_0| - s\Delta_\psi, |\mathbf{u}_0| + s\Delta_\psi] \times [\frac{|\omega_0|}{s} - \frac{1}{s}\Delta_{\hat{\psi}}, \frac{|\omega_0|}{s} + \frac{1}{s}\Delta_{\hat{\psi}}] \quad (4.41)$$

Moreover, based on the Heisenberg Uncertainty Principle and Eq. (4.33), the Morlet analysis windows satisfy the following equation

$$\Delta_\psi \Delta_{\hat{\psi}} = \frac{1}{2} \quad (4.42)$$

Specifically according to Eq. (4.37) and (4.38), for the standard deviation $\sigma = \frac{1}{2}$,

$$\Delta_\psi = \frac{\sqrt{2}}{2}\sigma = \frac{\sqrt{2}}{4} \quad \text{and} \quad \Delta_{\hat{\psi}} = \sqrt{2} \quad (4.43)$$

Another commonly used deviation $\sigma = 1$ in fringe pattern analysis gives

$$\Delta_\psi = \frac{\sqrt{2}}{2} \quad \text{and} \quad \Delta_{\hat{\psi}} = \frac{\sqrt{2}}{2} \quad (4.44)$$

Equations (4.43) and (4.44) show that the 2D Morlet wavelet has finer resolution in the time domain than in the frequency domain with the standard deviation $\sigma = 1/2$ and the same resolution both in the time domain and the frequency domain with $\sigma = 1$.

4.4.3 Cover Map

In the spatial-frequency domain, according to the Heisenberg uncertainty principle and the time-frequency analysis window described by Eq. (4.41), the 2D-CWT algorithm introduces a series of analysis windows in terms of the effective support of wavelets, which are called *cover patterns* here. All of the cover patterns form a *cover map* for fringe pattern analysis, similar to the image in Fig. 4.11.

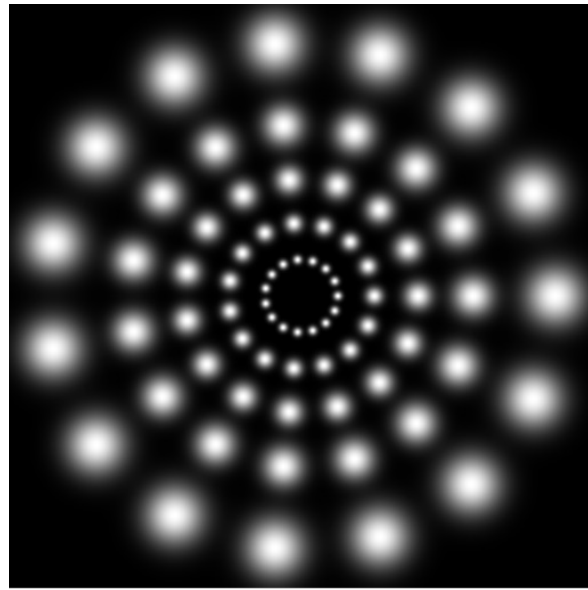


Figure 4.11: Wavelet modulated window in the frequency domain.

In the existing 2D-CWT fringe pattern analysis with the DRD algorithm, it is desired that the scale factors s cover all the possible fringe periods. This requires a small increment of s , such as 1 pixel, for an accurate analysis. For the rotation angle θ , a similar requirement is

demanded. This indicates that the 2D-CWT dilation and rotation parameters, s and θ , should be digitally continuous. It is for this reason that the 2D-CWT requires longer computation time than many other fringe analysis techniques.

To substantially reduce the number of dilation parameters, the redundant scale factors can be removed from the continuous parameters and only a minimum number of scale factors are needed to cover the frequency plane. Without loss of generality and for simplicity, the rotation angle is fixed as $\theta = 0$ in the following elaboration.

In order to cover the whole x axis in the frequency plane, based on Eq. (4.41), the ratio of any two adjacent scale factors s_k and s_{k+1} should satisfy the following equation:

$$\frac{\Delta_{\hat{\psi}}}{s_{k+1}} + \frac{\Delta_{\hat{\psi}}}{s_k} = \frac{|\omega_0|}{s_k} - \frac{|\omega_0|}{s_{k+1}} \quad (4.45)$$

This yields

$$q = \frac{s_{k+1}}{s_k} = \frac{|\omega_0| + \Delta_{\hat{\psi}}}{|\omega_0| - \Delta_{\hat{\psi}}} \quad (4.46)$$

Theoretically, the admissibility condition of the 2D Morlet wavelet requires $|\omega_0| \geq 5.3364$ [95]. In practice, $\omega_0 = (2\pi, 0)$ is an educated choice and has been widely used. The reason is that 2π not only ensures the satisfaction of the admissibility condition, but also is related to the period of fringe patterns. This can be seen from Eq. (4.41), where the center frequency is

$$\omega_c = \frac{\omega_0}{s} \quad (4.47)$$

With $|\omega_0| = 2\pi$, the value of s will represent the period of the local fringe pattern which has an ideal match with the daughter wavelet. In this case, considering $\Delta_{\hat{\psi}} = \sqrt{2}/(2\sigma)$ from Eq. (4.38), equation (4.46) becomes

$$q = \frac{s_{k+1}}{s_k} = \frac{2\pi + \frac{\sqrt{2}}{2\sigma}}{2\pi - \frac{\sqrt{2}}{2\sigma}} \quad (4.48)$$

Therefore, instead of using a large number of scale factors, the 2D-CWT analysis can simply use a small number of scale factors as the dilation parameters. Suppose that the fringe periods vary from λ_l to λ_h , where λ_l and λ_h are estimated values with λ_l no greater than the actual minimum period and λ_h no less than the actual maximum period, the ideal smallest scale factor can be determined as $s_l = \lambda_l [1 + \Delta_{\hat{\psi}}/(2\pi)]$. This ensures that the low end of the cover pattern is exactly λ_l because s_l is the center of the cover window and its half-width is $\lambda_l \Delta_{\hat{\psi}}/(2\pi)$ based on Eq. (4.41). Similarly, the ideal largest scale factor is $s_h = \lambda_h [1 - \Delta_{\hat{\psi}}/(2\pi)]$ to make the high end of the cover pattern be exactly λ_h . The actual selection of scale factors can begin from either s_l or s_h , so the dilation parameters can be chosen as $s = \{s_l, qs_l, q^2 s_l, \dots\}$, and an alternative way is using $s = \{\dots, q^{-2} s_h, q^{-1} s_h, s_h\}$. In practice, $\sigma = 0.5$ and 1.0 are commonly used in the 2D-CWT for fringe pattern analysis, and the corresponding q can be calculated as 1.5809 and 1.2536 , respectively. Another notable value is $\sigma = 0.3376$ obtained from a special $q = 2.0$, which yields dyadic scale factors $s = \{2, 4, 8, 16, 32, 64, 128, \dots\}$. Figures 4.12 (a)-4.12(c) show the complete cover maps for these three cases. For comparison, a representative cover map obtained from $\sigma = 0.5$ and $q = 2.0$ (i.e. dyadic scale factors) is shown in Fig. 4.12 (d). The last cover map is incomplete because the complete one requires $q = 1.5809$ instead of $q = 2.0$. In the figures, the image size is assumed to be 512×512 pixels, and the x axis has been converted to hertz for better illustration purpose.

The rotation angle θ can be determined according to the geometric relation illustrated in Fig. 4.13 as

$$\Delta\theta = 2c \arcsin \left(\frac{\Delta_{\hat{\psi}}/s}{|\omega_0|/s} \right) = 2c \arcsin \left(\frac{\Delta_{\hat{\psi}}}{|\omega_0|} \right) \quad (4.49)$$

where c is a nonzero constant to control the overlap between two adjacent cover patterns. When $c = 1$, the increments of θ can be determined as $\Delta\theta = 0.6797, 0.4540$, and 0.2256 for

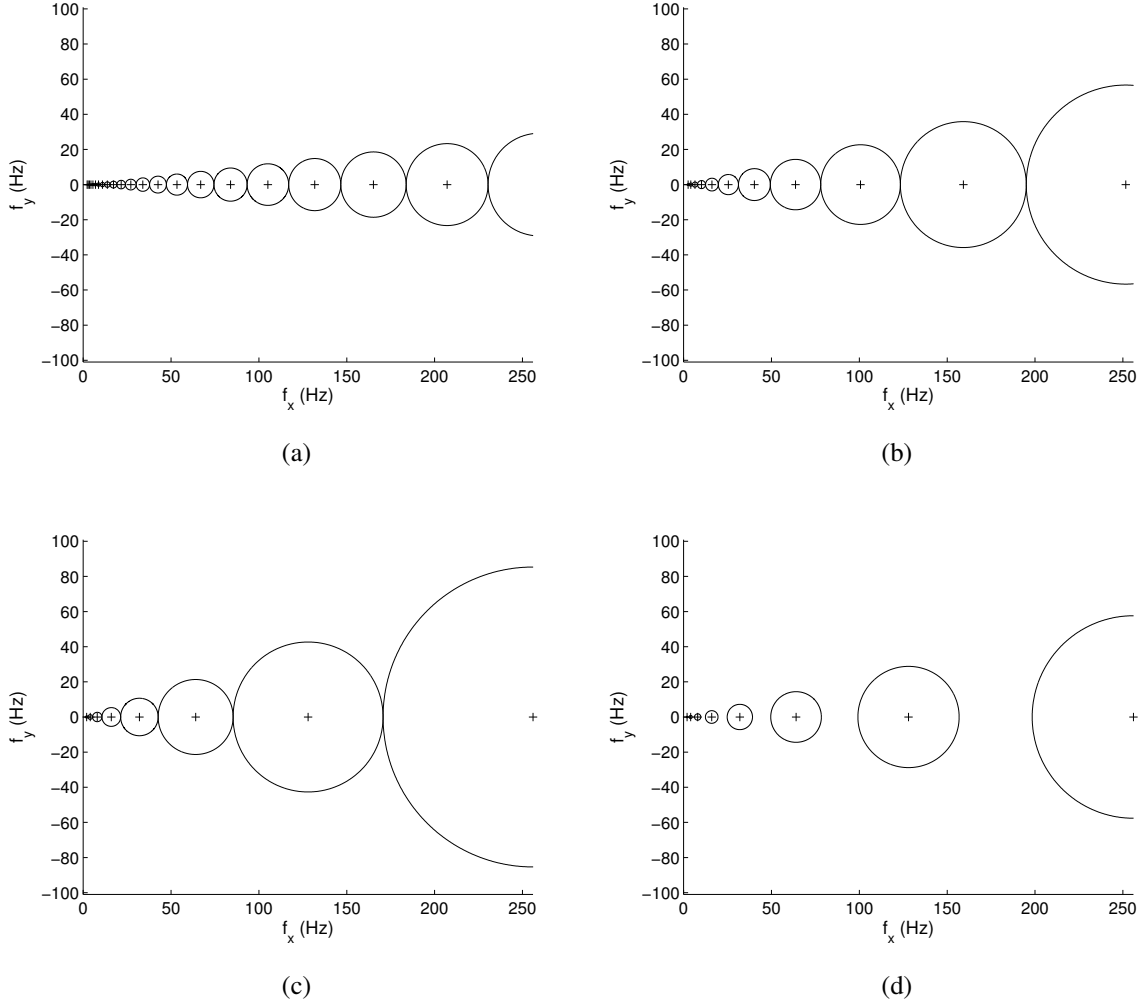


Figure 4.12: Examples of cover maps: (a) $\sigma = 1.0$ and $q = 1.2536$, (b) $\sigma = 0.5$ and $q = 1.5809$, (c) $\sigma = 0.3376$ and $q = 2.0$, and (d) $\sigma = 0.5$ and $q = 2.0$.

$\sigma = 0.3376$, 0.5 , and 1.0 , respectively.

From the presented theory and concept, for a given σ , by using appropriate scale factors and rotation angles, the 2D-CWT analysis is able to produce a complete cover map in the spatial frequency plane. For instance, figure 4.14 shows an example where the scale factor $s = \{2, 4, 8, 16, 32, 64, 128, 256\}$ and the rotation angle $\theta = \{-1.3593, -0.6797, 0.0, 0.6797, 1.3593\}$

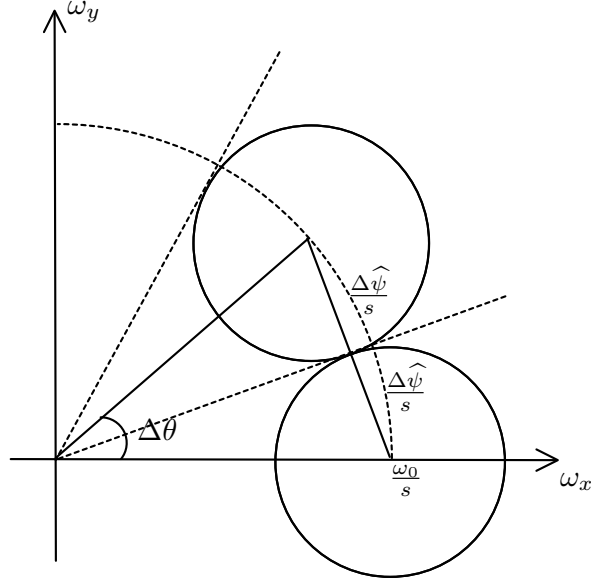


Figure 4.13: Schematic of the calculation of rotation angle.

for $\sigma = 0.3376$. Because the negative frequency plane does not need to be considered, only half of the cover map is plotted. Compared with the conventional analysis that uses digitally continuous parameters and exhaustive searching, the scheme based on the above discretized parameters has the ability to dramatically speed up the 2D-CWT analysis.

In real applications, the selection of σ depends on the actual fringe patterns because varying σ changes the resolution of the time-frequency analysis window. According to the uncertainty principle, decreasing the size of the frequency analysis window will enlarge the time analysis window, and vice versa. Numerous experimental results show that the proper σ is in the range of $0.45 \sim 0.65$. Furthermore, $\sigma = 0.5$ gives the best results in most cases and is, therefore, recommended for general fringe patterns. For fringe patterns with local defects where fringes are lacking or damaged, a larger σ can be used to recover the fringes there.

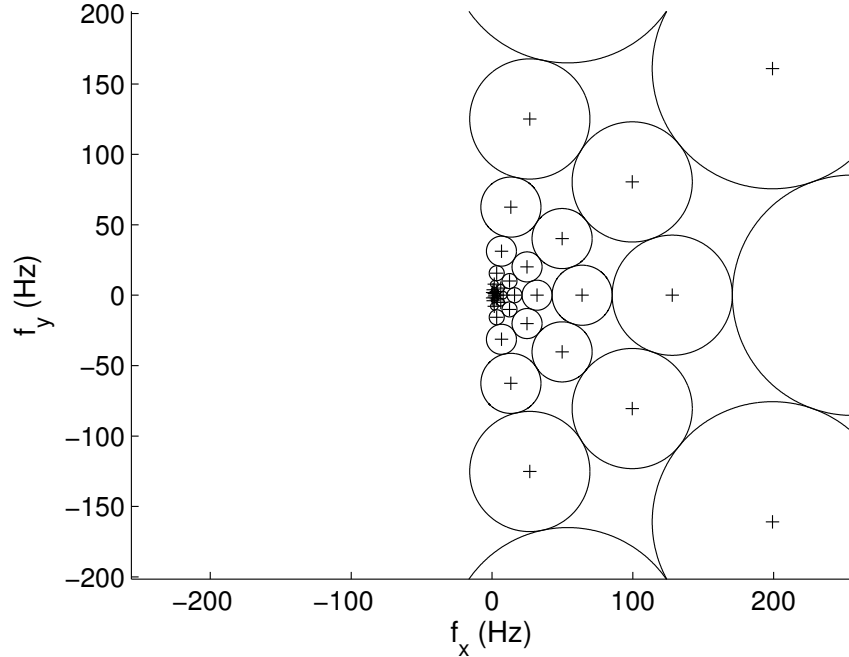


Figure 4.14: Complete dyadic cover map for $\sigma = 0.3376$.

4.4.4 Simulation

As mentioned before, the cover map actually comes from the concept of filters. In order to verify the proposed concept, a monotonic fringe patterns with the chirp is utilized to examine all the bandwidths of frequency analysis windows. Specifically, a fringe pattern of 512×512 pixels involving a sweep signal generated by computer is expressed as Eq. (2.21) in Sec. 2.4.1. The initial frequency $f_0 = 2$ Hz, and the dynamic range of frequency varies from 2 to 256 Hz in order to simulate all the possible frequencies of the fringe patterns. $N(\mathbf{x})$ is the random Gaussian noise and its amplitude is comparable with the amplitude of fringes patterns, e.g., $|N(\mathbf{x})| \geq 0.5|I_a(\mathbf{x})|$. In the simulation, $\sigma = 0.5$ and $\omega_0 = (2\pi, 0)$ are used, and the scale factors are $s = \{2.0344, 3.2162, 5.0844, 8.0380, 12.7074, 20.0892, 31.7593, 50.2085, 79.3750, 125.4847, 198.3798\}$ with $q = 1.5809$.

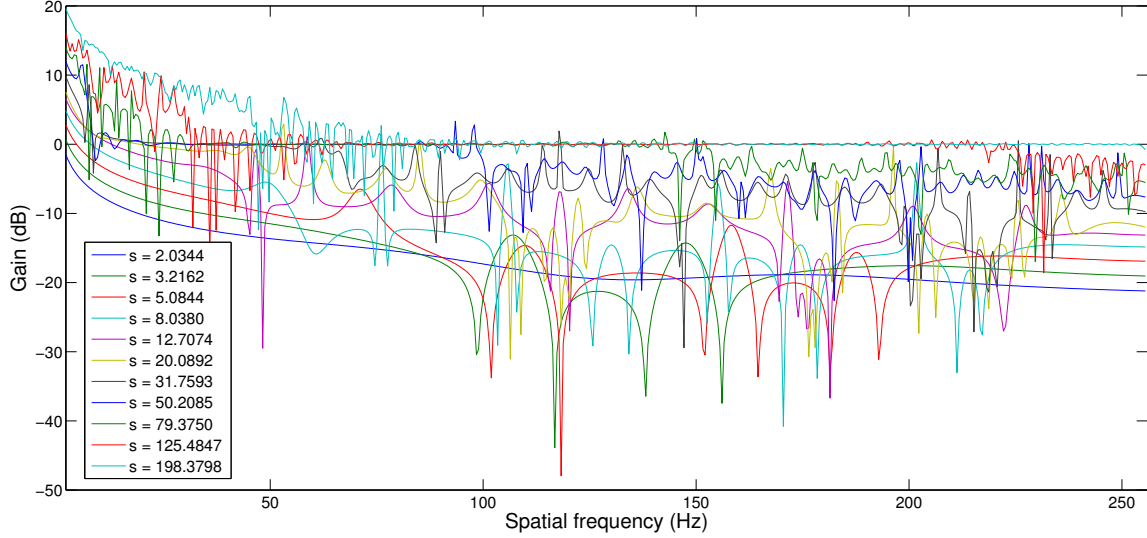


Figure 4.15: Frequency response.

By using the 2D-CWT analysis with discrete parameters associated with the complete cover map, the frequency response can be obtained, as Fig. 4.15 shows. For clear illustration purpose, the results from four representative scale factors are individually plotted in Fig. 4.16. For example, the theoretical bandwidth of the cover pattern with $s = 8.0380$ is from 49.36 to 78.03 Hz according to Eq. (4.41), and the simulation result for the same bandwidth shows that the frequency gain amplitudes [Gain = $10 \log(f_e/f_t)$ dB, with f_e as the frequency extracted by using the 2D-CWT technique and f_t the true value] are less than 0.08 dB. The bandwidth can be clearly seen from Fig. 4.16 (b). It is noted that a perfect zero gain is essential for an ideal match between the detected frequency and the theoretical frequency. However, the ideal case cannot be achieved due to the existence of noise in practice, and the gain always fluctuates around 0 dB. Since the fluctuation amplitude is very small, its effect can be neglected. For the frequency response at low frequency cases, such as $s = 125.4847$ shown in Fig. 4.16 (d), the gain values of the corresponding bandwidth from 3.16 to 4.99

Hz are from 0.15 to -1.5 Hz. Because it is a very small bandwidth in a low frequency region, which is typically not a region of interest in practice, such gain values will not bring nonnegligible errors to the fringe analysis.

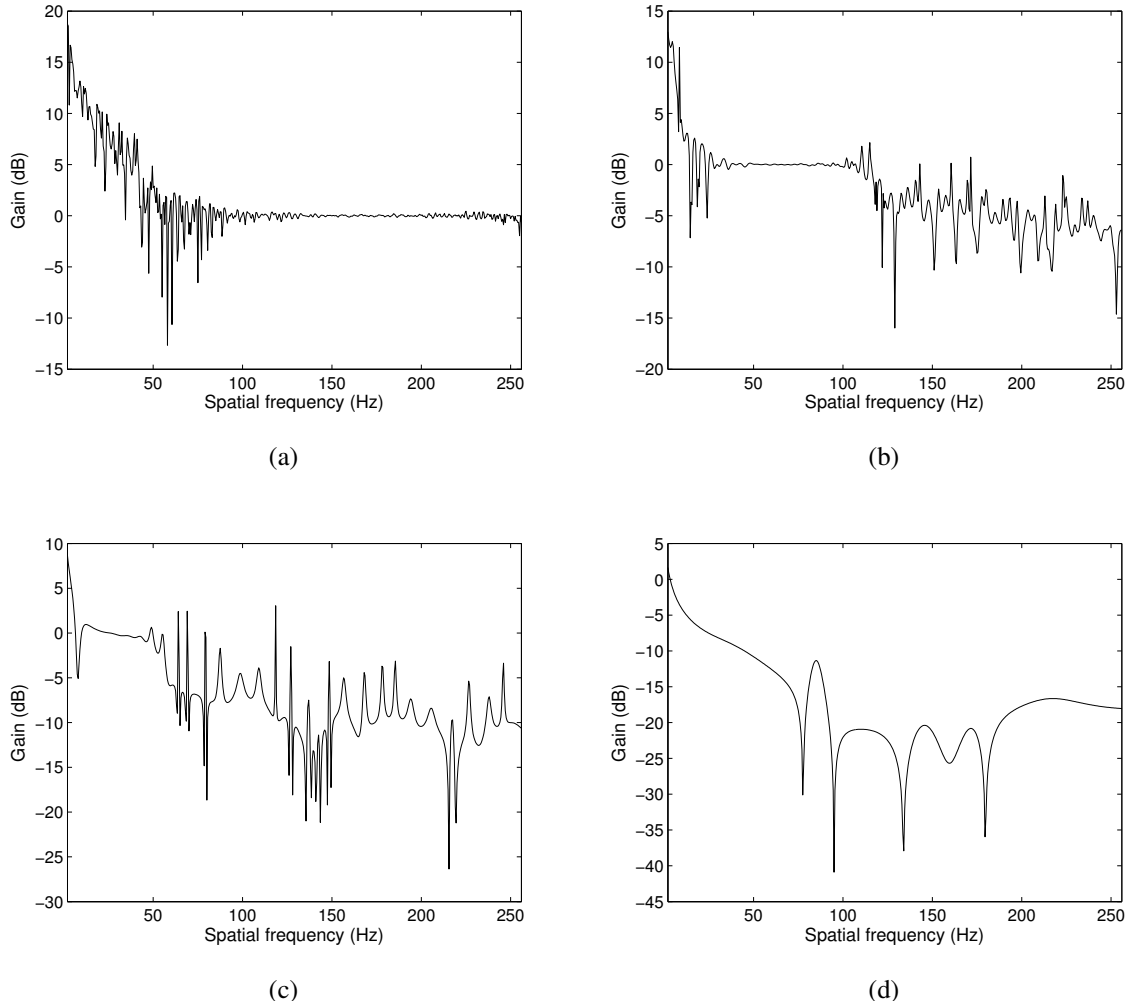


Figure 4.16: Frequency response for $\sigma = 0.5$: (a) $s = 3.2162$, (b) $s = 8.0380$, (c) $s = 20.0892$, and (d) $s = 125.4847$.

From the simulation, the frequency responses demonstrate that the resolution of the 2D-CWT analysis is related to the scale factors. Each scale factor allows the 2D-CWT analysis

to cover a certain range in the spatial frequency plane. By using appropriate discrete scale factors determined from Eq. (4.48), the 2D-CWT technique is able to detect all the spatial frequencies in the fringe pattern.

With the proposed approach, once the standard deviation σ is chosen, all the dilation and rotation parameters can be easily determined for the 2D-CWT fringe pattern analysis. To demonstrate the effect of different σ values on the analysis results, a computer-generated fringe pattern containing fringes with frequencies from 10 to 50 Hz is used in the simulation. Figures 4.17 (a) and 4.17(b) are the fringe patterns without and with noise, respectively. Four different sets of standard deviation σ and adjacent scale factor ratio q , identical to the ones used in producing Fig. 4.17 are employed to analyze the noisy fringe pattern in Fig. 4.17 (b). It can be seen from the results plotted in Figs. 4.17 (c)-4.17(f) that $\sigma = 0.5$ with a complete cover map yields the best results, while $\sigma = 0.5$ with a dyadic cover map (i.e. a complete cover map for $\sigma = 0.3376$ but incomplete for $\sigma = 0.5$) gives the worst results. It is noted that the bad results at the two ends of the image are induced by the edge effects, so they are not considered in the performance evaluation.

Varying the value of σ will change the resolution of the time-frequency analysis window. The selection of σ depends on the actual fringe patterns, and the balance of resolution in the time domain and frequency domain should be considered carefully. A general guideline is as follows: $\sigma = 0.5$ is recommended for general fringe patterns; for fringe patterns with local defects where fringes are lacking or damaged, a larger σ can be used to recover the fringes there.

Compared with the conventional 2D-CWT analysis, this technique can help remarkably increase the analysis speed. For this reason, it can be practically very useful for processing various kinds of interferograms or fringe patterns in many scientific and engineering

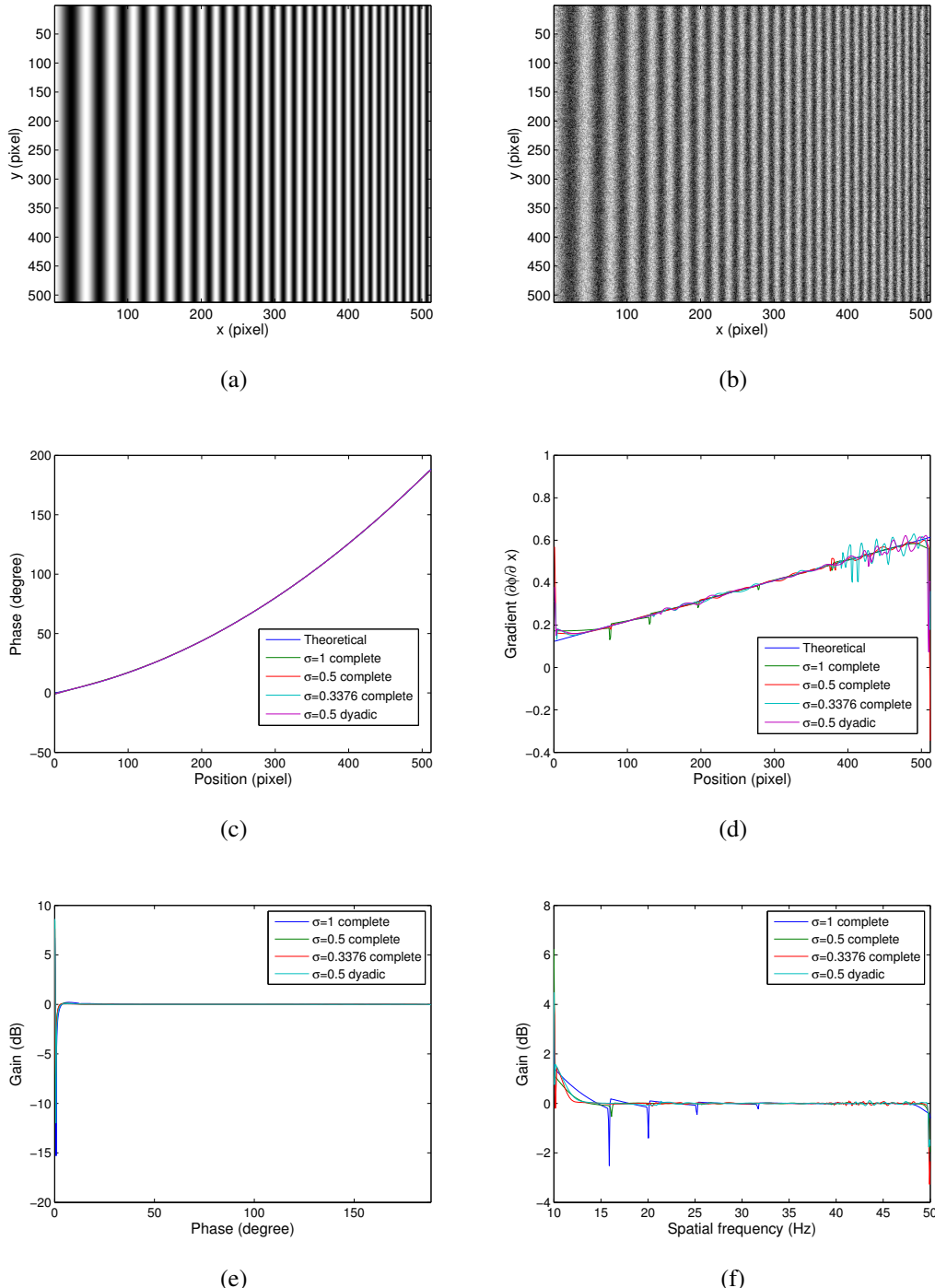


Figure 4.17: Simulation results: (a) fringe pattern, (b) fringe pattern with noise, (c) extracted phase, (d) phase gradient, (e) phase gain, and (f) frequency gain.

applications, especially those highly relying on single-image analysis, such as dynamic interferograms.

4.5 Performance

The mother wavelet is an essential component in the wavelet transform, and many kinds of mother wavelets have been employed in the 2D-CWT fringe pattern analysis. A typical one is the well-known Gabor wavelet, which was initially used for processing the moiré interferometry [17] and later was developed to analyze the speckle fringe pattern [27] as well as the digital holography [28]. Another commonly used wavelet which is known as the Morlet wavelet, and it has been successfully applied to practical optical measurements [35, 38–40]. Furthermore, a number of other notable wavelets, including the Fan wavelet [38], Paul wavelet [36], Mexican wavelet [41], Shannon wavelet and Spline wavelet [42], have also been used in fringe pattern analysis.

As the 2D-CWT fringe pattern analysis technique becomes mature for scientific research and engineering applications, a few discussions on the parameters of certain mother wavelets have been made to evaluate the performance of the 2D-CWT technique. For instance, a cost function was proposed to employ various scale factors and rotation angles in the 2D-CWT fringe pattern analysis, and a corresponding performance comparison with the 2D Fourier transform technique based on analyzing experimental fringe patterns was carried out [40]. By virtue of the cover map, the meaning of the parameters of the 2D-CWT is elaborated in Sec. 4.4. In addition, with respect to the local stationary length concept, an algorithm on the selection of the window size in the 2D-CWT technique was proposed and adapted for use by the 2D windowed Fourier transform analysis [42, 44]. A detailed comparison of the 2D-CWT and other time-frequency analysis techniques was also recently presented [45].

It is noteworthy, however, that the aforementioned discussions were usually made for certain mother wavelets and with respect to one or two aspects of the 2D-CWT technique. Moreover, the comparisons were conducted based on experiment results, and a fundamental theoretical analysis is lacking. Consequently, it remains unclear which kinds of wavelet(s) should be used in practice. In this section, the performance of a few commonly used mother wavelets is investigated and discussed based on the theory of the 2D-CWT technique, and this gives a general guidance on the selection of the mother wavelet in the 2D-CWT fringe pattern analysis [106].

By virtue of the ability to extract instantaneous frequencies in terms of the ridge of wavelet coefficients [96, 99], the DRD algorithm had been proposed to obtain the phase distributions of fringe patterns [23, 27, 37, 39] as Sec. 4.2 described. Specifically, with the DRD algorithm and based on the fact that I_b and I_a can be treated as constants in a local region of a fringe pattern, the phase distribution of the fringe pattern can be obtained from the wavelet coefficients at the ridge points by using Eq. (4.18). It can be seen from the governing equation Eq. (4.18) that the mother wavelet plays a key role in the 2D-CWT fringe pattern analysis.

4.5.1 Isotropic Wavelets

With respect to the detecting direction, wavelets can be classified as isotropic wavelets and anisotropic or directional wavelets [95]. The most commonly used isotropic wavelet is the 2D Mexican hat wavelet (2D-MHW), which is defined in the time domain as

$$\begin{aligned}\psi_{\text{MH}}(\mathbf{x}) &= -\nabla^2 \exp\left(-\frac{1}{2\sigma^2}|\mathbf{x}|^2\right) \\ &= \frac{(2 - |\mathbf{x}/\sigma|^2)}{\sigma^2} \exp\left(-\frac{1}{2\sigma^2}|\mathbf{x}|^2\right)\end{aligned}\quad (4.50)$$

and in the frequency domain as

$$\hat{\psi}_{\text{MH}}(\boldsymbol{\omega}) = \sigma^2 |\boldsymbol{\omega}|^2 \exp\left(-\frac{\sigma^2}{2} |\boldsymbol{\omega}|^2\right) \quad (4.51)$$

where σ is a parameter to control the width of the wavelet. According to Eq.(4.50), the 2D-MHW is the Laplacian of Gaussian. Because the Laplacian operator is an isotropic operator, the 2D-MHW is rotationally invariant. In addition, the 2D-MHW is a real-valued wavelet, so it cannot be directly used for fringe pattern analysis which demands an analytic wavelet. A solution to this problem is to form the fringe pattern as an analytic signal by using the Hilbert transform, and then the fringe pattern analysis can be carried out with the real-valued wavelet [41]. An alternative is to adapt the 2D-MHW in the frequency domain to an analytic function by using the Heaviside function $H(\boldsymbol{\omega})$ to enforce the negative frequency components being zeros. This wavelet, named the 2D analytic Mexican hat wavelet (2D-AMHW) here, is given by

$$\hat{\psi}_{\text{AMH}}(\boldsymbol{\omega}) = \sigma^2 |\boldsymbol{\omega}|^2 \exp\left(-\frac{\sigma^2}{2} |\boldsymbol{\omega}|^2\right) H(\boldsymbol{\omega}) \quad (4.52)$$

where $H(\boldsymbol{\omega}) = 1$ for $\omega_x \geq 0$ or $\omega_y \geq 0$, and $H(\boldsymbol{\omega}) = 0$ for otherwise.

Another commonly used isotropic wavelet is the 2D Paul wavelet (2D-PW) [107], and it is defined in the time domain as

$$\psi_P(\mathbf{x}) = \frac{2^n i^n n! (1 - i|\mathbf{x}|)^{-(n+1)}}{\sqrt{\pi(2n)!}} \quad (4.53)$$

where i is the imaginary unit, n is the order of the 2D-PW and is usually set to four for getting appropriate vanishing moments. In the frequency domain, the 2D-PW can be expressed as

$$\hat{\psi}_P(\boldsymbol{\omega}) = \frac{2^n}{\sqrt{n(2n-1)!}} |\boldsymbol{\omega}|^n \exp(-|\boldsymbol{\omega}|) H(\boldsymbol{\omega}) \quad (4.54)$$

According to Eq. (4.53), the 2D-PW is a complex-valued wavelet; meanwhile, it is also an analytic wavelet based on Eq. (4.54). Hence, the 2D-PW can be directly employed in fringe pattern analysis [36].

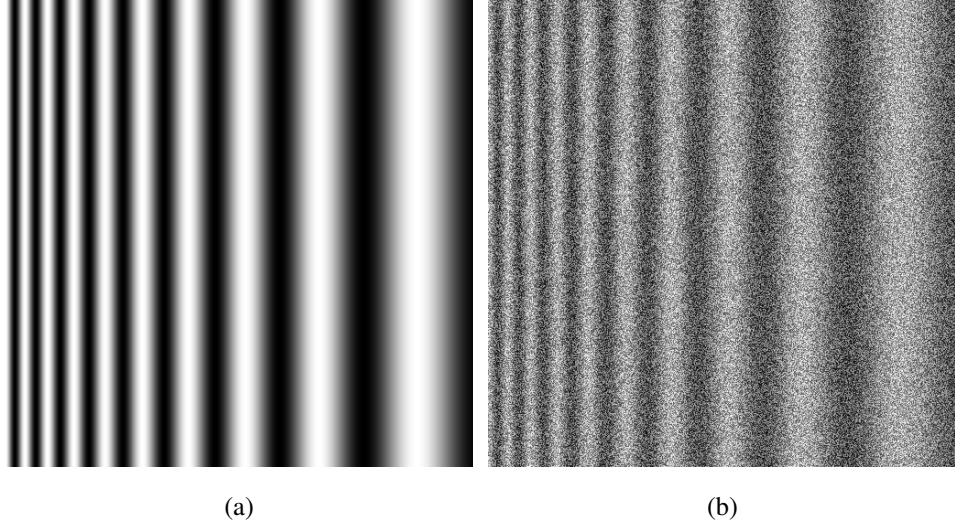


Figure 4.18: Simulated interferogram: (a) without noise, and (b) with noise

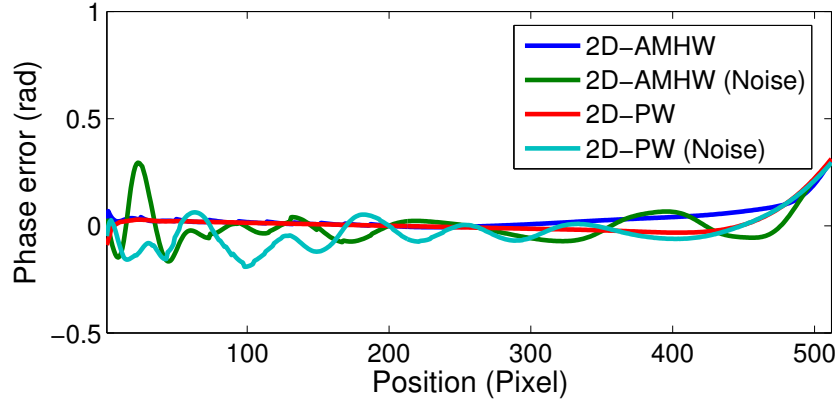


Figure 4.19: Errors of phase extracted by using isotropic wavelets.

To evaluate the performance of different wavelets in the 2D-CWT fringe pattern analysis, two monotonic fringe patterns of 512×512 pixels that represent a linear chirp signal are generated by computer simulation using the following equation:

$$\phi(\mathbf{x}) = 2\pi \cdot \frac{\mathbf{x}}{p} \quad (4.55)$$

Without the loss of generality, the simulation utilizes a case where the singal period p is a

function of x only. Specifically, $p = \frac{1}{15}x + 20$. For the two fringe patterns, one is noise-free, and the other is contaminated with an additive white noise of the signal-to-noise ratio $\text{SNR} = 10 \lg(I_{\text{Signal}}/I_{\text{Noise}})^2 = -6 \text{ dB}$, as shown in figures 4.18 (a) and (b), respectively.

Figure 4.19 shows the errors of the extracted phase along the horizontal center lines of the interferograms. The results indicate that both the 2D-AMHW and 2D-PW work well for the noise-free interferogram, but the performance is dropped remarkably for the noise-contaminated interferogram. The reason can be explained by the theory of filtering in the frequency domain as follows. Equations (4.52) and (4.54) indicate that both the 2D-AMHW and 2D-PW are a kind of band-pass filter, as figure 4.20 shows. When the scale factor varies, the cutoff frequencies of the filter will change and the passband will shrink or expand. However, this change occurs isotropically in all the directions [108], which makes the filter unable to eliminate the noise effectively and the directional phase distribution hard to distinguish. Consequently, notable errors in the phase extraction can be introduced when the noise level is high.

Because of their poor anti-noise performance and inability to detect directional information of fringes, isotropic wavelets are not suitable for real applications in practice. Instead, directional wavelets are preferred.

4.5.2 Directional Wavelets

A typical directional wavelet is the 2D Morlet wavelet (2D-MW), which is expressed in the time domain as

$$\psi_M(\mathbf{x}) = \exp(i\omega_0 \cdot \mathbf{x}) \exp\left(-\frac{|\mathbf{x}|^2}{2\sigma^2}\right) - \exp\left(-\frac{|\sigma^2\omega_0|^2}{2\sigma^2}\right) \exp\left(-\frac{|\mathbf{x}|^2}{2\sigma^2}\right) \quad (4.56)$$

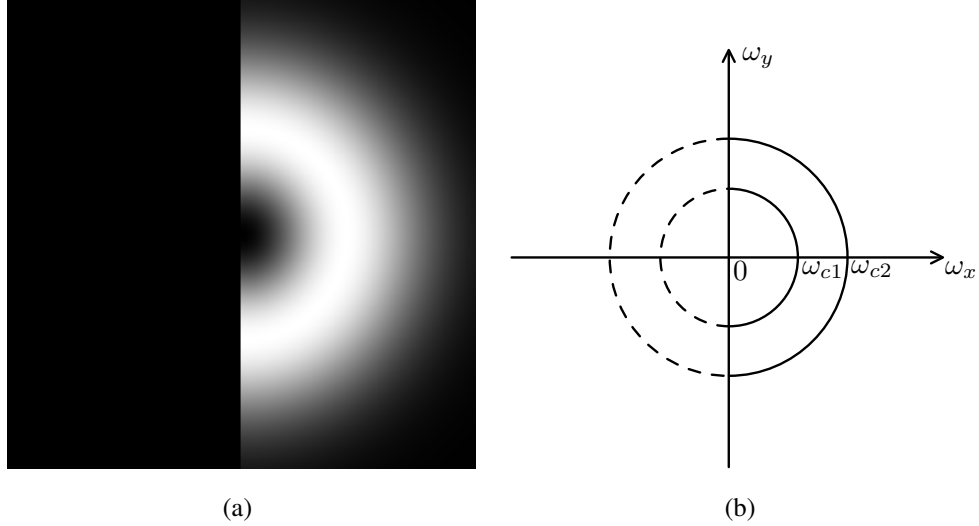


Figure 4.20: Isotropic wavelets with $H(\boldsymbol{\omega}) = 1$ for $\omega_x \geq 0$ in the frequency domain: (a) grayscale illustration, and (b) schematic with the cutoff frequencies denoted as $(\omega_{c1}, \omega_{c2})$.

and in the frequency domain as

$$\hat{\psi}_M(\boldsymbol{\omega}) = \sigma^2 \exp\left(-\frac{\sigma^2}{2} |(\boldsymbol{\omega} - \boldsymbol{\omega}_0)|^2\right) - \sigma^2 \exp\left(-\frac{\sigma^2 |\boldsymbol{\omega}_0|^2}{2}\right) \exp\left(-\frac{\sigma^2 |\boldsymbol{\omega}|^2}{2}\right) \quad (4.57)$$

where $\boldsymbol{\omega}_0$ is called the modulated frequency. The second term on the right side of each equation is a correction term to make the 2D-MW satisfy the admissibility condition, i.e. $\hat{\psi}_M(\mathbf{0}) = 0$ in the frequency domain. It can be seen from equation (4.57) that when $\sigma|\boldsymbol{\omega}_0|$ is large enough, the correction term at $|\boldsymbol{\omega}| = 0$ becomes very small and can be neglected. In this case, the truncated 2D-MW becomes the 2D Gabor wavelet (2D-GW), which is widely used in fringe pattern analysis. Unless otherwise specified, the 2D-MW means the 2D-GW in this section.

Equations (4.56) and (4.57) reveal that the performance of the 2D-MW is affected by both $\boldsymbol{\omega}_0$ and σ . On the one hand, $\boldsymbol{\omega}_0$ modulates the mother wavelet and affects the center frequency of the passband in the frequency domain; typically, a larger $\boldsymbol{\omega}_0$ can yield better

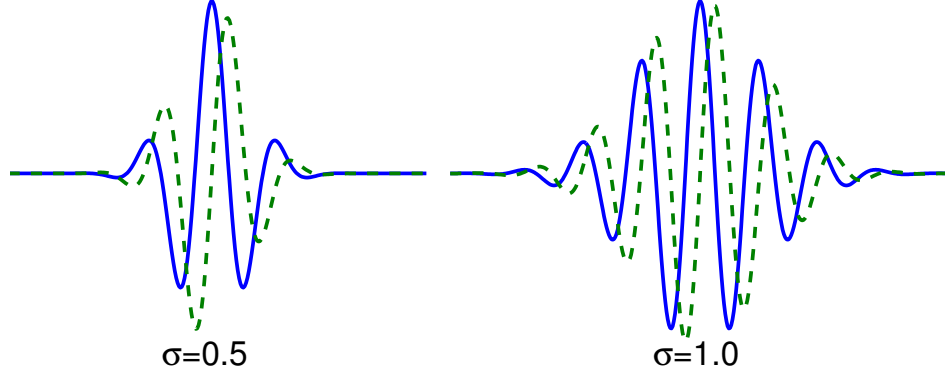


Figure 4.21: The Morlet wavelet with different σ in the time domain.

performance for high frequency fringes. On the other hand, σ determines the wavelet width and affects the anti-noise performance; for example, a small σ helps detect large local fringe variations, while a large σ tends to smooth out the local fringe variations and makes the 2D-MW more robust to noise and defects.

In practice, since equation (4.57) indicates that ω_0 and σ are coupled together, the selection of either ω_0 or σ must be based on fixing another of them. Generally, $|\omega_0| = 2\pi$ is adopted to let the scale factors of the 2D-CWT correspond to the fringe periods. In this case, the associated most effective σ for typical fringe pattern analysis is experimentally shown to be around $0.5 \sim 0.7$. This can also be seen from Fig. 4.21, which shows that a larger σ leads to a wider wavelet distribution, and therefore introduces more oscillations than a smaller one. Compared with $\sigma = 1.0$, $\sigma = 0.5$ is preferred because the mother wavelet has few oscillations and is more suitable for detecting local fringe information [39], which is normally required in practical fringe pattern analysis. With $|\omega_0| = 2\pi$ and $\sigma = 0.5$, $\widehat{\psi}_M(\mathbf{0}) = 0.0072$ based on equation (4.57), the value is small and can be treated as satisfying the admissibility condition in real applications.

Compared with isotropic wavelets, the 2D-MW is also a kind of band-pass filter but with

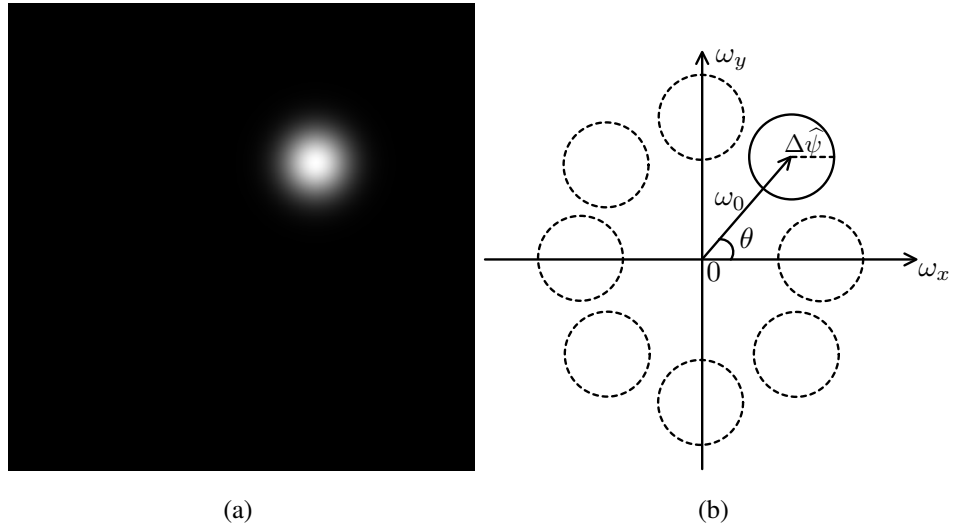


Figure 4.22: Directional wavelets in the frequency domain: (a) grayscale illustration, and (b) schematic with the modulated frequency ω_0 and radius $\Delta\hat{\psi}$.

different behaviors. From Fig. 4.22, it can be seen that the passband of the 2D-MW has a circular shape determined by the modulated frequency ω_0 and the radius $\Delta\hat{\psi} = \sqrt{2}/(2\sigma)$ instead of a ring centered at the origin as Fig. 4.20 shows. More important thing is that the center frequency and radius of the passband can be adjusted by varying the scale factors s and rotation angle θ . This localized analysis characteristic gives the 2D-MW a capability to better cope with the noise and distinguish the directional phase information. Nevertheless, because the selection of ω_0 and σ is constrained by the admissibility condition, the 2D-MW does not perform well with the low-frequency fringes [39].

Furthermore, in order to evaluate the performance of directional wavelets more quantitatively, the scale resolving power (SRP) and the angular resolving power (ARP) in the frequency domain are introduced in Eq. (4.58) [95].

$$\text{SRP}(\hat{\psi}) = \frac{|\omega_0| + \Delta\hat{\psi}}{|\omega_0| - \Delta\hat{\psi}} \quad \text{ARP}(\hat{\psi}) = \arcsin\left(\frac{\Delta\hat{\psi}}{|\omega_0|}\right) \quad (4.58)$$

And the SRP and ARP for the 2D-MW are

$$\text{SRP}(\hat{\psi}_M) = \frac{|\omega_0| + \frac{\sqrt{2}}{2\sigma}}{|\omega_0| - \frac{\sqrt{2}}{2\sigma}} \quad \text{ARP}(\hat{\psi}_M) = \arcsin\left(\frac{\frac{\sqrt{2}}{2\sigma}}{|\omega_0|}\right) \quad (4.59)$$

More specifically, when the modulated frequency $|\omega_0| = 2\pi$ and $\sigma = 0.5$, the $\text{SRP}(\hat{\psi}_M) = 1.5809$ and the $\text{ARP}(\hat{\psi}_M) = 0.227(\text{rad}) = 13.006^\circ$.

However, due to the constraint of the admissibility condition, the modulated frequency ω_0 of the 2D-MW cannot be decreased any more. It impacts the performance of the 2D-MW for analyzing lower frequency components. To further improve the performance of the 2D-CWT technique without loss of all the advantages of the 2D-MW, a combination of the 2D-MHW and 2D-MW can be used in the fringe pattern analysis. The wavelet, called the 2D modulated Mexican hat wavelet (2D-MMHW), is given by [95]

$$\begin{aligned} \psi_{\text{MMH}}(\mathbf{x}) &= -\nabla^2\psi_M \\ &= \frac{2 - |(\mathbf{x}/\sigma - i\sigma\omega_0)|^2}{\sigma^2} \exp(i\omega_0 \cdot \mathbf{x}) \exp\left(-\frac{|\mathbf{x}|^2}{2\sigma^2}\right) \end{aligned} \quad (4.60)$$

and

$$\hat{\psi}_{\text{MMH}}(\omega) = \sigma^2|\omega|^2 \exp\left(-\frac{\sigma^2}{2}|(\omega - \omega_0)|^2\right) \quad (4.61)$$

in the time and frequency, respectively. It is easy to see that the 2D-MMHW always satisfies the admissibility condition regardless of ω_0 and σ , i.e. $\hat{\psi}_{\text{MMH}}(\mathbf{0}) = 0$. This allows using flexible ω_0 and σ to potentially improve the performance of the 2D-CWT fringe pattern analysis.

From Eq. (4.58) the SRP and ARP for the 2D-MMHW are

$$\text{SRP}(\hat{\psi}_{\text{MM}}) = \frac{|\omega_0^*| + \Delta\hat{\psi}^*}{|\omega_0^*| - \Delta\hat{\psi}^*} \quad \text{ARP}(\hat{\psi}_{\text{MM}}) = \arcsin\left(\frac{\Delta\hat{\psi}^*}{|\omega_0^*|}\right) \quad (4.62)$$

where

$$|\omega_0^*| = |\omega_0| + \frac{8\sigma^2|\omega_0|^3 + 12|\omega_0|}{4\sigma^4|\omega_0|^4 + 12\sigma^2|\omega_0|^2 + 3} \quad (4.63)$$

$$\Delta\hat{\psi}^* = \sqrt{\frac{8\sigma^6|\omega_0|^6 + 60\sigma^4|\omega_0|^4 + 90\sigma^2|\omega_0|^2 + 15}{8\sigma^6|\omega_0|^4 + 24\sigma^4|\omega_0|^2 + 6\sigma^2} - |\omega_0^*|^2} \quad (4.64)$$

More specifically, when the modulated frequency $|\omega_0| = 5$ and $\sigma = 0.5$, $\omega_0^* = 6.3234$ and $\Delta\hat{\psi}^* = 1.2774$. Hence, the SRP($\hat{\psi}_{MM}$) = 1.5063 and the ARP($\hat{\psi}_{MM}$) = 0.2034(rad) = 11.6549°. Or with $|\omega_0| = 2\pi$ and $\sigma = 0.3$, the SRP($\hat{\psi}_{MM}$) = 1.4312 and the ARP($\hat{\psi}_{MM}$) = 0.1783(rad) = 10.2167°. Compared with the 2D-MW, the 2D-MMHW has better resolution in terms of both the SRP and ARP. Moreover, both the modulated frequency and σ can be adjusted to deal with different cases. Hence, the performance of the 2D-MMHW for lower frequency components will be better than the 2D-MW because by virtue of the flexibility of varying parameters.

Similar to the 2D-MW, $|\omega_0| = 2\pi$ is employed in the 2D-MMHW, and the analysis performance can be enhanced by choosing an appropriate σ . Based on the testings we performed, σ is determined to be in the range of $0.2 \sim 0.5$, and $\sigma = 0.3$ (with $|\omega_0| = 2\pi$) is suggested for the 2D-MMHW. In general, a larger σ gives better anti-noise performance but yields lower accuracies on analyzing fringes with large local frequency variations.

Figure 4.23 shows the errors of phase extracted from the same simulated interferograms used previously in the evaluation of isotropic wavelets. Compared with the isotropic wavelets, the superior of the directional wavelets are evident. In the simulation, $|\omega_0| = 2\pi$ [i.e. $\omega_0 = (2\pi, 0)$ with $\theta = 0$] and $\sigma = 0.5$ are used for both wavelets. It is noteworthy that because the fringe periods have rapid variations and are cut off abruptly, the analysis gives relatively large errors at the left and right ends. This inherent limitation of the CWT technique can be overcome by using carriers in actual experiments, and image border extension by data padding may also be used for fringes with relatively small variations.

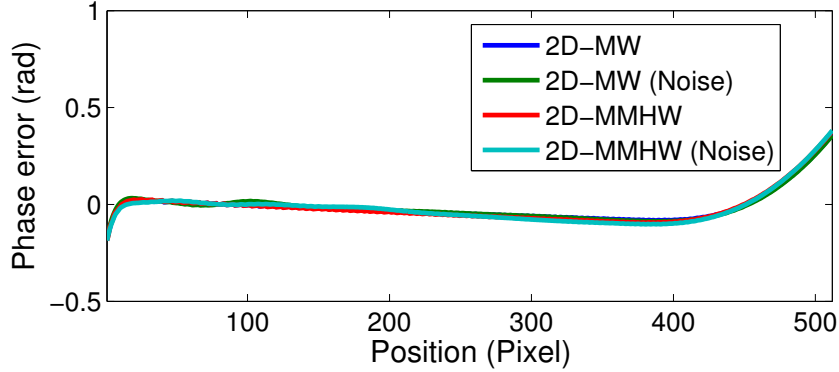


Figure 4.23: Errors of phase extracted by using directional wavelets.

4.5.3 Simulation

To further compare the 2D-MW and the 2D-MMHW, an additional computer-simulated interferogram has been analyzed by using the two directional wavelets with various parameters. The peaks fringe pattern of 512×512 pixels generated by using Eq. (2.25) is shown in Fig. 4.24, where the SNRs of the background and the additive white noise are 0 dB and -6 dB, respectively.

In the analysis, the scale factors $s \in [10, 25]$ and the rotation angles $\theta \in [-\pi/2, \pi/2)$ are employed. Table 4.1 shows the mean relative errors of the extracted phase, defined as $\frac{1}{N} \sum_{k=1}^{k=N} \left| \frac{\phi_{\text{exp}}(k) - \phi_{\text{true}}(k)}{\phi_{\text{true}}(k)} \right|$, along two representative lines ($y = 118$ pixel and $y = 385$ pixel) where the phase distributions have relatively large variations. The results for the entire interferogram are included in the table as well. It can be seen that with $|\omega_0| = 2\pi$, the best results are obtained with $\sigma = 0.5$ and $\sigma = 0.3$ for the 2D-MW and 2D-MMHW, respectively. The 2D-MMHW provides better performance than the 2D-MW because it introduces the freedom of choosing σ . The results also demonstrate that σ beyond $[0.5, 0.7]$ for the 2D-MW and $[0.3, 0.5]$ for the 2D-MMHW give large errors or even fail the analysis.

Table 4.1: Mean relative errors of phase extracted by using directional wavelets with $|\omega_0| = 2\pi$ and various σ .

σ	y=118 (pixel)		y=385 (pixel)		entire image	
	$\hat{\psi}_M$	$\hat{\psi}_{MMH}$	$\hat{\psi}_M$	$\hat{\psi}_{MMH}$	$\hat{\psi}_M$	$\hat{\psi}_{MMH}$
0.1	1.6295	4.1473	2.8435	0.6832	0.6147	0.5040
0.2	1.5777	0.0104	2.7956	0.0190	0.7365	0.0061
0.3	1.5706	0.0066	2.4554	0.0043	0.3753	0.0003
0.4	1.0593	0.0090	1.2370	0.0065	0.1860	0.0070
0.5	0.0128	0.0113	0.0081	0.0098	0.0058	0.0076
0.6	0.0202	0.0221	0.0159	0.0164	0.0069	0.0128
0.7	0.0208	0.0243	0.0161	0.0171	0.0177	0.0160
0.8	0.0294	0.0230	0.0204	0.0139	0.0083	0.0041
0.9	0.0209	0.0283	0.0238	0.0214	0.0078	0.0048
1.0	0.0258	0.0210	0.0277	0.0200	0.0127	0.0063

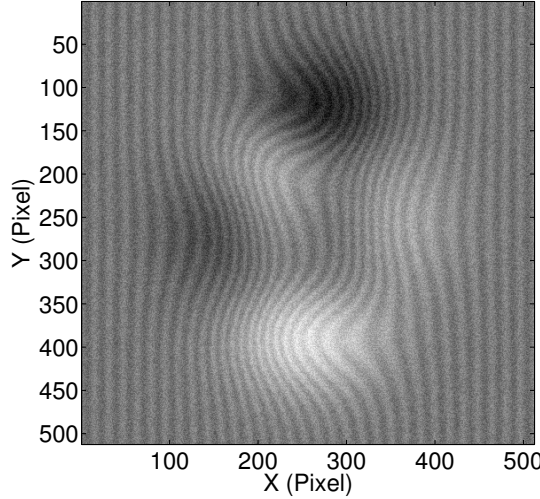


Figure 4.24: Simulated interferogram with large local fringe variations.

4.6 Hybrid Technique

As mentioned in Sec. 3.1, the PS technique is sensitive to the noise and defects presented in the interferograms, which impairs the application of the technique when noise-free results are demanded. In order to reduce the noise level, a straightforward way is to apply a filtering process to the determined phase data, but this may smear the phase map. However, the combination of the classic PS technique and the filtering technique is insufficient to correctly obtain the full-field phase map from interferograms that contain defects and corrupted fringes. To cope with the noise and defects simultaneously, a robust adaptive filtering technique with the capability of detecting local fringe information is usually required.

In order to improve the result, the FTM [10] and the WFT [11] have been proposed for phase-shifting interferograms. Compared with the FT technique, the WFT is more robust to noise in fringe pattern analysis. But the WFT technique still need a pre-filtering, e.g., in the windowed Fourier filtering (WFF) method. Moreover, the WFT technique has a fixed size

window in the sense of time-frequency analysis which limits its performance.

By virtue of the flexible time-frequency analysis window, the 2D-CWT technique has also been successfully applied to analyze single fringe patterns in numerous applications [27, 28, 41, 109]. The 2D-CWT technique normally requires only a single interferogram or fringe pattern to retrieve the full-field phase information. However, as mentioned in Sec. 4.2.2, for the fringes patterns with a monotonic phase distribution, the 2D-CWT technique works very well. But for the complex fringe patterns whose phase distribution is not monotonic, e.g., the close fringe patterns, the phase distribution cannot be determined correctly due to the phase ambiguity. Therefore, one or more post processing techniques are required, for example, the PDR and interpolation or extrapolation techniques described in Sec. 4.3 [39]. Fortunately, the phase ambiguity is vanished automatically when more interferograms are involved in the analysis. For instance, the PS technique is successful to extract the phase distribution of complex fringe patterns by using at least three interferograms. But the disadvantage of the PS technique is highly noise-sensitive. When the interferograms have some noises or defects, the determination of the phase will be failed by using the PS technique. Hence, combining the 2D-CWT and PS technique will provide a perfect solution for fringe pattern analysis without phase ambiguity and with the ability of anti-noise.

In this section, a hybrid technique that takes the advantages of both the PS and 2D-CWT techniques is elaborated to accurately extract the full-field phase distributions from analyzing multiple phase-shifted interferograms. The technique can analyze virtually any kinds of interferograms, including those with phase ambiguities, large fringe-frequency variations, noise, and defects [110].

4.6.1 Principle

As mentioned in Sec. 3.1, the most commonly used PS technique is the four-frame technique. However, when the noise exists, e.g., the additive white noise, the real part of the complex intensity in Eq. (3.14) becomes

$$I_4 - I_2 = I_{\text{bn}}(\mathbf{x}) + 2I_a(\mathbf{x}) \sin[\phi(\mathbf{x})] \quad (4.65)$$

and the imaginary part becomes

$$I_1 - I_3 = I_{\text{bn}}(\mathbf{x}) + 2I_a(\mathbf{x}) \cos[\phi(\mathbf{x})] \quad (4.66)$$

where $I_{\text{bn}}(\mathbf{x}) = I_b(\mathbf{x}) + N(\mathbf{x})$ and $N(\mathbf{x})$ represents the additive white noise. Obviously, the background intensity cannot be eliminated by subtraction and the phase distribute cannot be extract correctly by using Eq. (3.15). However, by compared with Eq.(2.17), equations (4.65) and (4.66) have the similar form, which means the 2D-CWT technique can be used to extract the phase distribution without the noise problem. Moreover, the phase ambiguity has already eliminated by subtraction in Eqs. (4.65) and (4.66). An extra phase determination rule is not required any more. Compared with the conventional 2D-CWT, the rotation angle of the proposed technique must be $\theta \in [-\pi, \pi]$ or $[0, 2\pi)$ due to Eq.(3.14) is a complex signal instead of a real-value signal in Eq.(2.17) whose analysis only relies on the positive frequency domain.

Furthermore, denoting the local fringe period and orientation at an arbitrary point \mathbf{u} in an interferogram as $S(S > 0)$ and $\Theta(0 \leq \Theta < 2\pi)$, respectively, the local information of the complex signal described by Eq. (3.14) at \mathbf{x} around \mathbf{u} can be written as

$$I(\mathbf{x}) = \frac{N}{2} I_a \exp \left\{ i [2\pi S^{-1} \mathbf{n} \cdot (\mathbf{x} - \mathbf{u}) + \phi(\mathbf{u})] \right\} \quad (4.67)$$

where I_a is treated as constants in the local region, and $\mathbf{n} = (\cos \Theta, \sin \Theta)$. Substituting Eqs. (4.67) and (4.39) into Eq. (4.1) can simplify the wavelet coefficient as

$$\begin{aligned}\mathcal{W}(\mathbf{u}, s, \theta) = \\ N\pi\sigma^2 I_a \exp \left(-2\pi^2\sigma^2 \left\{ \left(\frac{s}{S} - 1 \right)^2 + 2\frac{s}{S} [1 - \cos(\Theta - \theta)] \right\} \right) \exp [i\phi(\mathbf{u})]\end{aligned}\quad (4.68)$$

The equation reveals that the wavelet coefficient modulus can reach maximum when $s = S$ and $\theta = \Theta$. As mentioned in Sec. 4.1.2, the point $(\mathbf{u}, s = S, \theta = \Theta)$ is called a wavelet ridge, and the corresponding wavelet coefficient is given by

$$\mathcal{W}(\mathbf{u}, s, \theta)_{\text{ridge}} = N\pi\sigma^2 I_a \exp [i\phi(\mathbf{u})] \quad (4.69)$$

Consequently, the phase distribution of the original interferogram can be obtained from the wavelet coefficients by using the DRD algorithm in Sec. 4.2.

It is noteworthy that if a single interferogram described by Eq.(3.1) is analyzed by using the 2D-CWT technique, as mentioned before in Sec. 4.2.2, there are two wavelet ridges that yield identical wavelet coefficients at every pixel of the interferogram [39]. This subsequently gives two phase values with opposite signs, and consequently leads to a problem of phase ambiguity for the analysis of interferograms with complex fringe orders. As can be seen from the above description, the phase ambiguity problem does not exist in the proposed 2D-CWT analysis of phase-shifted interferograms.

From the view of signal processing, the 2D-CWT acts as a fringe-matching filter to detect the local signal information while suppressing the noise and defects in the interferogram. In the conventional 2D-CWT analysis where a single interferogram is used, the signal described by Eq. (3.1) involves a cosine function. Unless the interferogram is simple such that the full-field phase is monotonically distributed along certain directions, there are two possible solutions for the phase (i.e. ϕ and $-\phi$ or $2\pi - \phi$). On the contrary, the proposed 2D-CWT

analysis uses multiple phase-shifted interferograms, and the complex signal described by Eq. (3.14) contains a cosine function in the real part and a sine function in the imaginary part. The complex signal provides sufficient information to determine a unique solution for the phase. Consequently, with its original advantages and new feature, the proposed hybrid 2D-CWT technique has the capability to analyze phase-shifted interferograms containing complex fringes as well as noise and defects.

4.6.2 Algorithm

The procedure of the proposed hybrid technique combining the 2D-CWT algorithm and the phase-shifting algorithm is described as follows:

1. Construct the complex signal $I(\mathbf{x})$ from a series of phase-shifted interferograms by using Eq. (3.10), and calculate the Fourier transform of $I(\mathbf{x})$ as $\hat{I}(\boldsymbol{\omega})$.
2. Determine the wavelet ridges by using the direct ridge detection algorithm from a specified group of scale factors s and the rotation angles $\theta \in [0, 2\pi)$.
 - (a) Select a parameter pair of s_k and θ_k .
 - (b) Calculate the Fourier transform of the daughter wavelet as $\hat{\psi}_k(\boldsymbol{\omega})$.
 - (c) Obtain the wavelet coefficients $\mathcal{W}(\mathbf{u}, s_k, \theta_k)$ by calculating the inverse Fourier transform of the multiplication of $\hat{I}(\boldsymbol{\omega}) \cdot \hat{\psi}_k(\boldsymbol{\omega})$.
 - (d) Examine all the combination pairs of s and θ , and find the wavelet ridge $\mathcal{W}(\mathbf{u}, s, \theta)_{\text{ridge}}$ for every pixel of the interferogram.
3. Obtain the phase distribution by using Eq. (4.18).

4.6.3 Simulation

A computer simulation has been carried out to verify the effectiveness of the technique by applying the 2D-CWT in phase-shifting interferograms. In the simulation, four phase-shifted fringe patterns are generated with phase-shifting amounts $\delta = \{0, \pi/2, \pi, 3\pi/2\}$. Moreover, an additive white noise with the SNR = -6 dB and some defects, i.e. scratches here, have been added to the interferograms, which are shown in Fig. 4.25. It is clear that the scratches have corrupted the fringe patterns, and this can bring substantial errors to the phase determined by the classic PS technique. Figure 4.26 shows the simulation results obtained by different analysis techniques, where Fig. 4.26(a) is the ideal wrapped phase map, and Figs. 4.26(b)-(d) are the wrapped phase maps extracted by the four-frame PS technique, the conventional 2D-CWT technique, and the proposed 2D-CWT technique, respectively. In the PS analysis, a Gaussian filter has been pre-applied to the interferograms to reduce the noise. In the 2D-CWT analysis, no filtering is pre-applied, and both the conventional and proposed techniques use the scale factors $s \in [5, 35]$ and the rotation angles $\theta \in [0, 2\pi)$.

When $N(\mathbf{x}) = 0$, i.e. without any noise, the PS technique can extract the phase distribution correctly as Fig. 4.26(a) shows. But with the noise increasing, the phase distribution cannot be determined by the PS technique. Figure 4.26(b) shows that the phase map extracted by the phase-shifting technique still contains notable noise though the noise level has been substantially reduced by a filtering process. It is also clear that the filtering is not helpful for recovering the corrupted fringes.

The noise-insensitive technique should be used, e.g., the 2D-CWT technique. Figure 4.26(c) is the phase map obtained by applying the conventional 2D-CWT technique with PDR and the scale factor $s \in [5, 35]$ and the rotation angle $\theta \in [-\pi/2, \pi/2)$ to the first of the four interferograms. Because the phase values reach extrema and the fringe frequencies

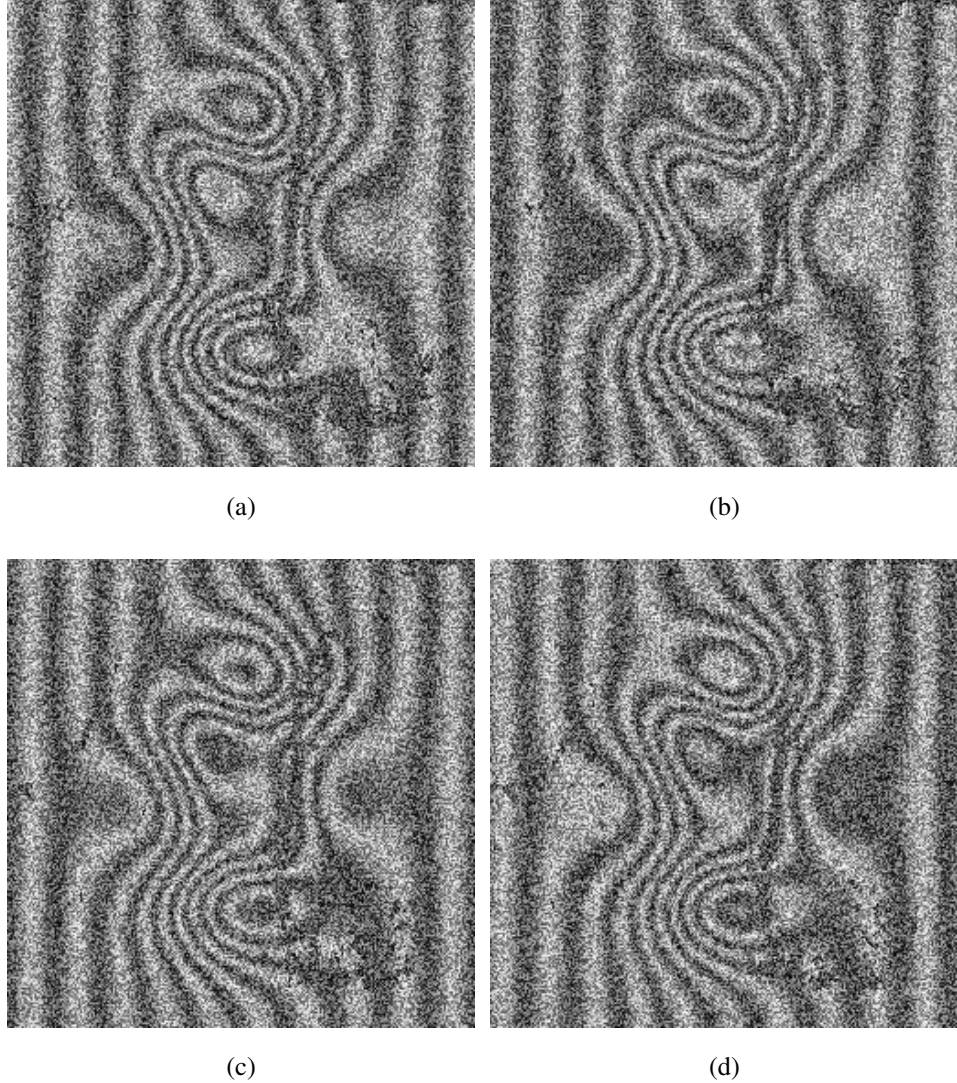


Figure 4.25: Phase-shifted interferograms generated from computer simulation: (a) $\delta = 0$, (b) $\delta = \frac{\pi}{2}$, (c) $\delta = \pi$, and (d) $\delta = \frac{3\pi}{2}$

are low in the center regions and non-monotonic distributions are presented, the phase information cannot be accurately determined there. The phase map determined by the proposed technique is shown in Fig. 4.26(d). By using the proposed 2D-CWT technique in all of the four phase-shifted fringe patterns with $s \in [5, 35]$ and $\theta \in [-\pi, \pi)$, the result shows clearly

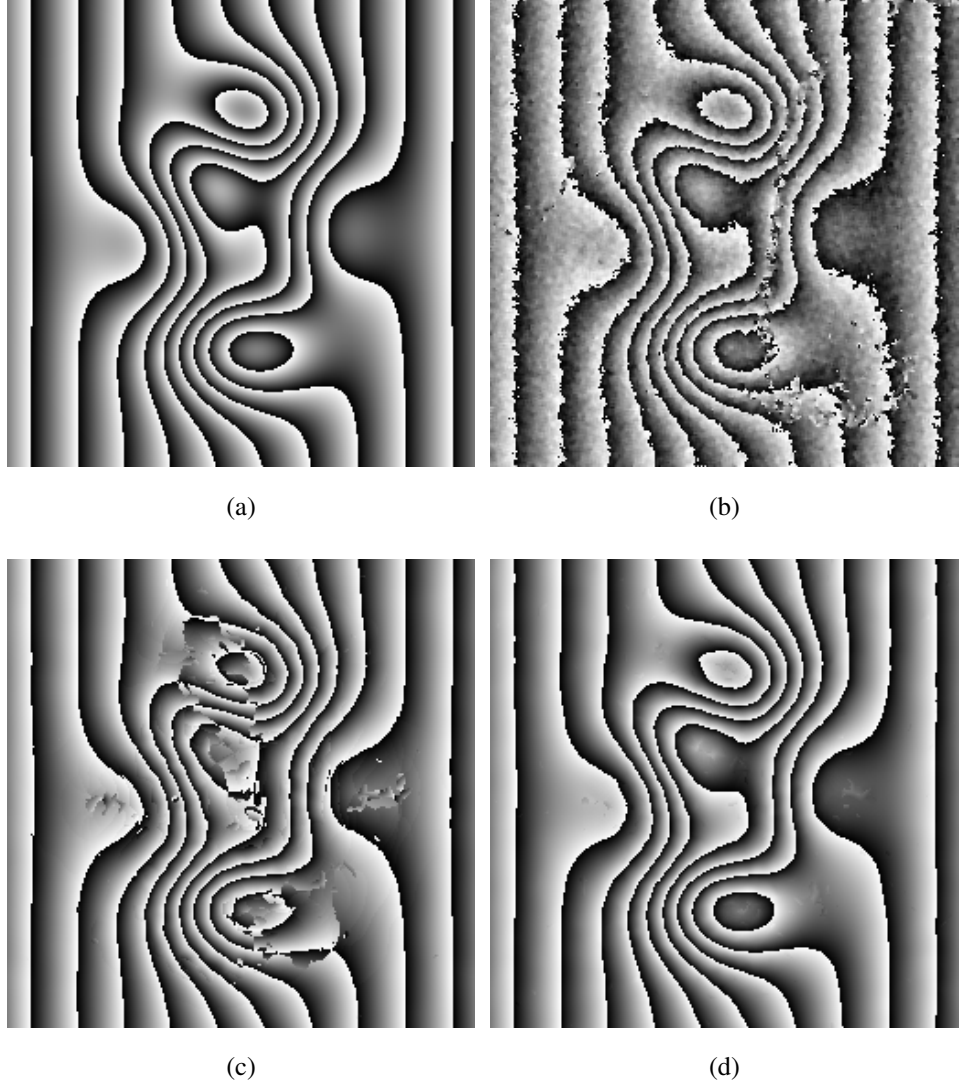


Figure 4.26: Simulation results: (a) ideal wrapped phase map, (b) wrapped phase map with the phase-shifting technique, (c) wrapped phase map with the conventional 2D-CWT technique, and (d) wrapped phase map with the hybrid 2D-CWT techniques.

that the phase distribution is extracted correctly in Fig. 4.26(d).

Furthermore, the unwrapped phase and its three-dimensional view are show in Figs. 4.27(a) and (b), respectively. In order to observe the performance of the proposed technique, a com-

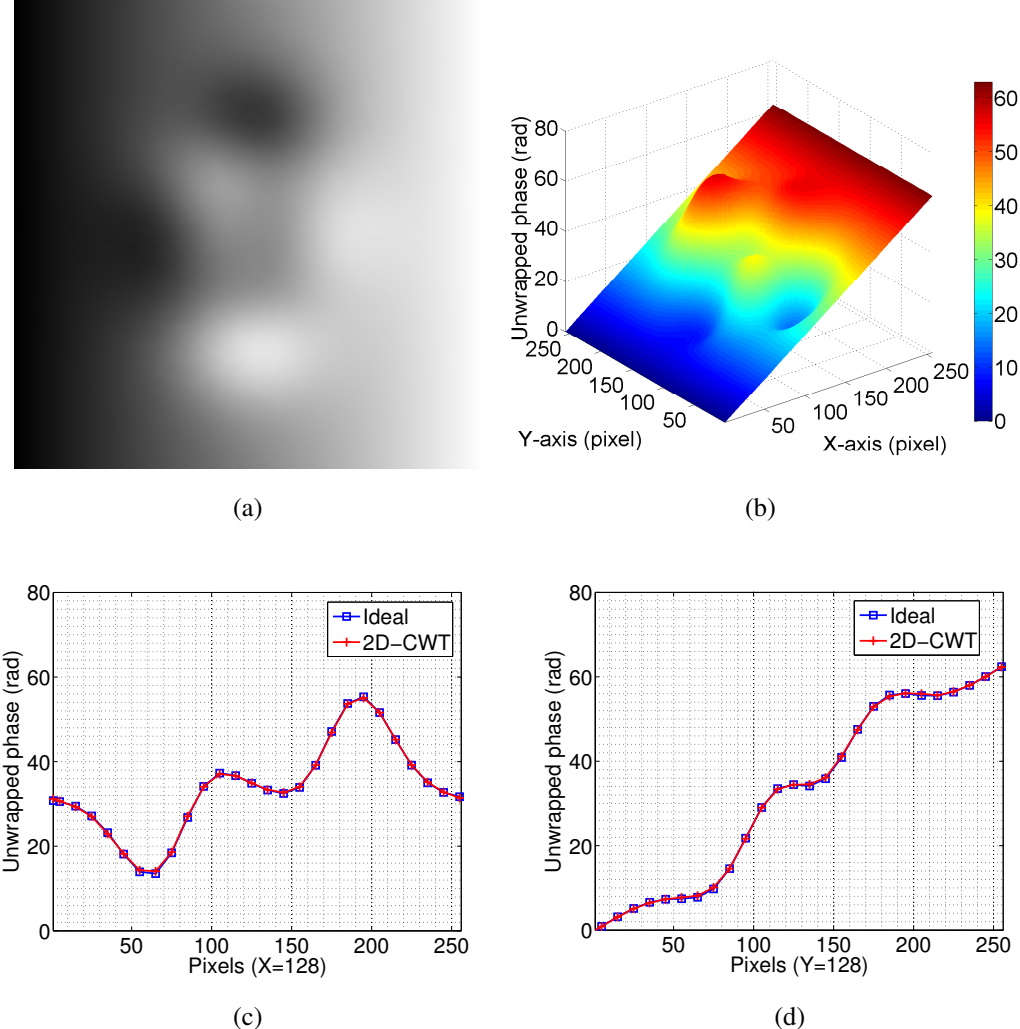


Figure 4.27: Unwrapped phase analysis: (a) unwrapped phase, (b) three-dimensional view of (a), (c) comparison with the ideal phase along $x = 128$ pixel, and (d) comparison with the ideal phase along $y = 128$ pixel

parison between the unwrapped phase and ideal phase is plotted along $x = 128$ pixel in Fig. 4.27(c) and $y = 128$ pixel in Fig. 4.27 (d) where the phase distribution varies abruptly.

By virtue of multiple phase-shifted interferograms, the full-field phase distribution can be correctly extracted. Table 4.2 shows the comparison of analysis accuracies in terms of

Table 4.2: Performance comparison.

Technique	Mean of absolute error (rad)		
	Vertical	Horizontal	Overall
Phase shifting	1.0432	1.0943	1.1223
Conventional 2D-CWT	1.1529	0.6760	0.4826
hybrid 2D-CWT	0.1425	0.1558	0.0861

the mean absolute errors of the phase values along the vertical and horizontal centerlines, as well as the full-field phase data. The results evidently demonstrate the validity the hybrid 2D-CWT technique.

Chapter 5

Experiments

5.1 Warpage Measurement

As mentioned above in Sec. 4.3, the 2D-CWT technique with the PDR works very well with the simulated fringe patterns as Figs. 4.8, 4.9 and 4.10 show. And this technique has been employed to analyze real experimental interferograms as well. Figure. 5.1 shows an example of warpage measurement of a tape-automated bonding package using high-sensitivity Twyman-Green interferometry, where the warpage can be directly computed from unwrapped phase by $w = \lambda\phi/(16\pi)$ with $\lambda = 632.8\text{nm}$.

In the analysis, the rotation angle $\theta \in [0, \pi]$ with an increment of 0.05π and the scale factor $s \in [6, 32]$ with an increment of 0.5 are used to extract phase distributions. It is noted that the defects in the original fringe pattern have been automatically corrected by the 2D-CWT algorithm. Meanwhile, it is important to point out that the 2D-CWT algorithm, due to its inherent characteristic, is usually incapable of processing the local region in which fringe frequencies become much lower when the phase gradients change signs. This can be seen in the center region of Fig. 5.1 (b). The corrupted phase in the region can be

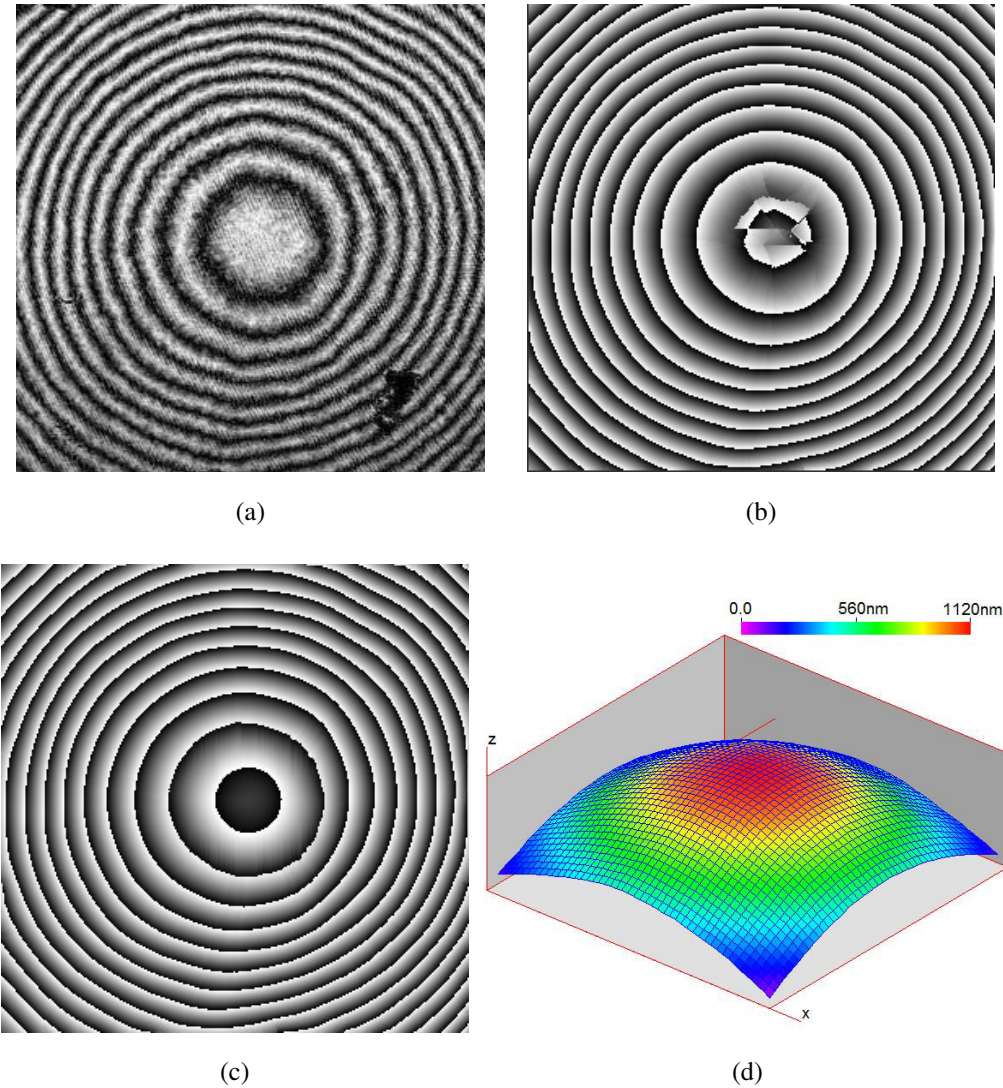


Figure 5.1: Warpage measurement of an electronic package: (a) Fringe pattern (288×288 pixels), (b) Wrapped phase distribution, (c) Refined wrapped phase distribution, and (d) 3D warpage.

replaced by data interpolation and/or extrapolation from the correct phase information in the surrounding regions. The operation can be performed along either horizontal or vertical direction (or both if necessary). Because the fringe frequencies or phase gradients in the

gradient-sign-transition region are much lower than the ones in the surrounding regions, the transition region is normally the least critical in an interferogram. Consequently, using data interpolation or extrapolation will not bring distinctive errors. The refined phase map is

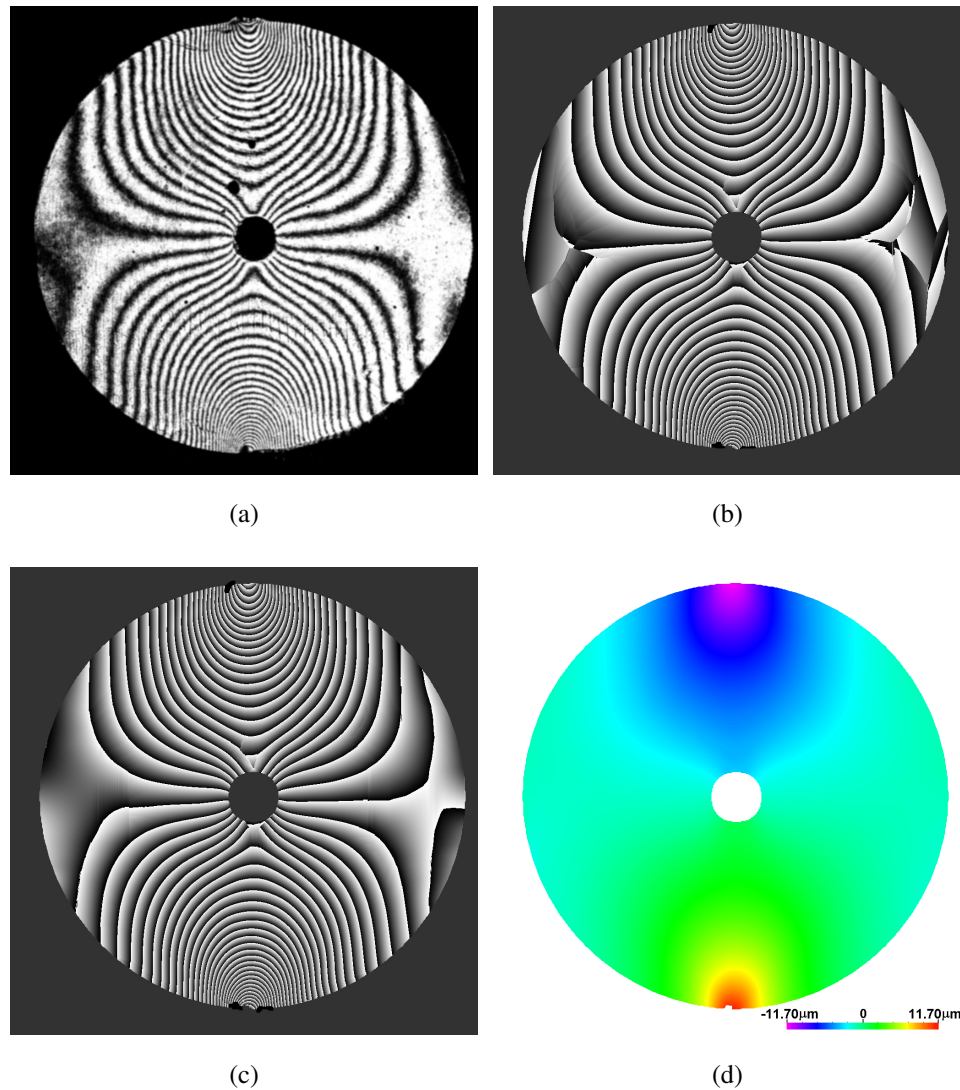


Figure 5.2: Displacement measurement of a circular disc: (a) Fringe pattern (1024×1024 pixels), (b) wrapped phase distribution, (c) refined wrapped phase distribution, and (d) displacement map

shown in Fig. 5.1 (c), and the 3D warpage is shown in Fig. 5.1 (d).

Figure 5.2 shows an application to the vertical displacement fringe pattern of a circular disc under diametrical compression. The experiment was conducted by using moiré interferometry, where the displacement is governed by $v = k\phi/(2\pi)$ with $k = 416.7\text{nm}$. In the analysis, the rotation angle $\theta \in [0, \pi]$ with an increment of 0.05π and the scale factor $s \in [2, 120]$ with an increment of 0.5 are used to extract phase distributions. In this application, data interpolation and extrapolation are carried out along one direction followed by another direction to obtain the full-field data in the left and right regions of the disc where initial phase data are corrupted.

5.2 PBGA Measurement

The approach based on the cover map concept described in Sec. 4.4, which demonstrates a scheme for how to choose a small number of dilation and rotation parameters for 2D-CWT analysis to perform accurate and fast analysis on fringe patterns, has been employed to process a real experimental fringe pattern. The fringe pattern is acquired during the deformation measurement of a plastic ball grid array (PBGA) package subjected to a temperature using high-sensitivity moiré interferometry [57].

As being seen from Fig. 5.3 (a), the moiré pattern contains noisy complex fringes and has quite a few small defects. As previously mentioned in Sec. 4.4, the 2D-CWT technique is robust to noise and has the ability to extract full-field phase distributions while eliminating the defects. Hence, the moiré fringe pattern is suitable for being analyzed by the 2D-CWT technique.

The size of the image shown in Fig. 5.3 (a) is 764×421 pixels, and the periods of the moiré fringes range roughly from 2 to 72 pixels. Therefore, the frequency range is from

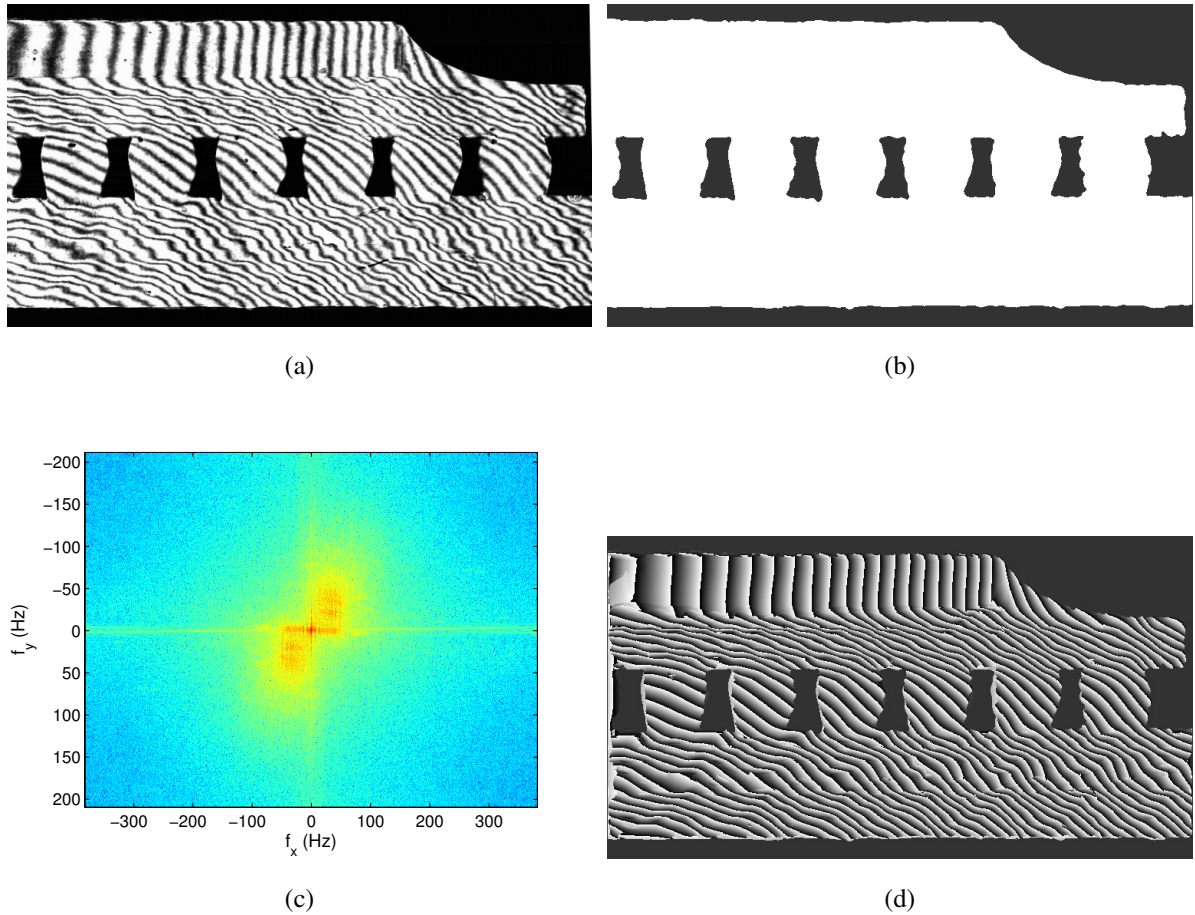


Figure 5.3: Moiré fringe pattern of a PBGA package and the analysis results obtained by the conventional 2D-CWT scheme: (a) fringe pattern, (b) boundary mask, (c) spectrum, and (d) phase map.

around 10.6 to 382 Hz, which can be seen from the spectrum of the fringe pattern in Fig. 5.3 (c). Using the conventional 2D-CWT scheme with $\sigma = 0.5$, the scale factors $s \in [2, 72]$ pixels with an increment of 1 pixel and the rotation angles $\theta \in [0, \pi/2]$ with an increment of 0.1 rad can be used to extract the phase distribution. The result is shown in Fig. 5.3 (d), where the boundary mask shown in Fig. 5.3 (b) has been superposed onto the phase map.

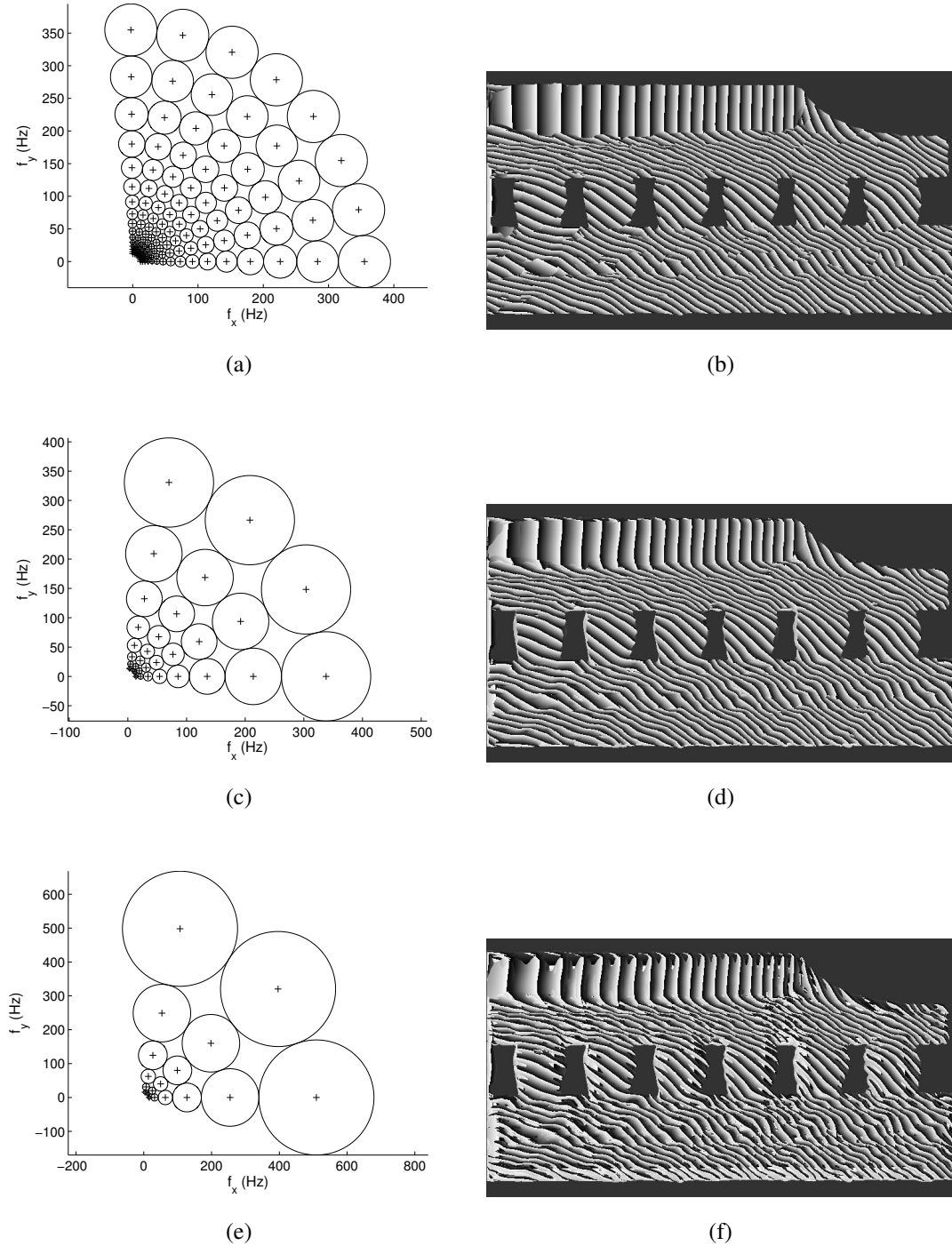


Figure 5.4: Analysis results with different cover map parameters: (a) cover map for $\sigma = 1.0$, (b) phase map from $\sigma = 1.0$, (c) cover map for $\sigma = 0.5$, (d) phase map from $\sigma = 0.5$, (e) cover map for $\sigma = 0.3376$, and (f) phase map from $\sigma = 0.3376$

A problem with this analysis is that the computation time is long due to the small increments of s and θ . As described previously, it is unnecessary to use very small increments for the dilation and rotation parameters in the 2D-CWT analysis. By using the relevant parameters associated with the complete cover maps for $\sigma = 1.0, 0.5$, and 0.3376 , the corresponding extracted phase distributions are obtained and shown in Figs. 5.4 (b), 5.4 (d), and 5.4 (f), respectively. Defining the phase distribution shown in Fig. 5.3 (d) as the reference, the root mean squared errors of the extracted phase are 0.2483 rad, 0.0618 rad, and 0.8924 rad for $\sigma = 1.0, 0.5$, and 0.3376 , respectively. It is evident that the case of $\sigma = 0.5$ matches well with the conventional analysis, and it performs better than the other two. The reason is that $\sigma = 1.0$ leads to relatively low resolution in the time domain, whereas $\sigma = 0.3376$ results in overly high resolution.

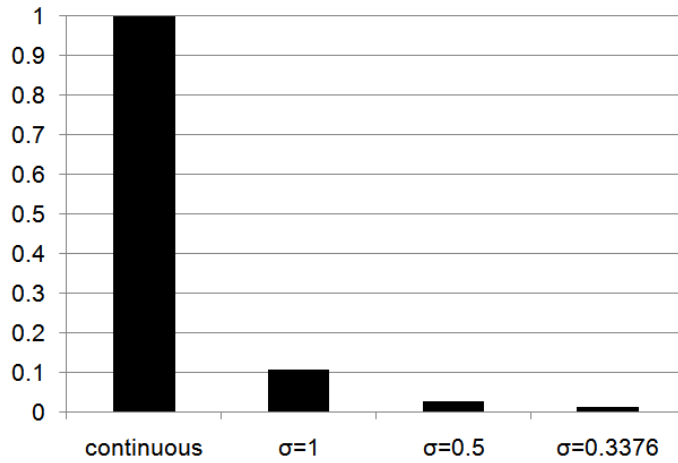


Figure 5.5: Comparison of analysis speed associated with different cover maps.

Because a substantially small number of dilation and rotation parameters are used, the computation efficiency of this 2D-CWT analysis can be dramatically improved. Figure 5.5 shows a comparison of the required computation time associated with different cover maps, where the data have been normalized by setting the conventional one to 1. It is clear that the

approach based on the cover map performs quite well in terms of processing time.

5.3 Thermal Deformation Measurement

The 2D-CWT technique with different mother wavelets mentioned in Sec. 4.5 has been applied to analyze a moiré fringe pattern captured during the thermal deformation measurement of an electronic packaging component. From the experimental image, which is 384×384 pixels, shown in Fig. 5.6, it is clear that the interferogram is noisy and has many defects. As previously mentioned in Sec. 4.5, the phase distribution of such an interferogram generally cannot be extracted accurately by using the isotropic wavelets due to their poor anti-noise capability.

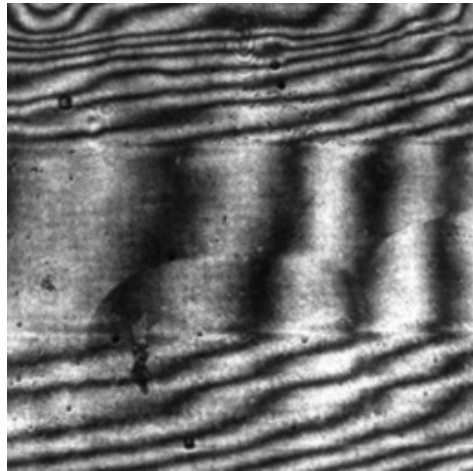


Figure 5.6: A real moiré interferogram.

More specifically, the results are shown in Figs. 5.7 (a) and 5.7 (b) by using the 2D-MHW and 2D-PW, respectively. And the range of the scale factor is $s \in [2, 90]$ in both cases. By comparison, firstly, the 2D-MW is employed to extract the phase distribution which is shown in Fig. 5.7 (c) with the parameters of $\omega_0 = (2\pi, 0)$, $\sigma = 0.5$, $s \in [2, 90]$, and $\theta \in [0, 2\pi]$. It

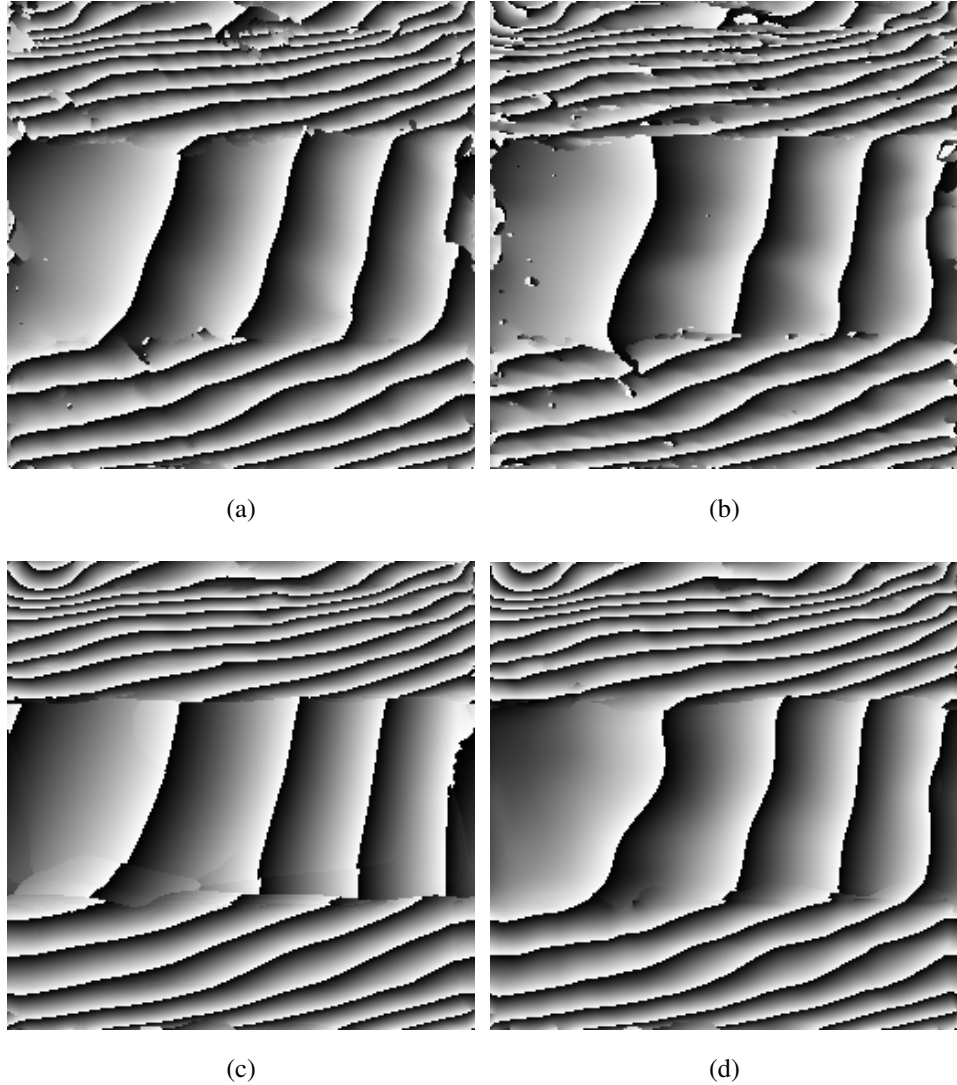


Figure 5.7: Wrapped phase maps extracted by using the 2D-CWT technique with different wavelets: (a) 2D-AMHW, (b) 2D-PW, (c) 2D-MW, and (d) 2D-MMHW.

can be seen that the result is much better than those obtained by using isotropic wavelets and all the noise and defects are eliminated. But the phase distribution is not smooth. In order to improve the result, the parameters must be varied, for example, a smaller σ . However, due to the admissibility condition, σ in the 2D-MW cannot be decreased any more. Hence,

the 2D-MMHW can be used to obtain a better result because either ω_0 and σ can be varied which gives the 2D-MMHW more flexibility. For example, the phase distribution by using the 2D-MMHW is shown in Fig. 5.7 (d). And the parameters are $\omega_0 = (2\pi, 0)$, $\sigma = 0.18$, $s \in [2, 90]$, and $\theta \in [0, 2\pi]$. It is clearly shown that the phase distribution is smoother than the one obtained by using the 2D-MW.

Chapter 6

Conclusions and Future Work

6.1 Conclusions

The 2D-CWT technique is robust for interferogram (or fringe pattern) analysis because it requires only a single interferogram and is insensitive to noise. For a complex interferogram where fringe orders do not change monotonically along a certain direction, there exists a phase determination ambiguity issue in the conventional 2D-CWT analysis with the DRD algorithm. In Sec. 4.3, the PDR is introduced to solve the phase ambiguity problem in 2D-CWT interferogram analysis. The rule is established on the phase distribution continuity, and a frequency-guided scheme is employed to obtain the correct phase at each point. The PDR, which is the key component of the presented technique, makes the 2D-CWT for interferogram analysis practical for real-world applications. The validity and the practicability of the proposed technique have been verified by computer simulation in Sec. 4.3 and real experiments in Sec. 5.1.

In the existing 2D-CWT technique for fringe pattern analysis, by using dilation and rotation parameters with very small increments, the analysis accuracy can be guaranteed but the

entire analysis is normally time-consuming. In order to speed up the analysis without loss of accuracy, the cover map concept is introduced in Sec. 4.4. The cover map allows a substantial discretization of the dilation and rotation parameters. With the proposed approach, once the standard deviation σ is chosen, all the discrete parameters can be easily determined for the 2D-CWT fringe pattern analysis. Typically, $\sigma = 0.5$ is sufficient for the analysis of general fringe patterns even some defects exist. For complex fringe patterns with notable fringe defects, an optimized σ can be sought by trials depending on the actual applications. Compared with the conventional 2D-CWT analysis, the cover map can help remarkably increase the analysis speed. For this reason, it can be practically very useful for processing various kinds of interferograms or fringe patterns in many scientific and engineering applications, especially those highly relying on single-image analysis, such as dynamic interferograms. Computer simulation in Sec. 4.4 and real experiment in Sec. 5.2 help verify the validity and feasibility of the proposed concept and technique.

Moreover, directional wavelets perform better than isotropic wavelets in the 2D-CWT fringe pattern analysis, and thus are recommended for practical applications. In order to satisfy the admissibility condition strictly, the 2D-MMHW is introduced in Sec. 4.5. Compared with the widely used 2D-MW, the 2D-MMHW provides flexibility in the parameter selections and yields better performance. The validity is demonstrated by computer simulation and real application in Secs. 4.5 and 5.3, respectively.

Finally, by applying the 2D-CWT to the analysis of multiple phase-shifted interferograms, the hybrid 2D-CWT technique overcomes the limitations of the PS and 2D-CWT technique while possessing the advantages of both techniques, i.e. automatic analysis and robustness to noise and defects. This hybrid technique is capable of accurately and automatically analyzing interferograms containing complex fringes as well as noise and defects.

A computer simulation has been carried out to verify the effectiveness of the technique by applying the 2D-CWT in phase-shifting interferograms in Sec. 4.6.

6.2 Future Work

Although many achievements have been made for the 2D-CWT technique in fringe pattern analysis, there are still a few problems have to be solved. Firstly, the systematic analysis of the accuracy of the 2D-CWT technique is still lacking. Most of the analysis of the 2D-CWT is based on the simulations and experiments, and compared with a reference phase map, for example, obtained by using the PS technique. Although the quantitative data analysis can be processed, the model of the error is not available yet. It causes the analysis of real experiments is inconvincible. Hence, an effort to build up the mathematic model for the accuracy analysis of the 2D-CWT is highly demanded. Secondly, the 2D-CWT technique does not work well when deals with the relative low-frequency component. This is determined by the inherent features of the WT which is designed for analyzing the details of signals. How to analyze fringe patterns which have rich frequency components will be a challenge task. Finally, an inevitable question is whether the DWT can be used in fringe pattern analysis or not. Because of the mature implementation algorithm and fast processing speed, the DWT is very attractive compared with the continuous one in fringe pattern analysis.

Bibliography

- [1] D. W. Robinson and G. T. Reid, eds., *Interferogram Analysis, Digital Fringe Pattern Measurement Techniques*. Bristol and Philadelphia: Institute of Physics Publishing, 1993.
- [2] D. Malacara, *Optical Shop Testing*. Hoboken: John Wiley & Sons, 3rd ed., 2007.
- [3] M. Tang, Q. Wang, J. Zhu, and H. Xie, “Phase-shifting laser scanning confocal microscopy moiré method and its applications,” *Measurement Science and Technology*, vol. 21, no. 5, pp. 55110–55119, 2011.
- [4] T. Hoang, Z. Wang, M. Vo, J. Ma, L. Luu, and B. Pan, “Phase extraction from optical interferograms in presence of intensity nonlinearity and arbitrary phase shifts,” *Applied Physics Letters*, vol. 99, p. 031104, 2011.
- [5] R. Séfel and J. Kornis, “Double-exposure phase calculation method in electronic speckle pattern interferometry based on holographic object illumination,” *Applied Optics*, vol. 50, no. 23, pp. 4642–4647, 2011.
- [6] L. Kai and Q. Kemao, “Dynamic phase retrieval in temporal speckle pattern interferometry using least squares method and windowed fourier filtering,” *Optics Express*, vol. 19, no. 19, pp. 18058–18066, 2011.

- [7] M. Vo, Z. Wang, T. Hoang, and D. Nguyen, “Flexible calibration technique for fringe-projection-based three-dimensional imaging,” *Optics Letters*, vol. 35, no. 19, pp. 3192–3194, 2010.
- [8] Z. Song, “Recent progresses on real-time 3D shape measurement using digital fringe projection techniques,” *Optics and Lasers in Engineering*, vol. 48, no. 2, pp. 149–158, 2010.
- [9] G. A. Ayubi, J. M. Di Martino, J. R. Alonso, A. Fernández, C. D. Perciante, and J. A. Ferrari, “Three-dimensional profiling with binary fringes using phase-shifting interferometry algorithms,” *Applied Optics*, vol. 50, no. 2, pp. 147–154, 2011.
- [10] M. Takeda, H. Ina, and S. Kobayashi, “Fourier-transform method of fringe-pattern analysis for computer-based topography and interferometry,” *Journal of the Optical Society of America*, vol. 72, no. 1, pp. 156–160, 1982.
- [11] Q. Kema, “Windowed fourier transform for fringe pattern analysis,” *Applied Optics*, vol. 43, no. 13, pp. 2695–2702, 2004.
- [12] Q. Kema, “Windowed fourier transform for fringe pattern analysis: Addendum,” *Applied Optics*, vol. 43, no. 17, pp. 3472–3473, 2004.
- [13] Q. Kema, “Two-dimensional windowed fourier transform for fringe pattern analysis: Principles, applications and implementations,” *Optics and Lasers in Engineering*, vol. 45, no. 2, pp. 304–317, 2007.
- [14] Q. Kema, H. Wang, and W. Gao, “Windowed fourier transform for fringe pattern analysis: Theoretical analyses,” *Applied Optics*, vol. 47, no. 29, pp. 5408–5419, 2008.

- [15] Q. Kemao, H. Wang, and W. Gao, “Some recent developments of windowed fourier transform for fringe pattern analysis,” in *AIP Conference Proceedings*, vol. 1236, (Monte Verita), pp. 106–111, 2010.
- [16] P. Tomassini, A. Giulietti, L. A. Gizzi, M. Galimberti, D. Giulietti, M. Borghesi, and O. Willi, “Analyzing laser plasma interferograms with a continuous wavelet transform ridge extraction technique:tthe method,” *Applied Optics*, vol. 40, no. 35, pp. 6561–6568, 2001.
- [17] K. Kadooka, K. Kunoo, N. Uda, K. Ono, and T. Nagayasu, “Strain analysis for moiré interferometry using the two-dimensional continuous wavelet transform,” *Experimental Mechanics*, vol. 43, no. 1, pp. 45–51, 2003.
- [18] C. A. Sciammarella, “Fringe pattern information retrieval using wavelets,” in *Proceedings of SPIE*, vol. 5914, (San Diego), p. 59140A, 2005.
- [19] C. A. Sciammarella and T. Kim, “Frequency modulation interpretation of fringes and computation of strains,” *Experimental Mechanics*, vol. 45, no. 5, pp. 393–403, 2005.
- [20] L. R. Watkins, S. M. Tan, and T. H. Barnes, “Determination of interferometer phase distributions by use of wavelets,” *Optics Letters*, vol. 24, no. 13, pp. 905–907, 1999.
- [21] R. Carmona, W. Hwang, and B. Torresani, “Characterization of signals by the ridges of their wavelet transforms,” *Signal Processing, IEEE Transactions on*, vol. 45, no. 10, pp. 2586–2590, 1997.
- [22] A. Federico and G. H. Kaufmann, “Evaluation of the continuous wavelet transform method for the phase measurement of electronic speckle pattern interferometry fringes,” *Optical Engineering*, vol. 41, no. 12, pp. 3209–3216, 2002.

- [23] H. Liu, A. N. Cartwright, and C. Basaran, “Moiré interferogram phase extraction: A ridge detection algorithm for continuous wavelet transforms,” *Applied Optics*, vol. 43, no. 4, pp. 850–857, 2004.
- [24] J. Bethge, C. Grebing, and G. Steinmeyer, “A fast gabor wavelet transform for high-precision phase retrieval in spectralinterferometry,” *Optics Express*, vol. 15, no. 22, pp. 14313–14321, 2007.
- [25] S. Li, X. Su, and W. Chen, “A new wavelet transform for reliability-guided phase unwrapping of optical fringe patterns,” *Optics Communications*, vol. 284, no. 20, pp. 4879–4883, 2011.
- [26] Z. Wang, J. Ma, and M. Vo, “Recent progress in two-dimensional continuous wavelet transform technique for fringe pattern analysis,” *Optics and Lasers in Engineering*, vol. 50, no. 8, pp. 1052–1058, 2012.
- [27] H. Niu, C. Quan, and C. Tay, “Phase retrieval of speckle fringe pattern with carriers using 2D wavelet transform,” *Optics and Lasers in Engineering*, vol. 47, no. 12, pp. 1334–1339, 2009.
- [28] J. Weng, J. Zhong, and C. Hu, “Phase reconstruction of digital holography with the peak of the two-dimensional gabor wavelet transform,” *Applied Optics*, vol. 48, no. 18, pp. 3308–3316, 2009.
- [29] H. Wang and Q. Kemo, “Frequency guided methods for demodulation of a single fringe pattern,” *Optics Express*, vol. 17, no. 17, pp. 15118–15127, 2009.
- [30] M. Servin, J. L. Marroquin, and F. J. Cuevas, “Demodulation of a single interferogram

by use of a two-dimensional regularized phase-tracking technique,” *Applied Optics*, vol. 36, no. 19, pp. 4540–4548, 1997.

- [31] M. Servin, J. L. Marroquin, and F. J. Cuevas, “Fringe-follower regularized phase tracker for demodulation of closed-fringe interferograms,” *Journal of the Optical Society of America A*, vol. 18, no. 3, pp. 689–695, 2001.
- [32] M. Servin, J. L. Marroquin, and J. A. Quiroga, “Regularized quadrature and phase tracking from a single closed-fringe interferogram,” *Journal of the Optical Society of America A*, vol. 21, no. 3, pp. 411–419, 2004.
- [33] L. Kai and Q. Kemao, “Fast frequency-guided sequential demodulation of a single fringe pattern,” *Optics Letters*, vol. 35, no. 22, pp. 3718–3720, 2010.
- [34] K. Li and B. Pan, “Frequency-guided windowed fourier ridges technique for automatic demodulation of a single closed fringe pattern,” *Applied Optics*, vol. 49, no. 1, pp. 56–60, 2010.
- [35] Z. Wang and H. Ma, “Advanced continuous wavelet transform algorithm for digital interferogram analysis and processing,” *Optical Engineering*, vol. 45, p. 045601, 2006.
- [36] M. Gdeisat, D. Burton, F. Lilley, M. Lalor, and C. Moore, “Spatial carrier fringe pattern demodulation by use of a two-dimensional continuous paul wavelet transform,” in *AIP Conference Proceedings*, vol. 1236, (Monte Verita), pp. 112–117, 2010.
- [37] S. Li, X. Su, and W. Chen, “Wavelet ridge techniques in optical fringe pattern analysis,” *Journal of the Optical Society of America A*, vol. 27, no. 6, pp. 1245–1254, 2010.

- [38] M. A. Gdeisat, D. R. Burton, and M. J. Lalor, “Spatial carrier fringe pattern demodulation by use of a two-dimensional continuous wavelet transform,” *Applied Optics*, vol. 45, no. 34, pp. 8722–8732, 2006.
- [39] J. Ma, Z. Wang, B. Pan, T. Hoang, M. Vo, and L. Luu, “Two-dimensional continuous wavelet transform for phase determination of complex interferograms,” *Applied Optics*, vol. 50, no. 16, pp. 2425–2430, 2011.
- [40] A. Z. Abid, M. A. Gdeisat, D. R. Burton, M. J. Lalor, and F. Lilley, “Spatial fringe pattern analysis using the two-dimensional continuous wavelet transform employing a cost function,” *Applied Optics*, vol. 46, no. 24, pp. 6120–6126, 2007.
- [41] S. Li, X. Su, and W. Chen, “Spatial carrier fringe pattern phase demodulation by use of a two-dimensional real wavelet,” *Applied Optics*, vol. 48, no. 36, pp. 6893–6906, 2009.
- [42] S. Fernandez, M. A. Gdeisat, J. Salvi, and D. Burton, “Automatic window size selection in windowed fourier transform for 3D reconstruction using adapted mother wavelets,” *Optics Communications*, vol. 284, no. 12, pp. 2797–2807, 2011.
- [43] J. Ma, Z. Wang, M. Vo, and L. Luu, “Parameter discretization in two-dimensional continuous wavelet transform for fast fringe pattern analysis,” *Applied Optics*, vol. 50, no. 34, pp. 6399–6408, 2011.
- [44] H. Li and C. Yang, “Two-dimensional multiscale windowed fourier transform based on two-dimensional wavelet transform for fringe pattern demodulation,” *Optics & Laser Technology*, vol. 43, no. 1, pp. 72–81, 2011.

- [45] L. Huang, Q. Kemao, B. Pan, and A. K. Asundi, “Comparison of fourier transform, windowed fourier transform, and wavelet transform methods for phase extraction from a single fringe pattern in fringe projection profilometry,” *Optics and Lasers in Engineering*, vol. 48, no. 2, pp. 141–148, 2010.
- [46] K. Creath, “Phase-shifting speckle interferometry,” *Applied Optics*, vol. 24, no. 18, pp. 3053–3058, 1985.
- [47] B. Ströbel, “Processing of interferometric phase maps as complex-valued phasor images,” *Applied Optics*, vol. 35, no. 13, pp. 2192–2198, 1996.
- [48] D. Malacara, M. Servín, and Z. Malacara, *Interferogram analysis for optical testing*. Boca Raton: CRC Press, 2nd ed., 2005.
- [49] M. Servin, J. C. Estrada, and J. A. Quiroga, “The general theory of phase shifting algorithms,” *Optics Express*, vol. 17, no. 24, pp. 21867–21881, 2009.
- [50] K. J. Gåsvik, *Optical Metrology*. Chichester: John Wiley & Sons, 3rd ed., 2002.
- [51] C. A. Sciammarella, “Overview of optical techniques that measure displacements: Murray lecture,” *Experimental Mechanics*, vol. 43, no. 1, pp. 1–19, 2003.
- [52] Merriam-Webster, *Merriam-Webster’s Collegiate Dictionary*. Springfield: Merriam-Webster, 11th ed., 2003.
- [53] B. E. Ross, C. A. Sciammarella, and D. Sturgeon, “Basic optical law in the interpretation of moiré patterns applied to the analysis of strains – Part 2,” *Experimental Mechanics*, vol. 5, no. 6, pp. 161–166, 1965.

- [54] C. A. Sciammarella, “Basic optical law in the interpretation of moiré patterns applied to the analysis of strains – Part 1,” *Experimental Mechanics*, vol. 5, no. 5, pp. 154–160, 1965.
- [55] C. A. Sciammarella, “The moiré method – A review,” *Experimental Mechanics*, vol. 22, no. 11, pp. 418–433, 1982.
- [56] C. A. Walker, “A historical review of moiré interferometry,” *Experimental Mechanics*, vol. 34, no. 4, pp. 281–299, 1994.
- [57] D. Post, B. Han, and P. Ifju, *High Sensitivity Moire: Experimental Analysis for Mechanics and Materials*. New York: Springer-Verlag New York, 1997.
- [58] C. A. Sciammarella and T. Kim, “Determination of strains from fringe patterns using space-frequency representations,” *Optical Engineering*, vol. 42, no. 11, pp. 3182–3193, 2003.
- [59] C. J. Tay, C. Quan, Y. Fu, and Y. Huang, “Instantaneous velocity displacement and contour measurement by use of shadow moiré and temporal wavelet analysis,” *Applied Optics*, vol. 43, no. 21, pp. 4164–4171, 2004.
- [60] M. A. M. Cavaco, *Automated Fringe Analysis in Moire Interferometry*. PhD thesis, Lehigh University, Pennsylvania, 1995.
- [61] J. M. Huntley, “Automated fringe pattern analysis in experimental mechanics: A review,” *The Journal of Strain Analysis for Engineering Design*, vol. 33, no. 2, pp. 105–125, 1998.
- [62] Z. Wang, *Development and Application of Computer-Aided Fringe Analysis*. PhD thesis, University of Maryland, College Park, Maryland, 2003.

- [63] W. Osten, ed., *Fringe 2005: The 5th International Workshop on Automatic Processing of Fringe Patterns*. Berlin Heidelberg: Springer-Verlag Berlin Heidelberg, 2006.
- [64] W. Osten and M. Kujawinska, eds., *Fringe 2009: The 6th International Workshop on Advanced Optical Metrology*. Berlin Heidelberg: Springer-Verlag Berlin Heidelberg, 2009.
- [65] K. Itoh, “Analysis of the phase unwrapping algorithm,” *Applied Optics*, vol. 21, no. 14, pp. 2470–2470, 1982.
- [66] D. C. Ghiglia, G. A. Mastin, and L. A. Romero, “Cellular-automata method for phase unwrapping,” *Journal of the Optical Society of America A*, vol. 4, no. 1, pp. 267–280, 1987.
- [67] J. M. Huntley, “Noise-immune phase unwrapping algorithm,” *Applied Optics*, vol. 28, no. 16, pp. 3268–3270, 1989.
- [68] J. M. Huntley and H. Saldner, “Temporal phase-unwrapping algorithm for automated interferogram analysis,” *Applied Optics*, vol. 32, no. 17, pp. 3047–3052, 1993.
- [69] D. C. Ghiglia and L. A. Romero, “Robust two-dimensional weighted and unweighted phase unwrapping that uses fast transforms and iterative methods,” *Journal of the Optical Society of America A*, vol. 11, no. 1, pp. 107–117, 1994.
- [70] T. R. Judge and P. J. Bryanston-Cross, “A review of phase unwrapping techniques in fringe analysis,” *Optics and Lasers in Engineering*, vol. 21, no. 4, pp. 199–239, 1994.
- [71] D. C. Ghiglia and M. D. Pritt, *Two-Dimensional Phase Unwrapping: Theory, Algorithms, and Software*. New York: Wiley, 1998.

- [72] J. Strand and T. Taxt, “Performance evaluation of two-dimensional phase unwrapping algorithms,” *Applied Optics*, vol. 38, no. 20, pp. 4333–4344, 1999.
- [73] M. A. Herráez, D. R. Burton, M. J. Lalor, and M. A. Gdeisat, “Fast two-dimensional phase-unwrapping algorithm based on sorting by reliability following a noncontinuous path,” *Applied Optics*, vol. 41, no. 35, pp. 7437–7444, 2002.
- [74] X. Su and W. Chen, “Reliability-guided phase unwrapping algorithm: a review,” *Optics and Lasers in Engineering*, vol. 42, no. 3, pp. 245–261, 2004.
- [75] A. Federico and G. H. Kaufmann, “Phase retrieval in digital speckle pattern interferometry by use of a smoothed space-frequency distribution,” *Applied Optics*, vol. 42, no. 35, pp. 7066–7071, 2003.
- [76] G. Rajsekhar, S. S. Gorthi, and P. Rastogi, “Adaptive window Wigner-Ville-distribution-based method to estimate phase derivative from optical fringes,” *Optics Letters*, vol. 34, no. 20, pp. 3151–3153, 2009.
- [77] J. Zhong and H. Zeng, “Multiscale windowed fourier transform for phase extraction of fringe patterns,” *Applied Optics*, vol. 46, no. 14, pp. 2670–2675, 2007.
- [78] F. Hlawatsch and F. Auger, eds., *Time-Frequency Analysis*. London and Hoboken: ISTE and John Wiley & Sons, 2008.
- [79] L. Cohen, *Time Frequency Analysis: Theory and Applications*. Upper Saddle River: Prentice Hall, 1994.
- [80] K. Gröchenig, *Foundations of Time-Frequency Analysis*. Cambridge: Birkhäuser Boston, Dec. 2000.

- [81] Y. Meyer, *Wavelets: Algorithms & Applications*. Philadelphia: Society for Industrial and Applied Mathematics, 1993.
- [82] B. B. Hubbard, *The World According to Wavelets: The Story of a Mathematical Technique in the Making*. Natick: A K Peters/CRC Press, 2nd ed., 1998.
- [83] C. K. Chui, *An Introduction to Wavelets, Volume 1*. San Diego: Academic Press, 1992.
- [84] I. Daubechies, *Ten Lectures on Wavelets*. Philadelphia: Society for Industrial and Applied Mathematics, 1992.
- [85] C. S. Burrus, R. A. Gopinath, and H. Guo, *Introduction to Wavelets and Wavelet Transforms: A Primer*. Upper Saddle River: Prentice-Hall, 1997.
- [86] S. Mallat, *A Wavelet Tour of Signal Processing, Third Edition: The Sparse Way*. Burlington: Academic Press, 2008.
- [87] M. B. Ruskai, *Wavelets and Their Applications*. Jones and Bartlett books in mathematics, Boston: Jones and Barlett, 1992.
- [88] J. Byrnes, K. A. Hargreaves, and K. Berry, eds., *Wavelets and their Applications (NATO Science Series C:)*. Dordrecht: Kluwer Academic Publishers, 1994.
- [89] P. S. Addison, *The Illustrated Wavelet Transform Handbook: Introductory Theory and Applications in Science, Engineering, Medicine and Finance*. Bristol: Institute of Physics Publishing, 2002.
- [90] J. S. Walker, *A Primer on Wavelets and Their Scientific Applications*. Boca Raton: Chapman & Hall/CRC, 2nd ed., 2008.

- [91] H. Stark, *Wavelets and Signal Processing: An Application-Based Introduction*. Berlin Heidelberg: Springer-Verlag Berlin Heidelberg, 2010.
- [92] P. Kumar and E. Foufoula-Georgiou, *Wavelets in Geophysics*, vol. 4 of *Wavelet analysis and its applications*. San Diego: Academic Press, 1994.
- [93] A. Aldroubi and M. A. Unser, *Wavelets in Medicine and Biology*. Boca Raton: CRC Press, 1996.
- [94] J. C. v. d. Berg, *Wavelets in Physics*. Cambridge: Cambridge University Press, 1999.
- [95] J. Antoine, R. Murenzi, P. Vandergheynst, and S. T. Ali, *Two-Dimensional Wavelets and their Relatives*. Cambridge: Cambridge University Press, 2004.
- [96] N. Delprat, B. Escudie, P. Guillemain, R. Kronland-Martinet, P. Tchamitchian, and B. Torresani, “Asymptotic wavelet and gabor analysis: extraction of instantaneous frequencies,” *Information Theory, IEEE Transactions on*, vol. 38, no. 2, pp. 644–664, 1992.
- [97] H. Liu, *Phase Reconstruction of Phase Shifted Moire Interferograms Using Continuous Wavelet Transforms*. PhD thesis, State University of New York at Buffalo, New York, 2003.
- [98] J. Antoine, P. Carrette, R. Murenzi, and B. Piette, “Image analysis with two-dimensional continuous wavelet transform,” *Signal Processing*, vol. 31, no. 3, pp. 241–272, 1993.
- [99] C. Gonnet and B. Torresani, “Local frequency analysis with two-dimensional wavelet transform,” *Signal Processing*, vol. 37, no. 3, pp. 389–404, 1994.

- [100] T. Kim, *Determination of frequencies from fringe patterns using short-term Fourier transforms and wavelet transforms*. PhD thesis, Illinois Institute of Technology, Illinois, 2003.
- [101] K. Patorski and K. Pokorski, “Examination of singular scalar light fields using wavelet processing of fork fringes,” *Applied Optics*, vol. 50, no. 5, pp. 773–781, 2011.
- [102] A. A. Abdulbasit Zaid, *Fringe Pattern Analysis using Wavelet Transforms*. PhD thesis, Liverpool John Moores University, Liverpool, 2008.
- [103] R. Dingle, *Asymptotic Expansions: Their Derivation and Interpretation*. New York: Academic Press, 1973.
- [104] C. M. Bender and S. A. Orszag, *Advanced Mathematical Methods for Scientists and Engineers: Asymptotic Methods and Perturbation Theory*. New York: Springer-Verlag New York, 1999.
- [105] C. A. Sciammarella and F. M. Sciammarella, “Heisenberg principle applied to the analysis of speckle interferometry fringes,” *Optics and Lasers in Engineering*, vol. 40, no. 5-6, pp. 573–588, 2003.
- [106] J. Ma, Z. Wang, M. Vo, and B. Pan, “Wavelet selection in two-dimensional continuous wavelet transform technique for optical fringe pattern analysis,” *Journal of Optics*, vol. 14, no. 6, p. 065403, 2012.
- [107] M. Afifi, A. Fassi-Fihri, M. Marjane, K. Nassim, M. Sidki, and S. Rachafi, “Paul wavelet-based algorithm for optical phase distribution evaluation,” *Optics Communications*, vol. 211, no. 1-6, pp. 47–51, 2002.

- [108] R. Murenzi, “Scale-angle CWT features: application in object recognition,” in *Proceedings of SPIE*, (Denver), pp. 16–27, 1999.
- [109] K. Pokorski and K. Patorski, “Visualization of additive-type moiré and time-average fringe patterns using the continuous wavelet transform,” *Applied Optics*, vol. 49, no. 19, pp. 3640–3651, 2010.
- [110] J. Ma, Z. Wang, and M. Vo, “Hybrid two-dimensional continuous wavelet transform for analysis of phase-shifted interferograms,” *Optics Communications*, no. 0, pp. 3917–3920, 2012.